Enhanced Raman spectrometry for environmental gas sensing and human breath analysis

seit 1558

DISSERTATION

zur Erlangung des akademischen Grades doctor rerum naturalium (Dr. rer. nat.)

vorgelegt dem Rat der Chemisch-Geowissenschaftlichen Fakultät

der Friedrich-Schiller-Universität Jena

eingereicht von Dipl.-Phys. Stefan Hanf

geboren am 30. Mai 1985 in Gera

1. Gutachter: Prof. Dr. rer. nat. Jürgen Popp

2. Gutachter: Prof. Dr. rer. nat. Markus Schmidt

eingereicht am: 06.05.2015

Tag der Verteidigung: 04.09.2015

Index of abbreviations

AD(C)	analog-to-digital(-converter)
AR	anti-reflection
ATIR	attenuated total internal reflection
C	carbon
CCD	charged-couple device
CERS	cavity-enhanced (multi-gas) Raman spectrometry
CMOS	complementary metal-oxide-semiconductor
CRDS	cavity-ring down spectroscopy
cw	continuous-wave
DCRR	differential cosmic ray removal
DOS	density of states
DPSSL	diode-pumped solid-state laser)
EtOH	ethanol (C_2H_6O)
FAST	fiber array spectral translation
FAST-RI	fiber spectral translator-based Raman imaging
FERS	fiber-enhanced Raman spectroscopy
FWHM	full width of half maximum
GC	gas chromatography
HBT	hydrogen breath test
HC	hollow core
HC-PCF	hollow-core photonic crystal fiber
HPLC	high-pressure liquid chromatography
HPLC-PAD	high-pressure liquid chromatography pulsed amperometric detection
HR	hyperspectral
IR	infrared
ISO	International Organization for Standardization
LFL	lower flammability limit
LO	longitudinal optical

LOD	limit of detection
LN$_2$	liquid nitrogen (N$_2$)
LWD	long working distance
MFC	mass flow controller
MFD	mode field diameter
MOF	microstructured optical fiber
MS	mass spectrometry
NA	numerical aperture
Nd:YAG	neodymium-doped yttrium aluminum garnet (Nd:Y$_3$Al$_5$O$_{12}$)
NIR	near-infrared
NSC	non-structural carbohydrates
PBC	power build-up cavity
PBG	photonic bandgap
PC	photonic crystal
PCF	photonic crystal fiber
ppb	parts per billion
ppm	parts per million
ppt	parts per trillion
REM	raster electron microscope
rms	root mean square
RQ	respiratory quotient
RR	respiration rate
SNR	signal-to-noise ratio
TIR	total internal reflection
UHPLC	ultra-high performance/pressure liquid chromatography
VIS	visible
VOC	volatile organic compound
WSC	water-soluble carbohydrates

Table of Contents

1 Introduction

Gas sensing techniques allow for groundbreaking studies in the field of plant-physiological processes, soil-bacteria interactions, as well as early stage monitoring of disease states via human breath analysis [5, 174, 170, 28]. Easy-to-operate, miniaturized, on-site, and cost-efficient gas sensors have attracted great interest in the scientific community in the last years [50, 113]. In addition, environmental gas sensing includes the quantitative detection and simultaneous monitoring of climate-relevant atmospheric trace gases such as CH_4, CO_2, and N_2O besides N_2 and O_2 in a wide range of concentration. Apart from monitoring in a biogeochemical context, these gases face crucial importance as tracers for clinical diagnostics of metabolic disorders or diseases related to human breath analysis. The latter is non-invasive, acceptable for patients, and allows a repeatable sampling in a short amount of time. The human breath is a mixture of different compounds such as N_2, O_2, CO_2, and H_2O in high concentrations, minor gas components, and small fractions of volatile organic compounds (VOC). Concentrations of these VOC vary from parts per million (ppm) even to parts per trillion (ppt). Important gases in the low ppm region are for example CH_4, H_2, CO, CO_2, NH_3, and C_3H_6O for the detection of diseases or disorders such as lung cancer (C_3H_6O, CH_4), (mitochondrial) oxidative stress (CO), colonic fermentation (CH_4, H_2), or *Helicobacter pylori* infection (NH_3, $^{12}CO_2/^{13}CO_2$). One major challenge is the accurate real-time quantification of many gases ranging in different concentrations simultaneously.

The most commonly used technique to quantify a mixture of exhaled VOC is mass spectrometry (MS) often in combination with gas chromatography (GC). Although MS is accurate, highly sensitive, and monitors gases simultaneously within seconds, this technique would be sample-destructive, expensive, bulky due to the requirement of high vacuum turbo pumps, and is therefore not suitable for clinical applications. In addition, GC requires a complicated sampling preparation, is difficult to calibrate, and is limited for miniaturization. Optical absorption spectroscopic methods such as mid- and near-infrared absorption spectroscopy [193], (broadband) cavity-ring down spectroscopy (CRDS) [185], or photoacoustic spectroscopy [76] are applicable for the sensitive detection of different VOC with strong dipole moment such as H_2O, CO_2, CH_4, and N_2O. Here, the highly sensitive multi-gas detection in a single cavity at the ppb-level is restricted to limited availability of NIR broadband sources. Another drawback is the lower reflectivity of broadband mirrors with values $< 99.9\%$ in this spectral region connected to a necessary feedback system for the correction of opto-mechanical and opto-thermal drifts [150]. Furthermore, these absorption spectroscopic methods cannot be applied for homonuclear diatomic molecules such as H_2, N_2, or O_2 due to the missing permanent dipole moment [77].

In contrast, Raman spectroscopy is based on molecular vibrations and therefore a potential candidate for specific multi-compound gas analysis in clinical diagnosis and biogenic multi-gas monitoring. One main advantage for the application of Raman spectroscopy is the ability to detect the homonuclear diatomic gases, as well as other molecular gas species including stable isotope gases such $^{13}CO_2$, $^{14}N^{15}N$, or $^{15}N_2$. Raman gas analysis is fast, non-consumptive, requires no labeling or sampling, and enables a simultaneous detection of all gases except noble gases.

However, a major drawback is the intrinsically weak Raman effect, which has low absolute scattering cross sections and needs to be enhanced to achieve reasonable limits of detection for the mentioned applications. Different methods such as initializing high

power lasers [178] or applying higher analyte pressures up to 150 bar [83] to increase the number of scattering particles, utilizing highly reflective mirrors for multi-beam pass arrangements [99, 134, 140, 162], or applying optical power built-up cavities [110, 131] are implemented to provide enhancement factors for sufficient sensitivity levels. Gas sensing with optical waveguides, which enable optimal light-analyte interaction over long optical distances, has become of growing importance and sensors based on capillaries [132, 133, 137, 20] or hollow metal waveguides [23] are well-known in literature. Nevertheless, they suffer from high attenuation of signal and laser light within the waveguide. The resulting sensitivities in the range of several tens to hundreds ppm are not sufficient for clinical diagnostics and biogene multi-component gas monitoring.

However, hollow-core photonic crystal fibers (HC-PCF) have arisen as auspicious technology in the field of trace gas sensing, showing the potential to further increase the sensitivity [32, 21, 22]. This novel type of fiber with characteristically low waveguide losses enables the long optical interaction of laser light with Raman-active gas molecules. State-of-the-art fiber-based Raman spectroscopic setups were introduced as a promising new methodology for non-invasive and painless multi-component breath sensors in the field of clinical diagnosis with detection limits < 100 ppm [35]. However, the Raman-based detection of even lower concentrated VOC such as CH_4, H_2, $^{13}CO_2$, or C_3H_6O at concentration levels of several ppm or even sub-ppm is not yet established in medical breath analysis. Hence, innovative multi-gas sensors for H_2 and CH_4 as combined biomarkers for colonic fermentation of undigested or unabsorbed oligosaccharides from exhaled human breath of concentrations in the range $1 - 100$ ppm are for example required for the implementation of hydrogen breath tests.

The main objective of this thesis is to develop a fiber-enhanced Raman multi-gas sensor for manifold applications in the field of clinical diagnosis and environmental science in a wide concentration range. Compactness in combination with high accuracy, sensitivity, and precision is desired for this purpose. This will be achieved by merging the versatile Raman spectroscopic technique with applied state-of-the-art low loss microstructured optical fibers (e.g. HC-PCF) for the Raman signal enhancement. Even though the fiber approach is highly sensitive for several applications in clinical diagnostics, high finesse optical cavities meet the required level of miniaturization and compactness easily for the elucidation of complex and severely interdependent environmental processes by adequate levels of signal enhancement. Thus, continuous monitoring of O_2 and CO_2 respiration rates were further performed by utilizing a field-portable cavity-enhanced Raman spectrometric (CERS) multi-gas sensor [100] for the investigation in metabolic substrate change for droughted and shaded trees in the field of plant physiology.

The thesis structure is as follows: Firstly, theory on quantitative ro-vibrational and rotational Raman spectroscopy is briefly introduced in Chapter 2. The linear optical properties of HC-PCF, the Raman signal collection, and the flow dynamics in HC-PCF are presented in Chapter 3. Chapter 4 is focused on the optical design and analytical performance of the developed fiber-based multi-gas Raman spectroscopic setup. First simultaneous quantification of a biogenic gas mixture and the detection of exhaled human breath by fiber-enhanced Raman spectrometry (FERS) are shown. Since FERS analysis revealed an insufficiently high intrinsic signal background, the spatial analyte signal distribution was further quantitatively and qualitatively elucidated with the help of an applied fiber-array spectral translator-based (FAST) Raman imaging device in Chapter 5. Thus, a state-of-the-art FERS setup is adapted and improved to serve as a multi-component Raman gas sensor for the highly sensitive monitoring of disease-relevant multi-compound breath samples for non-invasive and painless breath gas analysis. Hence, Chapter 6 presents the simultaneous monitoring of H_2 and CH_4 in a simulated multi-gas breath mixture. Chapter 7 is focused on the utilization of a highly miniaturized cavity-enhanced Raman spectrometric device for the real-time and

long-term monitoring of minor deviations for respiratory O_2 and CO_2 fluxes on a high ambient background. These concentrations changes act as an indicator for alterations in respiratory substrate utilization for different ecologically important tree species, such as spruce and pine, under drought and shading. Finally, the thesis summarizes both introduced enhanced Raman spectrometric techniques and their applications in Chapter 8.

2 Theory of quantitative Raman scattering

The process of light being scattered by molecules has the unique property of causing resultant photons to have the same wavelength but different trajectories. This elastic Rayleigh scattering has a probability of 10^{-5} relative to all incoming photons for the transmission through 1 m of ambient air [122]. The even more rarely encountered process, namely inelastic scattering, predicted by Adolf Smekal in 1923 [173] and experimentally discovered by C.V. Raman and K.S. Krishnan in 1928 [149], was later named after on of its discoverers "Raman effect". This process of inelastic scattering of a photon with a diatomic molecule is illustrated in Fig. 2.1.
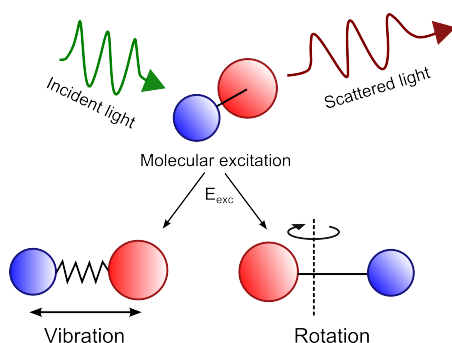
Figure 2.1: Illustrated Raman scattering process: An incident photon (green) with energy $h\nu_{\mathrm{in}}$ is scattered off of a diatomic molecule (dark red). The process of inelastic scattering results into vibrational and/or rotational excitation of a molecule with consequent energy transfer E_{exc}. The energy of the scattered photon is reduced to $h\nu' = h\nu_{\mathrm{in}} - E_{\mathrm{exc}}$, and thus its wavelength is increased (frequency is decreased).

Raman spectroscopy nowadays is used to reveal the qualitative and quantitative composition of samples, which can be solid, liquid, or gaseous. This chapter will provide the reader a sufficient theoretical background to follow the thesis' content mainly focusing on multi-component gas Raman spectrometry. Raman scattering for diatomic molecules covering pure rotational, vibrational, and ro-vibrational Raman transitions will be introduced. The issue of quantification is also discussed and concludes with a theoretical explanation of signal-to-noise ratio and limit of detection. The fundamentals of Raman effect are based on various books, e.g. by Long, McCreery, and Haken and Wolf [77, 122, 127], which cover this chapter.

2.1 Introduction to Raman scattering

The classical representation of the Raman effect originates from the definition of the Rayleigh scattering (Fig. 2.1). No vibration or rotation occurs for this form of radiation. If a light beam with frequency ν_0 and electric field intensity $E = E_0 \cdot \cos(2\pi\nu_0 t)$ scatters off of a molecule, a dipole moment p results within the molecule electron shell. It will vibrate with the same frequency similar to the E-vector of the incident light with $p = \alpha \cdot E_0 \cdot \cos(2\pi\nu_0 t)$, α being the molecule's polarizability. If the molecule already vibrates in one of its eigenstates, the induced moment with vibrational frequency ν_{vib} further modulates the amplitude for a change in molecular polarizability α and nuclei distance R. It follows a time-dependent approximation with $R = R_0 + d\alpha/dR \cdot (R - R_0) +$

higher order terms. A general schematic setup of Raman signal collection is presented in Fig. 2.2.
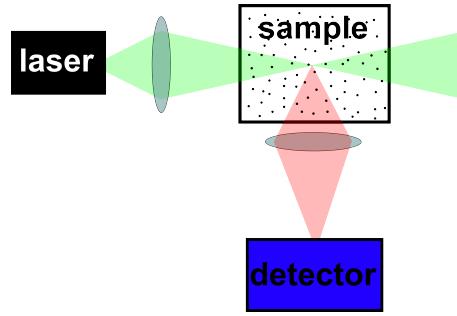
Figure 2.2: Scheme of a conventional Raman spectroscopic measurement with a 90 °-collection geometry: The intensity of the primary collected light, which most likely will be diffusely reflected into the detection system, is reduced compared to a 0 °-collection geometry.

The dipole moment, together with the change in polarizability, is represented with the help of $\cos \alpha \cdot \cos \beta = 1/2 \left[\cos(\alpha + \beta) + \cos(\alpha - \beta) \right]$:

$$p(t) = \alpha \cdot E \approx \left[\alpha(R_0) + \frac{d\alpha}{dR} q \cos\left(2\pi\nu_{\mathrm{vib}} t\right) \right] \cdot E_0 \left(2\pi\nu_0 t\right) = \alpha(R_0) E_0 \cos\left(2\pi\nu_0 t\right)$$

$$+ \frac{1}{2}\frac{d\alpha}{dR} E_0 \, q \left[\cos\left(2\pi(\nu_0 + \nu_{\mathrm{vib}})t\right) + \cos\left(2\pi(\nu_0 - \nu_{\mathrm{vib}})t\right) \right]. \qquad (2.1)$$

Emerging side bands with frequencies $\nu_0 \pm \nu_{\mathrm{vib}}$ are known as the first order vibrational Raman effect for the vibrational frequency ν_{vib}. With decreasing Raman intensity higher orders of $\nu_0 \pm 2\,\nu_{\mathrm{vib}}$, $\nu_0 \pm 3\,\nu_{\mathrm{vib}}$, ... are observed, i.e. the Raman effect of 2nd, 3rd, ... order. The spectroscopic vibration is Raman active, if $(d\alpha/dR) \neq 0$, which implies that the polarizability α of the molecule changes with the nuclei distance R caused by the vibrational Raman effect.
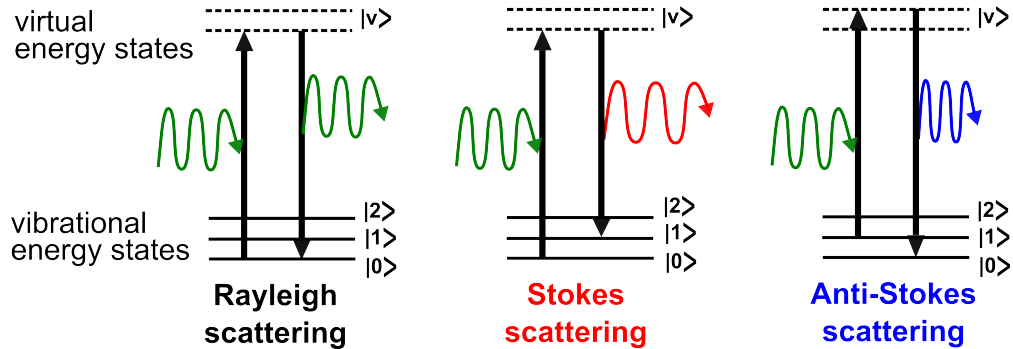
Figure 2.3: Energy level diagram for Raman scattering including real vibrational and virtual energy states for Rayleigh, Stokes, and Anti-Stokes scattering. The incident photon (green) with energy $h\nu_{\mathrm{in}}$ excites the molecule to a virtual quantum state ($|v>$) followed by a transition to a final state ($|i>$, $\mathrm{i} = 0, 1, 2$) in combination with the emission of a scattered photon (green, red, or blue). Rayleigh scattering: The initial and final states have no energy difference. Stokes scattering: The energy difference $E_{\mathrm{exc}} = h\nu' - h\nu_{\mathrm{in}}$ is < 0. The scattered photon is energetically red-shifted. Anti-Stokes scattering: The energy difference $E_{\mathrm{exc}} = h\nu' - h\nu_{\mathrm{in}}$ is > 0. The scattered photon is energetically blue-shifted.

This semi-classical approach is not valid, if Raman intensities are discussed [77]. For the energy shifted light, no difference in intensity would result between the incident light shifted to lower energies and the incident light shifted to higher energies, namely Stokes and Anti-Stokes lines. Only one photon out of $10^7 - 10^8$ is Raman scattered and intensity

contribution for inelastically scattered light is much smaller in elastically scattered light. This effect becomes comprehensible through a quantum theoretical approach [77].

The Raman effect as inelastic photon scattering compared to elastic photon scattering is illustrated in Fig. 2.3: The Stokes lines (Anti-Stokes lines) of one energy level with a smaller (higher) vibrational quantum number ν lead to a higher (lower) vibrational energy level for the inelastic scattering process, most probably from $\nu = 0 \rightarrow \nu = 1$ for Stokes scattering. Consequently, the wavenumber shift for Stokes Raman scattering can be described by $\nu' = \nu_0 - \nu_{\text{in}}$ and for Anti-Stokes scattering by $\nu' = \nu_0 + \nu_{\text{in}}$. The intensity distribution for several energy states between Stokes and Anti-Stokes transitions is governed by the probability of initial states. This can be calculated by the Boltzmann distribution for a thermal equilibrium:

$$\frac{I_{\text{Anti-Stokes}}}{I_{\text{Stokes}}} = \frac{n(\nu = 1)}{n(\nu = 0)} = \exp\left(\frac{-h\nu_{\text{vib}}}{k_B T}\right). \tag{2.2}$$

The Boltzmann constant k_B is $1.3806488 \cdot 10^{-23}$ J/K, Planck's constant is $6.62606957 \cdot 10^{-34}$ J·s, and thus Eq. 2.2 results in a value of 0.7 % for $T = 300\,\text{K}$ with $\nu_{\text{vib}} = 1000\,\text{cm}^{-1}$. Raman scattering processes involving higher energy transfers with $\Delta\nu = \pm 2, 3, \ldots$ have much smaller probabilities compared to the previously described case of $\Delta\nu = \pm 1$ for Stokes and Anti-Stokes Raman scattering.

Advances of Raman spectroscopy in comparison to other typically used techniques like absorption or emission spectroscopy are the application of single frequency laser and the detection of homonuclear molecules, which do not exhibit a permanent dipole moment, e.g. N_2, O_2, and H_2. The detection of the Raman process is usually non-destructive and non-consumptive for the analyte, non-contact, and usually no sample preparation is required.

This introduction covers only the semi-classical approach to describe the excited states for Raman scattering. A pure quantum mechanical model would further describe these processes and involved energies in much more detail [122], but this is of no relevance for the results presented here based on the given experimental precision and resolution.

2.2 Rotational and vibrational Raman spectroscopy

Vibrational states

For the description of vibrational energy states in a diatomic molecule, the generic model of a harmonic oscillator is applied. The approximation of an energy spectrum is as follows:

$$G(\nu) = \omega_e\left(\nu + \frac{1}{2}\right) \tag{2.3}$$

with ν being the vibrational quantum number in units cm^{-1}. The constant $\omega_e = (2\pi c)^{-1}\sqrt{k\mu^{-1}}$ contains the reduced mass μ of the molecule and the spring constant k characterizes the coupling between both atoms. For qualitative analysis of a vibrational Raman spectrum this model of a harmonic oscillator is usually exchanged by the Morse potential $V = D_e[1 - \exp(-a(R - R_e))]^2$ with dissociation energy D_e, equilibrium distance R_e, and $a = (m_r/2D_e)^{1/2}\omega_e$ in units cm^{-1} (Fig. 2.4).

The equidistant energy level spacing for the harmonic potential is not valid for the case of an anharmonic oscillator. The introduced correction is called the anharmonicity constant $\chi_e\omega_e$. Thus, Eq. 2.3 changes to

$$G(\nu) = \omega_e\left(\nu + \frac{1}{2}\right) - \chi_e\omega_e\left(\nu + \frac{1}{2}\right)^2. \tag{2.4}$$

The vibrational frequency decreases with increasing quantum number ν expressed by $\omega_\nu = \omega_e[1 - (\nu + 1/2)]$. Higher-order terms for adequate correction can be added in Eq. 2.4 [77], but are not relevant in this context.
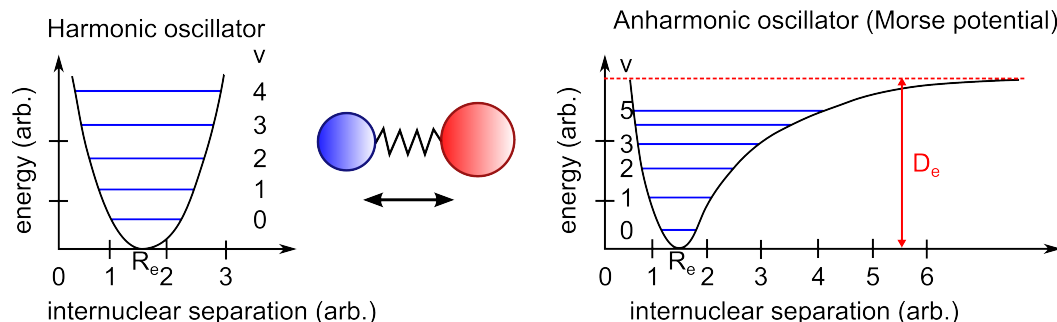
Figure 2.4: Comparison between (left) harmonic oscillator and (right) anharmonic oscillator by the model of the Morse potential with R_e being the equilibrium internuclear distance and ν the vibrational quantum number: The energy for the anharmonic oscillator converges to a dissociation energy D_e at an internuclear separation of $R_e \to \infty$. No bound states will appear above this energy.

Rotational states

The generic description of a diatomic molecule can be modeled by a rigid rotator for an energy configuration with quantized energy states for each rotational quantum number J. It follows the quantized energy spectrum $F(J)$ in units of cm^{-1} with

$$F(J) = B\,J\,(J+1) \tag{2.5}$$

and $B = h\,(8\pi^2 c)^{-1}\Theta^{-1}$ as the rotational constant for a molecule with mass-dependent moment of inertia Θ. Similar to Stokes and Anti-Stokes side bands for the Rayleigh line, side bands will arise for a pure rotational Raman process with $\Delta v = 0$. The quantum theoretical approach of the rational Raman effect resulting from an inelastic photon scattering process leads to the selection rule $\Delta J = \pm 2$ for rotational energy transitions. Thus, the eigen energy spectrum is represented by $\nu_{\text{rot}} = \pm B\,(4J+6)$ in cm^{-1} for $J = 0, 1, 2, \ldots$. For an energy transition with $\Delta J = +2$ the molecule is transferred to higher rotational states by a scattering process for Stokes Raman scattering. For the Anti-Stokes lines with $\Delta J = -2$ the inverted process is valid. The first Raman line with $\Delta J = 0$ differs by a distance of $6B$ from the Rayleigh line and every other line follows with an energy distance of $4B$. The intensity distribution for the rotational Raman spectrum is distributed by the thermal population with multiplicity of J-terms. It is expressed by

$$N_j = N\,\frac{hcB}{k_B T}\,(2J+1) \cdot \exp\left(-\frac{BJ(J+1)hc}{k_B T}\right), \tag{2.6}$$

for N_j being the number of populated electrons with N incident photons. The energy difference of neighboring rotational energy levels is much smaller than $k_B T$ and thus a small intensity difference for rotational Stokes and Anti-Stokes lines exists. Hence, the description of rotational Raman energy states by the rigid rotator is not a completely accurate description of a diatomic molecule since the molecular bonds are not rigid, i.e. have a variable inter atomic distance R.
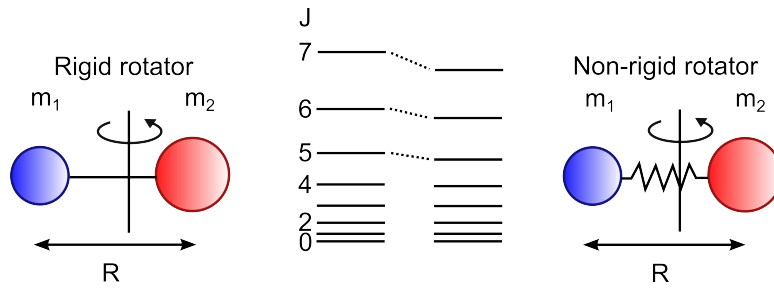
Figure 2.5: Illustrative comparison between rigid (left) and non-rigid (right) rotator of the energy spectrum for diatomic molecules: For the rigid rotator, the inter atomic distance R is fixed, whereas for the non-rigid rotator a flexible atomic connection with spring constant k is realized. For the latter, this consequently shifts the energy levels to lower values, respectively.

Usually the term in Eq. 2.5 is corrected by a stretching constant $D = h\left(32\pi^4 kc\Theta^2 R_e^2\right)^{-1}$ in units cm^{-1} and the modified energy $F(J)$ is then

$$F(J) = B\,J\,(J+1) - D\,J^2\,(J+1)^2. \tag{2.7}$$

D is This is illustratively shown in Fig. 2.5. Again, if a higher precision for describing the rotational Raman lines is required, further correction terms can be added [77].

2.3 Ro-vibrational Raman spectroscopy

In the previous section, the rotational and vibrational excitations are considered to be independent of each other. Raman spectroscopy usually reveals a combination of rotational and vibrational transitions leading to a so-called ro-vibrational Raman spectrum. Energy states for ro-vibrational transitions can be simultaneously described by additional terms contributing to these interactions. The increase of the internuclear separation R for higher vibrational quantum numbers ν is a consequence of the anharmonicity of the Morse potential (cf. Fig. 2.4). Consequently, rotational energy levels are shifted and the coupling is generally expressed by replacing the constants B and D in Eq. 2.4 and 2.7 by a ν-dependent term:

$$B \to B_\nu = B - \frac{\alpha}{2}\left(\nu + \frac{1}{2}\right), \tag{2.8}$$

$$D \to D_\nu = D - \beta\left(\nu + \frac{1}{2}\right). \tag{2.9}$$

α and β are the molecular specific correction constants. In summary, the complete terms for coupled ro-vibrational excitation levels T in units of cm^{-1} can be expressed by

$$
\begin{aligned}
T(\nu, J) \cong\ & \omega_e\left(\nu + \frac{1}{2}\right) - \chi_e\omega_e\left(\nu + \frac{1}{2}\right)^2 + B\,J\,(J+1) - D\,J^2\,(J+1)^2 \\
& - \alpha_e\left(\nu + \frac{1}{2}\right)J\,(J+1) - \beta_e\left(\nu + \frac{1}{2}\right)^2 J\,(J+1) \\
& - \gamma_e\left(\nu + \frac{1}{2}\right)J^2\,(J+1)^2.
\end{aligned}
\tag{2.10}
$$

This equation includes the previously described terms of the harmonic and anharmonic oscillator, rigid and non-rigid rotator, and coupling terms with constants α_e, β_e, and γ_e in units of cm^{-1}. Eq. 2.10 provides all energy terms relevant for this thesis in

sufficient precision. For even higher precision, higher order terms can be added. Further corrections are introduced for example by Haken and Wolf [77].

In the ro-vibrational Raman spectrum, $S-$, $Q-$, and $O-$branches will arise, which is illustrated in Fig. 2.6. In the case of Stokes scattering with $\Delta\nu_{\text{vib}} = +1$, these different branches are characterized by the energy and selection rules as follow:

S-branch, $\qquad \nu_0 - \Delta v_{\text{vib}} - \Delta\nu_{\text{rot}}, \qquad\qquad\qquad \Delta J = +2,$

Q-branch, $\qquad \nu_0 - \Delta v_{\text{vib}}, \qquad\qquad\qquad\qquad\quad \Delta J = 0,$

O-branch, $\qquad \nu_0 - \Delta v_{\text{vib}} + \Delta\nu_{\text{rot}}, \qquad\qquad\qquad \Delta J = -2.$

Here, $\Delta\nu_{\text{rot}}$ stands for the rotational energy difference $B(4J+6)$ in the case of a rigid rotator.
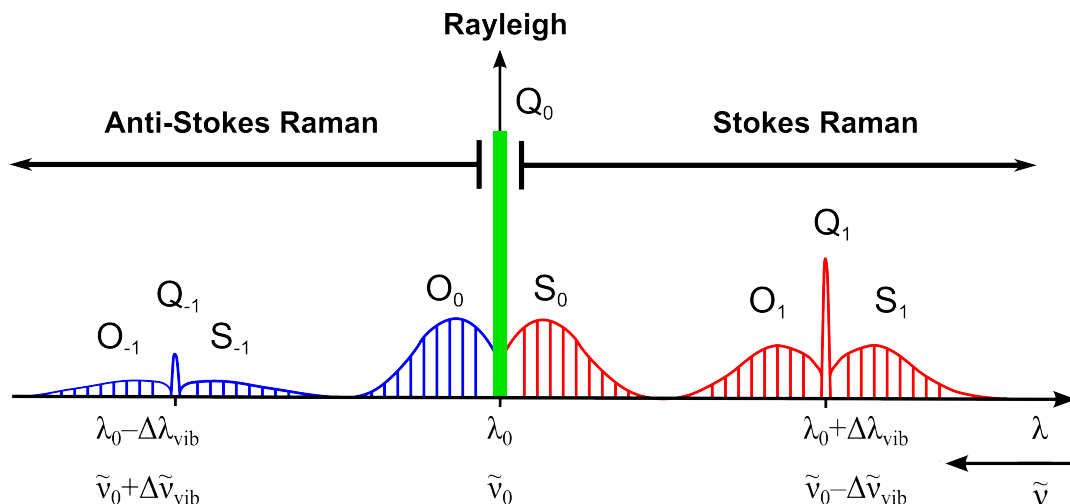
Figure 2.6: Illustration of a Raman spectrum for a diatomic molecule based on the described theory. The centric Rayleigh line Q_0 (green) at the frequency of the primary line is accompanied by pure rotational Raman lines, which are expressed by S-branch and O-branch. Vibrational Raman transitions show as well rotational side bands for Stokes and Anti-Stokes lines. The axis is labeled in wavelength, not in wavenumbers and the Anti-Stokes lines (blue) are usually much weaker than the Stokes lines (red) at room temperature accordingly to Boltzmann statistics.

Nuclear spin dependency

Typical intensity alterations are observable in homonuclear diatomic molecules such as N_2, O_2, and H_2, as well as in molecules with an inversion center, e.g. CO_2, for odd and even rotational states J. These alterations originate from the nuclear spin with resulting dependency on the statistics. For molecules with identical nuclei, the total wave function must be symmetric under any given interchange of the identical nuclei with integral spin. However, the wave function must be antisymmetric for identical nuclei with half-odd-integral for any spin exchange. Fermions are particles with a half-integer spin and bosons have an integer spin. Thus, the Pauli principle defines the total wave function to be (anti-)symmetric by transposition for (fermions) bosons. In general for a diatomic molecule with two identical nuclei with nuclear spin number I or for polyatomic molecules with an inversion center, the relationship for the statistical weight g_a and g_s of anti-symmetric and symmetric states is

$$\frac{g_a}{g_s} = \frac{I}{I+1}. \tag{2.11}$$

For example for a hydrogen nucleus with $I = 1/2$, Eq. 2.11 leads to an antisymmetric wave function for a hydrogen nucleus. Therefore, the rotational states with even J values combine with antisymmetric nuclear spin functions in order to have the degeneracy of

the statistical weight $(2I + 1) \cdot I = (2 \cdot 1/2 + 1) \cdot 1/2 = 1$. The statistical weight of this level can be defined by the number of quantum states corresponding to a given molecular energy level. Similarly, the rotational states with odd J values combine with symmetric nuclear spin functions resulting in a statistical weight $(2I + 1) \cdot I = (2 \cdot 1 + 1) \cdot 1 = 3$ for molecular hydrogen. Thus, an intensity increase for every second line in the ratio 3:1 is expected in the rotational spectrum of molecular hydrogen (cf. Fig. 5.4, Tab. 2.1). Molecules with nuclear spin $I = 1$, e.g. $^{14}N_2$, $^{15}N_2$, D_2, ..., will show an intensity alteration of 1:2 in the rotational spectrum (Tab. 2.1).

In the case of heteronuclear diatomic molecules such as X-Y, the interchange of a nuclei under a symmetric operation does not apply and the nuclear spin weight is $(2I_X + 1)(2I_Y + 1)$, where I_X and I_Y are the spins of nuclei X and Y respectively. The nuclear spin weight is the same for each rotational level and as a consequence, there is no intensity alteration in the rotational Raman lines, e.g. for molecule spectra such as $^{14}N^{15}N$, $^1H^2H$, ...

Molecular $^{16}O_2$ is unusual because it has a $^3\Sigma_g^-$-ground state and the electronic function is antisymmetric. Since the ^{16}O has a zero spin, i.e. $I = 0$, the total wave function must be symmetric. Therefore, the levels with odd (even) values of J are (anti-)symmetric for molecular oxygen. The rotational levels with even values of J combine with antisymmetric nuclear spin states leading to a statistical weight of 1. Consequently, only odd values of J are possible and rotational levels with even values of J are completely absent for $^{16}O_2$ and its isotopologue $^{18}O_2$. This is however not true for $^{16}O^{18}O$ and $^{16}O^{17}O$ due to the non-centrosymmetric molecule feature [77] (Tab. 2.1).

The rotational Raman spectrum of $^{16}O_2$ shows a general line separation of $8\,B$ for odd values and none for even values of J. The opposite behavior occurs for $^{12}C^{16}O_2$ molecules with a zero nuclear spin for ^{12}C. The CO_2-ground state $^1\Sigma_g^+$ is symmetric and the rotational levels with odd J values are completely absent due to a zero statistical weight. Only transitions between even J values are possible.

	$^1H_2$	$^{14}N_2$	$^{16}O_2$	$^{16}O^{18}O$	$^{12}C^{16}O_2$	$^{12}C^{16}O^{18}O$
I	1/2	1	0	0	0	0
g_a/g_s	3:1	1:2	0:1	0:1	0:1	0:1
even J	para-	yes	no	yes	yes	yes
odd J	ortho-	yes	yes	yes	no	yes

Table 2.1: The spin number I, statistical weight g_a/g_s, and existence of even and odd quantum number J for prominent diatomic and poly-atomic molecules are listed. Even and odd values of J for hydrogen are named as para- and ortho-hydrogen.

All previously described spin numbers I, the statistical weight g_a/g_s, and the existence of even and odd J numbers are illustrated in Tab. 2.1. Just from the intensity alteration within the rotational Raman spectrum of molecule, the nuclear spin number I can be determined after Eq. 2.11.

2.4 Signal-to-noise ratio and limit of detection

The limit of detection (LOD) is defined as the ability to extract analytical information from any spectroscopic technique. This limit within a quantitative analysis could be calculated by default with the concentration of a certain analyte yielding a signal-to-noise ratio (SNR) of 3 [127]. In the case of gas detection, one is usually interested in a minimum detectable concentration c_{LOD} or partial pressure p_{LOD} instead of the LOD, referring to less gas molecules compared to ambient conditions within a closed

system. The SNR itself represents the average peak height or area under the peak above the baseline for the intensity (total counts of area) of a Raman band S divided by its standard deviation σ_y. For very low analyte concentrations usually resulting in small peak intensities, the background noise of a neighboring region approximately equals to the standard deviation of the Raman peak. An accurate method to define σ_y relies on acquiring several spectrum repetitions, subtracting two successive spectra, and applying it to the noise around the peak region of σ_y.

For the evaluation of the SNR, the general noise σ_y originates from a number of sources as indicated by

$$\sigma_y = \left(\sigma_S^2 + \sigma_B^2 + \sigma_d^2 + \sigma_F^2 + \sigma_r^2 \right)^{1/2}, \tag{2.12}$$

where σ_S, σ_B, σ_d, σ_F, and σ_r are the standard deviations of analyte signal, background, dark signal, flicker noise, and readout noise, respectively. Other noise contributions such as additional stray light or room light are neglected in Eq. 2.12.

If the signal shot noise $\sigma_s = \sqrt{S}$ is the only noise source, the SNR becomes $S/\sqrt{S} = \sqrt{S}$ with S being the number of detected photoelectrons in counts per second registered above the background. Thus, the optimum measurement, i.e. 100 % quantum efficiency, 360° collection angle, and 100 % spectrometer transmission, as well as a zero background, is limited by this SNR [127]. The background noise σ_B is the result of luminescence of the sample or other optics and stray laser light, i.e. optics reflection or Rayleigh scattering. Contrary to detector and readout noise, it depends on the intensity of the laser and the sample luminescence. The background noise is also governed by shot noise and therefore it is $\sigma_B = \sqrt{B}$ for B being the number of detected photoelectrons in counts per second. This is observed when measuring very low concentrations of gas compounds, where the small gas peak usually appears among a high background noise signal. The dark signal originates from spontaneously generated electrons in the detector and is strongly temperature dependent. In the case of liquid nitrogen-cooled CCD detectors, this noise source is negligible for very low detector temperatures < -100 °C. Laser intensity variations will consequently cause Raman scattering variations in the measured signal and flicker noise σ_F would appear within this signal variation. Nowadays, power-stable, fan-cooled laser sources nearly eliminate this noise contribution.

The readout noise σ_r is a consequence of the analog-to-digital (AD) conversion of detector electrons to virtual counts by the spectrometer software next to contributions from thermal noise and electronic component noise. All these mentioned noise sources are strictly specified by the spectrometer manufacturer. The readout noise can be important for samples with very weak scattering, e.g. sensitive measurements with low gas concentrations of some parts per million (ppm). This noise is not time dependent, and thus the SNR will increase linearly in time. For strong Raman scattering of the sample, the overall noise will be mainly restricted by the analyte shot noise and scales by $\sqrt{t_S}$ for the measurement time t_S. While SNR and LOD characterize the quality of a single spectrum, the terms precision and accuracy relate to a set of multiple spectra and define the quality of measurement series, i. e. the reproducibility or repeatability for a value of interest such as the Raman signal amplitude. The precision though is connected to random errors, whereas accuracy is associated with systematic errors.

2.5 Quantitative Raman gas spectrometry

The scattering cross-section of the Raman effect is very low around 10^{-23} cm^2 sr^{-1} [55]. It yields an insufficient SNR especially in Raman gas sensing applications compared to well-known techniques in literature such as absorption spectroscopy. This drawback can be overcome with a proper experimental setup and several parameters can be exploited

to improve the increase of Raman scattered light and therefore the LOD. The observed Raman scattered light intensity I_R can be expressed by the simplified equation

$$I_R(\tilde{\nu}_R, \tilde{\nu}_0) = \eta\, I_0\, n\, \left(\frac{d\sigma(\tilde{\nu}_R, \tilde{\nu}_0)}{d\Omega} \right) \Omega\, L_e. \tag{2.13}$$

I_0 is the intensity of the exciting laser field; n is the molecule density of the measured gas (in parts per cm^3). The factor η represents the detection efficiency of the experimental setup and takes into account intensity losses related to the signal collection geometry, the optical components, i.e. mirrors or grating efficiencies, and the detector quantum efficiency. The parameter Ω contributes to the solid angle of the signal collection optics. The variable L_e is the effective scattering length of the sample volume. $d\sigma/d\Omega$, known as the absolute differential Raman scattering cross-section in units of $cm^2\,sr^{-1}$, is given by the following equation:

$$\left(\frac{d\sigma}{d\Omega} \right) = \frac{(2\pi)^4}{45} \frac{(\tilde{\nu}_0 - \tilde{\nu}_R)^4}{1 - \exp\left(-\dfrac{hc\tilde{\nu}_R}{kT} \right)} \frac{h}{8\pi^2 c\tilde{\nu}_R} \frac{1}{(4\pi\varepsilon_0)^2}\, g\,(45a^2 + 7\gamma^2). \tag{2.14}$$

Here, $\tilde{\nu}_0$ is the excitation wavenumber, $\tilde{\nu}_R$ the wavenumber of the Raman signal, g is the degeneracy of the Raman mode, a^2 and γ^2 are the isotropic and anisotropic parts of the polarizability tensor in units of $C^2\,V^{-2}\,m^4$. There is a linear relationship between the Raman scattered signal, the laser intensity, as well as the particle density of the gas (Eq. 2.13). The latter is proportional to the temperature and pressure in accordance to the ideal gas law. Therefore, the Raman signal scales linearly with a linear pressure increase, for example within a constant fiber core volume. In summary, there are manifold options to improve the performance, i.e. SNR, of a Raman gas sensor by utilizing higher laser powers, increasing particle pressure and collection angle, reducing gas particle temperature, or decreasing the laser excitation wavelength.

Raman scattering cross sections Rotational and vibrational effects of numerous different molecules are well characterized in literature [122, 77, 165]. For example the longest, i.e. energetically highest Raman shift is exhibited by the lightest gas molecule hydrogen with a Stokes shift of $4156\,cm^{-1}$ [77]. It defines the largest possible detection bandwidth for a Stokes Raman measurement of gaseous molecules [55, 165]. On the other hand, pure rotational transition lines with high signal intensities, i.e. a high excitation probability at room temperature, for a Stokes Raman spectrum can be usually found in the range of about $0 - 200\,cm^{-1}$ for common gas components, if these transitions are spectroscopically allowed. However, molecular hydrogen reveals pure rotational transitions detectable with adequate sensitivity in a wide wavenumber range from $300 - 1100\,cm^{-1}$ (cf. sub. 5.2.1).

In literature, the absolute Raman scattering cross section of the vibrational nitrogen frequency of $2331\,cm^{-1}$ is stated to be $3.30 \cdot 10^{-31}\,cm^2\,sr^{-1}\,mol^{-1}$ for an excitation wavelength of 488 nm and at ambient conditions [55] and changes to a value of $2.23 \cdot 10^{-31}\,cm^2\,sr^{-1}\,mol^{-1}$ ($0.82 \cdot 10^{-31}\,cm^2\,sr^{-1}\,mol^{-1}$) for a different excitation wavelength at 532 nm (660 nm). The absolute value is dependent on the excitation wavelength (cf. Eq. 2.14), which is expressed more general by

$$\left(\frac{d\sigma}{d\Omega} \right)_L = \left(\frac{d\sigma}{d\Omega} \right)_0 \cdot \frac{(\tilde{\nu}_0(\lambda_L) - \tilde{\nu}_R)^4}{(\tilde{\nu}_0(\lambda_0) - \tilde{\nu}_R)^4} \tag{2.15}$$

in accordance to the general λ^{-4}-dependency in Eq. 2.14. $(d\sigma/d\Omega)_L$ and $(d\sigma/d\Omega)_0$ represent the absolute differential Raman scattering cross sections for the excitation wavelength and reference wavelength. $\tilde{\nu}_0(\lambda_0)$ and $\tilde{\nu}_0(\lambda_L)$ are the Raman shifts for the reference laser wavelength λ_0 and the excitation laser wavelength λ_L, $\tilde{\nu}_R$ the Raman

shift for the specific vibrational or rotational Raman transition, all in units of absolute wavenumbers.

gas molecule	Raman transition	Raman shift (cm^{-1})	relative Raman scattering cross section*	reference
H_2	$S_0(1)$	587^r	4.66	[59]
	$S_0(2)$	814^r	0.65	[59]
	$S_0(3)$	1034^r	0.42	[59]
	$S_0(4)$	1243^r	0.01	[59]
H_2	$Q_1(1)$	4156^v	3.43	[55]
N_2O	$2\nu_2$	1168^v	0.08	[7]
	ν_1	1284^v	2.34	[55]
	ν_3	2224^v	0.51	[55]
$^{12}CO_2$	hot band	1270^v	0.08	[50]
	$2\nu_2$	1285^v	0.95	[55]
	ν_1	1388^v	1.48	[55]
	hot band	1410^v	0.14	[50]
$^{13}CO_2$	$\nu_1{'}$	1370^v	1.48	[55]
O_2	-	1556^v	1.28	[55]
N_2	-	2331^v	1.00	[55]
CH_4	ν_2	1535^v	0.10	[166]
	$2\nu_4$	2585^v	0.01	[37]
	ν_1	2917^v	5.78	[55]
	ν_3	3021^v	0.18	[37]
NH_3	ν_1	3334^v	5.00	[55]

Table 2.2: Assignment of individual Stokes Raman peaks (Raman transition and corresponding Raman shift in cm^{-1}) for prominent gas molecules and their relative Raman scattering sections referred to in this thesis together with stated literature reference values. (*, relative Raman scattering cross sections at λ_{exc} = 607 nm compared to that of nitrogen at 2331 cm^{-1}; ^{r}, rotational mode; ^{v}, vibrational mode)

The relative Raman scattering cross sections for numerously prominent gas molecules, which are detected throughout this thesis, were calculated for an excitation wavelength of 607 nm from reference data at different wavelengths and are shown in Tab. 2.2. On the one hand, the relative Raman intensities for an individual vibrational (rotational) transition next to the relative Raman scattering cross sections will change for different laser excitation wavelengths (cf. Eq. 2.15). On the other hand, the sensitivity and thus SNR of the Raman setup will change with varying Raman scattering cross sections for different excitation wavelengths. Lower wavelengths usually result in higher Raman scattering cross sections and therefore a theoretically higher SNR.

3 Linear optical properties of hollow-core photonic crystal fibers

In the year 1991, Philipp Russell first proposed a novel type of fiber, the so-called photonic crystal fiber [15, 14, 158]. The idea behind the invention was based on a microstructured region consisting of periodically arranged hollow-core air holes, which formed a 2-dimensional photonic crystal with an out-of-plane photonic bandgap. This novel type of optical waveguide can confine and guide light inside vacuum with a surrounding medium. In this chapter the idea of photonic crystals is first described and second followed by the description of a photonic crystal fiber (PCF) and its guiding mechanism. Next, HC-PCF and their optical properties will be introduced. Later, the signal collection and flow dynamics in a HC-PCF will be analyzed.

3.1 Photonic crystal

Photonic crystals (PC) are formed by periodic patterns in the scale of the effective optical wavelength. Electromagnetic waves propagating in a crystalline medium, which forms the PC, face periodic spatial variations of the refractive index n in the range of the incident light wavelength. As a consequence of this electromagnetic wave guiding, stop bands will emerge. They range in angle and frequency and will block the waves transmitting through the periodic structure. The incident light from an isotropic external medium experiences two effects, being either reflected or tunneled by the periodic structure. Only for special cases, these stop bands are able to prevent the light from propagating in all directions within a limited frequency region (and an incident angle range). In literature this is known as photonic bandgaps (PBG). A photonic bandgap belongs to the category of photonic crystals, but refers to at least 2 dimensions[1]. Contrary, an 1-dimensional photonic crystal is not a photonic bandgap. In comparison to the guiding mechanism of a photonic bandgap, the Bragg mirror demonstrates a similar but rather easier structure. It consists of concentric periodic refractive index alterations surrounding the core. This mechanism is based on Bragg's law:

$$n\lambda = 2 \cdot \Lambda \sin \Theta, \tag{3.1}$$

with Λ being the grating period, n the average refractive index, Θ the angle of incident, and λ the wavelength. For incoming light with sufficiently small incident angles, a strong light reflection will occur (Fig. 3.1). For the majority of reflections from each Bragg plane the Bragg condition becomes unconfined and thus for several Bragg planes, light will not penetrate the structure's center for a largely spanned angle. Light inside the center will be trapped by this 2-dimensional photonic bandgap vice versa (Fig. 3.1). The requirements are a sufficiently high refractive index contrast and an appropriate crystal lattice for such a PBG. Yablonovitch produced the first artificial 3-dimensional photonic structure providing a photonic bandgap in the GHz region [197, 198].

---

[1]The photonic bandgap of the later introduced photonic bandgap fiber (HC-PCF) represents a quasi-2-dimensional (or 2.5-dimensional) photonic crystal.
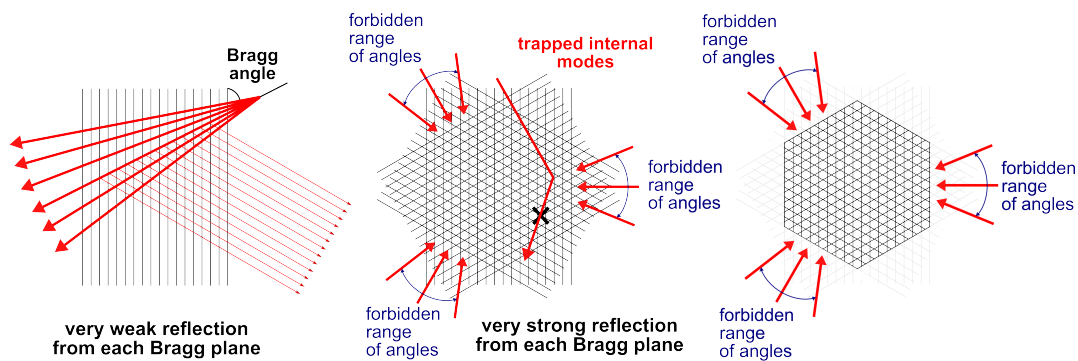
Figure 3.1: Exemplary graph for the Bragg reflection effect at periodic structured planes: Cumulative reflection at the Bragg angle (left), existence of a photonic bandgap by periodic plane sets (middle), and final hexagonal shaped plane set structure representing a photonic bandgap structure (right) are shown.

3.2 Photonic crystal fiber

The first satisfying PCF structure was drawn in 1995 [158, 159]. It was shown in literature, that PCF can confine more optical power, act as a more appropriate host for rare-earth ions like Yb^{3+}, Nd^{3+}, and Er^{3+} [51], have higher nonlinearities than standard optical fibers [159], can be produced in different designs with different dispersion features [10], and can be widely used for sensing applications [40, 38, 108, 107, 39]. Photonic crystal fibers with the characteristic microstructured cladding region can be classified into two categories, depending on the material that is forming the fiber core. If the core is hollow, the fiber will be named as hollow-core photonic crystal fiber (HC-PCF). If the core is solid, it will be referred to solid-core photonic crystal fibers (SC-PCF). In the following sections, these different optical fiber types will be discussed in terms of light guiding and optical properties [78].
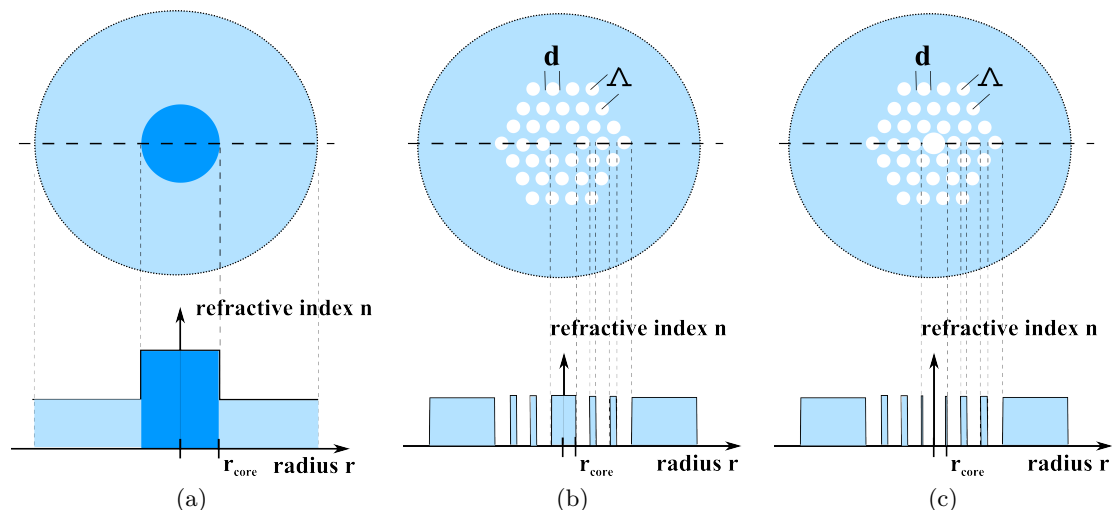
Figure 3.2: Cross-sections (top) and refractive radial index profiles (bottom) of (a) a step-index optical fiber, (b) a solid-core PCF, and (c) a hollow-core PCF. The hole diameter d and the pitch Λ for the microstructured cladding region of (b) and (c) are marked. Colors: light blue: fused silica, dark blue: doped silica, and white: air.

Similar to standard step-index optical fibers, SC-PCF reveal a positive refractive index difference with $n_{core} > n_{cladding}$. The refractive index reduction is achieved by the periodic structure of microscopic air capillaries along the whole fiber length (Fig. 3.2).

15

The effective refractive index of this microstructured region is a consequence of the air-glass phase relation with a generally smaller value than that of the undoped fused silica core. In SC-PCF, the light is guided by a modified total internal reflection (TIR). Fig. 3.2 shows the difference between standard step-index fibers, (undoped) SC-PCF, and HC-PCF. For photonic crystal fibers the parameters Λ and d are describing the hole-to-hole distance (i.e. pitch) and the hole diameter (Fig. 3.2).

The index guiding of a SC-PCF between solid core and the cladding region is shown for the E-field in Fig. 3.3a. The refractive index n of the silica core is higher than that of the silica-air cladding. Contrary, the perfect periodic structure creates a different E-field in the hollow core and the periodically microstructured region shown in Fig. 3.3b.
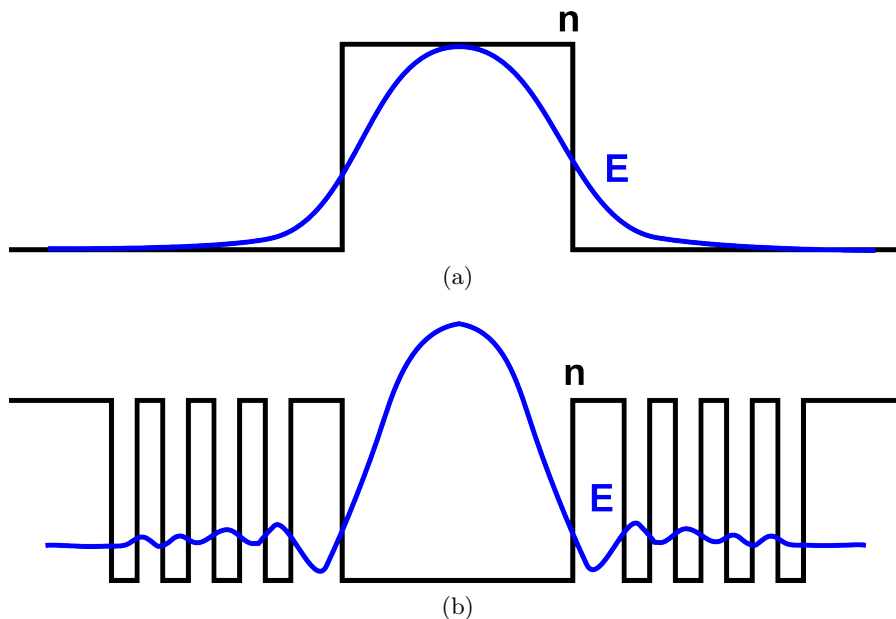
Figure 3.3: Variation of electric field E in (a) TIR propagation fiber (SC-PCF) and (b) HC-PCF.

3.3 Guidance mechanism in photonic crystal fibers

The wavevector parallel to the interface will be conserved for light, which enters any interface between materials. In general, the wavevector along z, which represents the direction of the fiber length, will be conserved for optical fibers. This parameter is represented as the propagation constant β in literature [136]. The free space vector $k_0 = 2\pi/\lambda$ defines the maximum allowed value for β, which is defined by $\beta = n \cdot k_0$ with n being the refractive index of the medium. Light will propagate entirely inside the medium along the fiber length in z-direction for β values higher than this cut-off number. It will be trapped in higher order refractive index regions such as in solid-core PCF with generally $n_{\text{core}} > n_{\text{cladding}}$, similar to standard step-index optical fibers. The light propagation in SC-PCF is usually shown in so-called propagation diagrams (Fig. 3.4). Therefore, the axes are normalized to the dimensionless axial wavevector $\beta \cdot \Lambda$ and the frequency $\omega \cdot \Lambda/c$. Λ defines the distance between neighboring air holes and c is the speed of light in vacuum. Light will only propagate in the medium as long as the propagation constant β fulfills the condition $\beta < n \cdot k_0$. These cases will be described in more detail for the solid-core PCF in comparison to the well-known optical step index fiber.

Optical step index fiber

Standard optical step index fibers usually consist of a solid fiber core with a refractive index higher than that of the fiber cladding. Let us consider a fiber core with refractive index $n = 1.47$, which is surrounded by the solid material cladding with $n = 1.45$ (Fig. 3.4 left). Four regions of propagation are defined by theory and can be identified:

Figure 3.4: Propagation diagram of step-index fibers (left) and solid-core PCF (right): The insights show illustratively the individual structure of each fiber. Framed numbers mark different regions for light propagation and will be discussed in this chapter. The horizontal line exemplarily shows the operation region of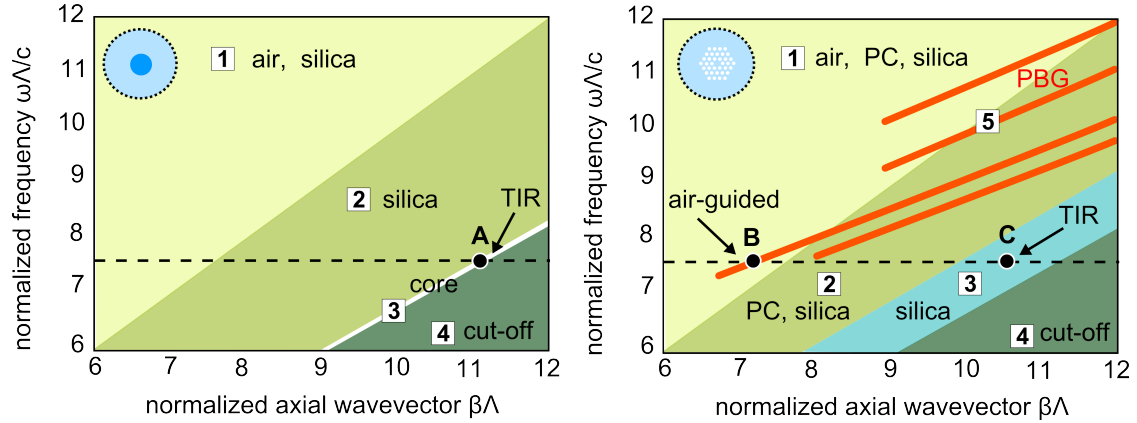 the fiber with $\beta = n \cdot k_0$, i.e. the light line. (TIR: total internal reflection, PBG: photonic bandgap, PC: photonic crystal)

- Region 1: $\beta < n \cdot k_0$ for core, cladding, and air with $n = 1$. Light can travel within or outside the solid fiber.

- Region 2: $\beta < n \cdot k_0$ for core and cladding, $\beta > n \cdot k_0$ for air. Evanescent light propagation will occur in air. Light is confined in the fiber core and cladding.

- Region 3: $\beta < n \cdot k_0$ exclusively for core, $\beta > n \cdot k_0$ for cladding and air. Evanescent light will propagate in the fiber cladding and in air. Only for this region, light will be confined and guided inside the core by total internal reflection (shown as an example in point A).

- Region 4: $\beta > n \cdot k_0$ for all values of n. No propagation of light for any medium. Light will be only evanescent in the core, cladding, and air for $n_{\text{cladding}} < \beta/k_0 < n_{\text{core}}$. This region is also known as cut-off. It is not possible to trap the light in a region with lower refractive index than that of the cladding for index guiding.

Solid-core photonic crystal fiber

Electromagnetic waves with an excitation frequency ω usually propagate through an isotropic homogenous medium with refractive index $n = n(\omega)$ and the previously described axial wavevector $\beta \leq n \cdot k_0$. A PC structure can be formed by a 2-dimensional periodic array of air holes in the glass substrate perpendicular to the normal light propagation in the fiber. The schematic structure of a SC-PCF was already shown in Fig. 3.2. This fiber is composed of pure silica without doping and a honeycomb-like microstructure of air holes within the 2-dimensional fiber cross section. The solid core is formed by absence of these air holes in the center of the fiber. The regions of propagation are similar to that of a solid optical step-index fiber:

- Region 1: $\beta < n \cdot k_0$ for core, cladding and air with $n = 1$. Light can travel within or outside the solid fiber like in conventional step-index optical fibers.

- Region 2: $\beta < n \cdot k_0$ for core and cladding, $\beta > n \cdot k_0$ for air. Evanescent light propagation will occur in air. Light is confined in the fiber core and cladding.

- Region 3: $\beta < n \cdot k_0$ for silica with $n = 1.45$. For the microstructured cladding region, the effective refractive index is lower due to the air holes and the air-to-silica relation. Thus, the propagation is forbidden. Light is allowed to travel either in the solid-core with surrounding microstructured region or in the pure silica around this cladding region. The light guidance is possible by TIR, shown as an example in point C (Fig. 3.2c).

- Region 4: $\beta > n \cdot k_0$ for all region with different refractive index n. For this cut-off region, only evanescent light will be transmitted in air and silica.

Hollow-core photonic crystal fiber

Both structures, which were previously described and are shown in Fig. 3.2c, do not require bandgaps to allow light propagation. However, specific features, i.e. "fingers" (Fig. 3.4 right, red lines) will appear for a PCF, but not for conventional step-index optical fibers. A general propagation in these regions is strictly forbidden due to certain β values, but photonic bandgaps appear as a consequence of the air hole silica structure in the microstructured cladding region (region 5 in Fig. 3.2c). These bandgaps can range into the propagation region 1, where light is free to propagate in air, in the solid core, and the PC. However for PCF fabricated with a hollow core, i.e. HC-PCF, light can propagate inside the air-filled core and will be confined by the surrounding bandgap cladding structure. Let us consider an incident excitation frequency, which cannot find any resonance to the PC with refractive index n_{PC}. As a result, the electromagnetic wave would be totally reflected. For a properly designed PBG, the light can propagate in a medium with $n < n_{PC}$ (for example for point B in Fig. 3.2c). The microstructured cladding of a HC-PCF should realize the light trapping in the hollow fiber core via a PBG, which is created by a honeycomb-like periodic array of micro-holes in the size of the wavelength (Fig. 3.2c).

Optical losses in photonic crystal fibers

Attenuation per unit of length, usually in units of dB/km, is one of the most important parameters in fiber optics, because it describes for example the maximum usable fiber length. For fiber-based Raman spectroscopic applications, the achievable sensitivity or LOD is, among others, a consequence of the applicable optical fiber length. The higher the fiber attenuation, the lower the effective fiber length will be. Longer fiber lengths will provide a larger analyte-light interaction along the fiber length and thus, more scattering molecules will be involved in the Raman process.

SC-PCF show familiar loss mechanisms like absorption and Rayleigh scattering in the bulk glass. Roughness of the hole boundaries can cause scattering losses as well, based on the thermally-excited surface capillary waves frozen in the fused silica fiber as it is drawn. The attenuation of conventional optical fibers is set to a limit of $0.15\,\mathrm{dB/km}$ at the telecommunication wavelength of 1550 nm due to the latter nano-scale imperfections, Rayleigh scattering, and absorption processes by transition metal ions and hydroxyl ions [29].

In HC-PCF, most of the light propagates in the air-filled hollow core, where all these processes are much less pronounced. The indirect leakage from the core via the power coupling from the core mode to surface modes is still the source of losses in HC-PCF. An improved fiber design can minimize this spatial mode overlap. The low loss record of $1.2\,\mathrm{dB/km}$ for a HC-PCF operating at 1620 nm was accomplished by Blaze Photonics Ltd. This was achieved through a high purity glass usage, which was prepared by

the vapor-phase axial deposition technique, and through the elimination of OH⁻ contamination [33]. The fiber attenuation could possibly be reduced to a practical value of 0.2 dB/km based on estimations of the still remaining loss due to imperfect fiber drawing [152].

(HC-)PCF suffer from bend-induced losses in the same manner as conventional optical step-index fibers. As a result, laser light and guided signal will leak out of the hollow core and couple into the microstructured region from fundamental to higher order modes. Bending radii are specified to minimum 3 cm for commercially available HC-PCF. Nevertheless, transmission features for wavelengths at the bandgap boundaries will be dramatically modified with smaller bending radii. This circumstance will be analytically described in Chap. 5. Additionally, an imperfect drawing process will introduce structural variations in the transversal and longitudinal fiber dimension. This results in an increased attenuation, which is a consequence of the high bandgap effect sensitivity due to structural imperfection.

3.4 Characteristics of hollow-core photonic crystal fibers (HC-PCF)

In general, HC-PCF can be categorized in two classes: the photonic bandgap (PBG) guiding mechanisms presented in this thesis, and the guidance based on inhibited coupling or von-Neumann-Wigner bound states in continuum. The latter is known as large-pitch Kagome-, or triangular-lattice HC-PCF[2] [36]. The Kagome fiber type provides ultra-broad band guidance (several hundreds of nm) at the expense of an increased attenuation. Contrary, commercial HC-PCF show typically attenuation with lowest of ~ 10 dB/km for optical guidance around 1550 nm [143]. The application of HC-PCF in the visible range increases the attenuation to a minimum value of 500 dB/km [145, 146, 144]. This is the consequence of the λ^{-3}-dependence for the attenuation values [9].
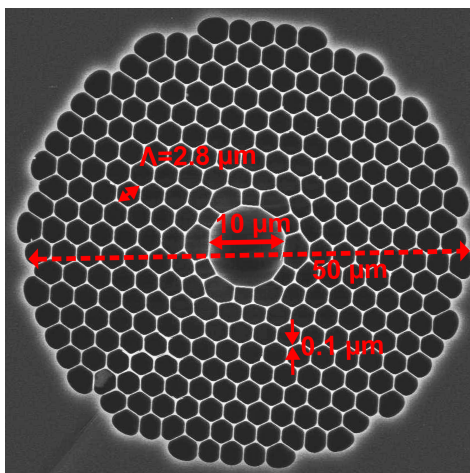
Figure 3.5: Scanning electron micrograph image for the cross section of the HC-PCF "HC-1060-02" (NKT Photonics) [142] including the hollow core, a microstructured region, and the solid cladding region.

Hollow-core photonic bandgap (HC-PBG) fibers entail a central defect, i.e. a hollow core, in the microstructured cladding. This core is usually composed of a 1, 7, or 19 missing hole(s) structure. In the case of a 7-cell HC-PCF, the core is formed by removing

---

[2]If not different stated, the abbreviation "HC-PCF" refers to hollow-core PBG fibers, not Kagome fibers, without exception within this thesis.

7 capillaries from the cladding. A typical HC-PBG fiber (model "HC-1060-02", NKT Photonics) with a 7-cell structure, operating in the IR range, is shown in Fig. 3.5. The microstructured fiber cladding region features a pitch Λ of 2.8 µm, a fiber core diameter of 10.0 µm, and a strand thickness of ~ 0.1 µm (Fig. 3.5). The diameter of the whole centrosymmetric microstructured region is 50 µm and the fiber diameter sums up to (123 ± 5) µm [142]. These structure parameters will define the guidance properties of the fiber.

More than 95 % of optical power is located in the form of a Gaussian-like fundamental mode in the air-filled hollow core with an effective mode index of 0.99 [145]. The hollow-core structured cladding normally contains minor glass content. Thus the air-filling fraction can reach values higher than 90 %. The *NA* of the HC-PCF is specified to ~ 0.2, which should be matched by a proper lens for the laser beam coupling.

The HC-PCF is characterized by a PBG with low attenuation restricted by a certain wavelength region. For the presented PBG fiber in Fig. 3.5, the spectral transmission window spans approximately from $1010 - 1130$ nm [142]. Characteristic loss spectra for the differently applied HC-PCF, operating in the VIS range, are shown in Fig. 3.6 and will be of importance for the second part of this thesis.
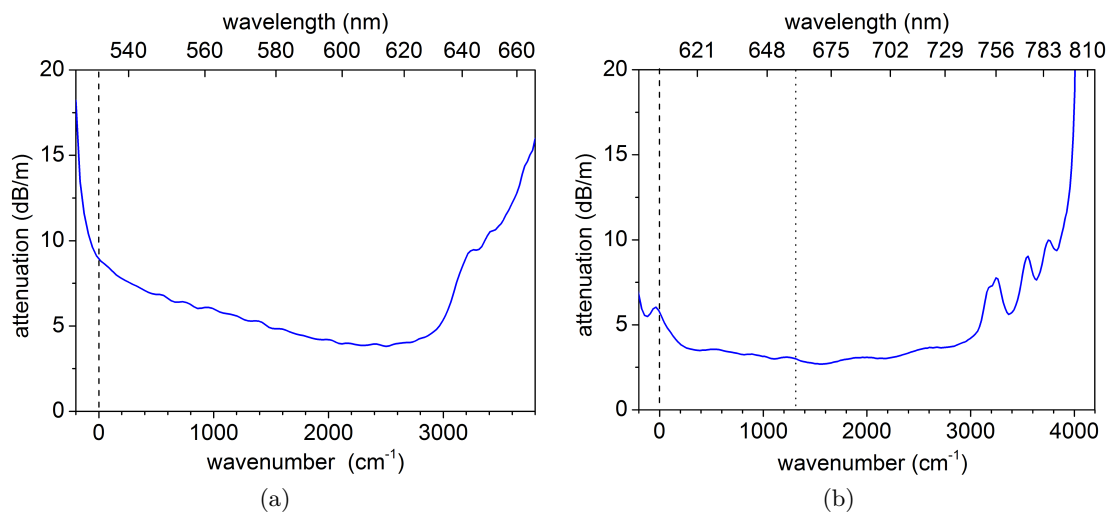
Figure 3.6: Measured attenuation graph for the applied HC-PCF of (a) "HC-580-02" and (b) "HC-633-02" from NKT Photonics: The dashed lines represent the laser wavelength at 532 nm in (a) and 607 nm in (b), respectively. The dotted line in (b) illustrates another excitation wavelength at 660 nm utilized for this thesis. Graph generated from data provided by [82, 79].

3.5 Raman signal collection for HC-PCF

3.5.1 Backward and forward simulated Raman scattering in HC-PCF

The fiber attenuation characteristic will primarily determine the useful length of a Raman cell. The loss, or attenuation α in m^{-1}, at a particular wavelength is determined by a number of different factors. In the case of PBG fibers, the loss is a function of the 2-dimensional bandgap geometry, as well as structure imperfections originating from the fiber-drawing process. Attenuation losses for the excitation laser wavelength with initial intensity I_0 are physically expressed by α_L. The laser intensity I_L at any point x along the fiber length L is then given by Beer-Lambert law with $I_L = I_0 \cdot \exp\left(-\alpha_L x\right)$.

The Raman signal I_R scales naturally linear with the probe volume length (Eq. 2.13). The fiber transmission losses for laser light and Raman signal will modify this scaling. The collection of the Raman signal can be distinguished between a forward scattering and backward scattering arrangement resulting in a Raman signal intensity difference. In

general, the specific application goal must be considered for the design of a fiber-based Raman setup. The effective fiber length $L_{\text{eff}}^{\text{for}}$ and $L_{\text{eff}}^{\text{back}}$ for a forward and backward scattering arrangement with fiber length L is defined by [4]

$$L_{\text{eff}}^{\text{for}} = \frac{e^{-\alpha_L L} - e^{-\alpha_R L}}{\alpha_R - \alpha_L} \text{ and} \tag{3.2}$$

$$L_{\text{eff}}^{\text{back}} = \frac{1 - e^{-(\alpha_L + \alpha_R)L}}{\alpha_R + \alpha_L}, \tag{3.3}$$

where α_L and α_R in m^{-1} represent the attenuation of the excitation laser light and the Raman signal at a specific Raman frequency. Both attenuation factors are governed by the attenuation profile of the fiber (Fig. 3.6). The maximum effective fiber lengths $L_{\text{eff,max}}^{\text{for}}$ and $L_{\text{eff,max}}^{\text{back}}$ for forward and backward Raman scattering in HC-PCF are [4]

$$L_{\text{eff,max}}^{\text{for}} = \frac{\left(\frac{\alpha_R}{\alpha_L}\right)^{-\alpha_L/(\alpha_R - \alpha_L)} - \left(\frac{\alpha_R}{\alpha_L}\right)^{-\alpha_R/(\alpha_R - \alpha_L)}}{\alpha_R - \alpha_L} \text{ and} \tag{3.4}$$

$$L_{\text{eff,max}}^{\text{back}} = \frac{1}{\alpha_R + \alpha_L} \tag{3.5}$$

for $\alpha_L \neq \alpha_R$. According to manufacturer specifications for the commercial HC-PCF "HC-633-02" [146] together with the Eq. 3.4-3.5, maximum effective fiber lengths of $L_{\text{eff,max}}^{\text{for}} = 0.55\,\text{m}$ and $L_{\text{eff,max}}^{\text{back}} = 0.43\,\text{m}$ are resulting for an excitation wavelength of $660\,\text{nm}$ and the Raman signal of rotational hydrogen band $S_0(1)$ at $587\,\text{cm}^{-1}$ (cf. Tab. 2.2 and Fig. 3.6).
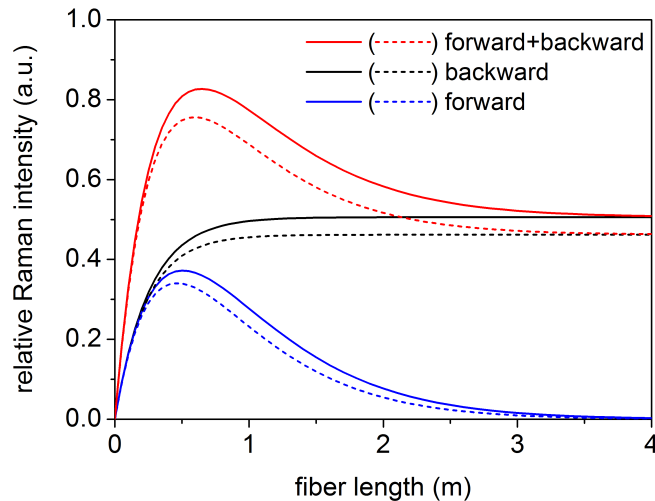
Figure 3.7: Simulated relative Raman intensity vs. effective fiber length for the HC-PCF "HC-633-02" [146] and an excitation wavelength at 660 nm referring to the rotational hydrogen band $S_0(1)$ at $587\,\text{cm}^{-1}$ (solid) and vibrational band of oxygen at $1556\,\text{cm}^{-1}$ (dashed) in accordance to Fig. 3.6 and Eq. 3.2-3.3 for 3 different scattering geometries in comparison: forward (blue), backward (black), and combined forward with backward Stokes scattering (red).

The difference between backward and forward scattering signal guidance in HC-PCF is shown in Fig. 3.7. The Raman signal increases exponentially for both scattering arrangements according to Eq. 3.2-3.3. Nevertheless, higher Raman intensities can be realized for longer fiber lengths for backward Raman scattering in HC-PCF since the signal intensity increases exponentially to a maximum effective length (Fig. 3.7, black curve). The strongest Raman intensity is generated at the fiber input for unattenuated laser light and Raman signal. The guided laser light along the fiber will be consequently

attenuated at longer fiber lengths, producing less Raman signal. Additionally, this Raman signal has to be transmitted back to the fiber input, what is accompanied by higher fiber losses. Increasing the fiber length to values larger than the effective length will lead to saturation in achievable Raman signal, since the additionally transmitted Raman signal will be attenuated to zero (Fig. 3.7, black curve). For forward scattering the highest Raman signal will be generated at the fiber input and will be also transmitted longest in the fiber. Hence, it will experience the highest loss (Fig. 3.7, blue curve). Increasing the fiber length introduces more signal loss and the higher attenuated laser light will generate less additional Raman signal at fiber positions close to the fiber outlet. Increasing the fiber length to large values will fully attenuate the forward guided Raman signal to zero (Fig. 3.7, blue curve). The combination of both signal collection arrangements in forward and backward scattering will theoretically lead to a stronger exponential increase in Raman signal until the maximum effective length is reached [4]. Longer fiber lengths will exponentially decrease the Raman intensity, comparable to forward scattering until the saturation maximum of backward scattering (Fig. 3.7, red curve).

3.5.2 Silica Raman background of HC-PCF

The here introduced microstructured optical fibers are made of undoped fused silica, i.e. quartz glass material. The thin silica strands with a thickness of ~ 100 nm form the hexagonal-shaped air capillaries of the microstructured region. The guided excitation laser beam inside the hollow core along the fiber will penetrate into the surrounding microstructured region formed by these miniaturized silica strands. Thus, the fused silica structure essentially produces parasitic silica Raman signal, which will be guided with low loss inside the hollow core as well. Based on the intrinsically higher absolute Raman cross section of the fiber glass material compared to the weaker of gas molecules, the resulting larger silica Raman background has to be cleared out for highly sensitive Raman gas spectroscopy. Additionally, general bandgap structure imperfections along the HC-PCF will generate higher losses connected to a larger content of parasitic silica Raman signal guided inside the air-filled core. The small HC-PCF core diameter of ~ 5 µm introduces a tradeoff between a minimum focus diameter and matching the acceptance NA of the fiber. High NA microscope objective lenses guarantee a minimum focal diameter of several micrometer smaller than the fiber core, but also have a larger NA than the fiber acceptance NA. Thus, silica Raman signal in the microstructured silica cladding will be generated by the laser light that cannot be guided in the air-filled core. The application of a small NA objective lens is normally limited to a minimum focus spot diameter larger than the fiber core diameter. Similarly, the holey cladding region surrounding the hollow core produces parasitic silica Raman signal next to the analyte signal collected by the lens optics. The right choice of magnification and lens NA in advance will minimize the interfering Raman signal content of fused silica.

A typical silica Raman spectrum originating from the silica microstructured region of a HC-PCF is shown in Fig. 3.8. SiO_2 mainly consists of six-membered rings at ambient conditions (compare the inset in Fig. 3.8). The W_1 band between $200 - 500 \, cm^{-1}$ generally reflects the six-member ring behavior and is associated with the Si-O-Si bending motion, i.e. a symmetric stretching of the bridging oxygen. The defect bands D_1 and D_2 at 495 cm^{-1} and 606 cm^{-1} are associated with breathing modes of three- and four-membered rings [163]. The W_3 band at 820 cm^{-1} arises from an unresolved TO-LO phonon pair, whereas the W_4 band is related to a TO and LO phonon at around $1060 \, cm^{-1}$ and 1190 cm^{-1}. The Raman spectrum at wavenumbers larger than 1200 cm^{-1} is dominated by a certain fluorescence background extending to higher wavenumbers [192].
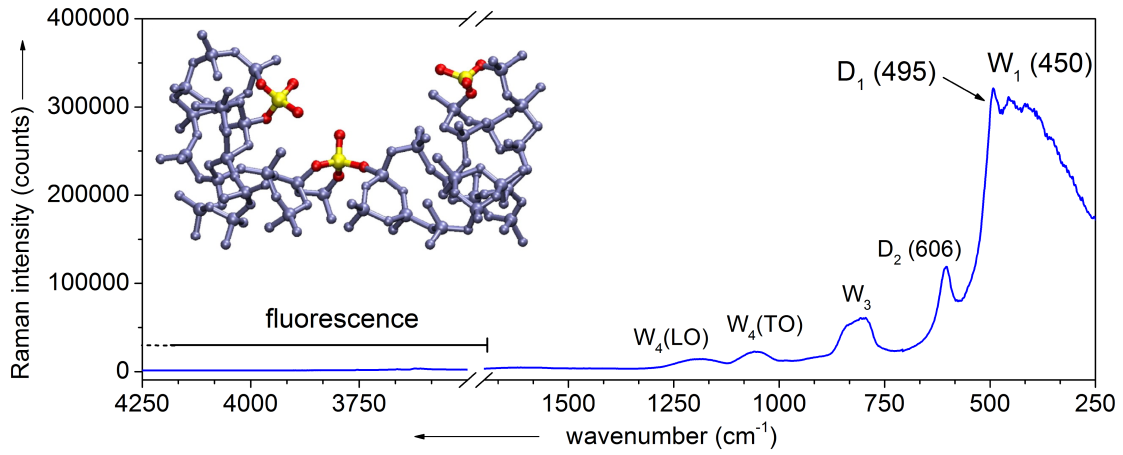
Figure 3.8: Raman spectrum of undoped fused silica obtained with a 532 nm laser and the HC-PCF "HC-580-02" [145]. Inset: Illustration of amorphous silica showing Q2 and Q3 species as tetrahedral with two and three coordination to the surface, respectively [46].

The detection of vibrational Raman bands of gaseous compounds is presented in a large wavenumber region up to 4200 cm^{-1}. The pure rotational band structure of molecular gas components can span up to wavenumbers of 4200 cm^{-1}, e.g. for molecular hydrogen. These bands in this low spectroscopic fingerprint region can in general be detected on a high fused silica Raman background (Fig. 3.8). The silica Raman noise of individual bands will significantly contribute to the individual peak noise of the investigated Raman band. Consequently, the SNR will be reduced by the additional silica noise contribution, as well as the potentially lower signal peak intensity. This will be quantitatively discussed in Chap. 6. For extremely sensitive Raman spectroscopic multi-gas sensing in the ppb-concentration range, a reduction of this silica Raman noise has to be accomplished.

The introduction of spatial filtering by different spectrometer functions represents a feasible option for a consequent silica Raman noise reduction originating from the microstructured cladding region and outer core region [82]. Guided silica Raman signal inside the fiber core can be further cut out by additional spatial filtering within the fiber image plane. Both methods will be discussed in Sec. 6.1.

3.6 Gas flow dynamics in HC-PCF

For the Raman spectroscopic detection of different gas compounds together with HC-PCF, the gaseous analytes will be introduced to the hollow core, where most of the exciting laser light is guided. This effectively creates a great interaction path between light and the gaseous analyte along the whole fiber length. There are two ways to introduce gas molecules into the fiber, either by diffusion or a gas flow as a consequence of a pressure gradient along the fiber length

3.6.1 Diffusion

The gas composition can gradually penetrate the fiber by diffusion. This diffusion can be characterized by a relative concentration of gas inside the fiber averaged over the fiber length. This concentration C is found by the integration of local concentrations obtained by solving the diffusion equation with corresponding boundary conditions. This is expressed by the following infinite sum:

$$C = 1 - \frac{8}{\pi^2} \sum_{j=1,3,5}^{\infty} \frac{1}{j^2} \exp\left[-\left(\frac{j\pi}{iL}\right)^2 Dt \right], \quad (3.6)$$

23

where L is the fiber length, D the diffusion coefficient for the individual gas component, and t the time. For example, the value of D for molecular hydrogen (methane) in ambient air is $0.627\,\mathrm{cm^2\,s^{-1}}$ ($0.106\,\mathrm{cm^2\,s^{-1}}$) for $p = 101.325\,\mathrm{kPa}$ and $T = 293.15\,\mathrm{K}$ [119]. The factor i in Eq. 3.6 equals two values: $i = 1$ is used for two open fiber ends, $i = 2$ for one end opened. Applying the diffusion coefficient for hydrogen in ambient air, the dependence of the average relative concentration vs. time for 4 different fiber lengths with one or both ends opened is plotted in Fig. 3.9. As expected, the diffusion into the microstructured fiber for both ends opened is realized significantly faster than for one opened end (Fig. 3.9). It has to be mentioned, that surface effects of the inner fiber core were neglected. This was ensured by the considerably larger fiber core diameter of some µm in comparison to gas molecule diameters $< 1\,\mathrm{nm}$. Table 3.1 summarizes the total time t_{90} to fill the hollow fiber core with 90 vol. % hydrogen or methane in ambient air for 4 different fiber lengths analogous to Fig. 3.9.
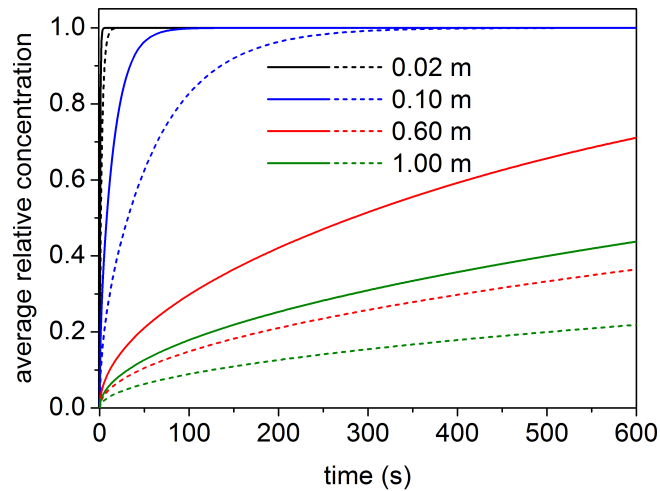
Figure 3.9: Time-dependence of the average relative hydrogen concentration in ambient air inside a HC-PCF with core diameter of 6 µm and different lengths of 0.02 m (black), 0.1 m (blue), 0.6 m (red), and 1.0 m (green) for one end opened (dashed lines) and two ends opened (solid lines) was simulated and is illustrated.

fiber length L (m)	t_{90} (H_2) (s)		t_{90} (CH_4) (s)
	1 open end	2 open ends	2 open ends
0.02	6	2	8
0.10	136	34	200
0.60	4869	1218	7200
1.00	7523	3380	19998

Table 3.1: Expected time t_{90} to obtain 90 vol. % average hydrogen or methane concentration in ambient air for diffusion into the hollow core of a HC-PCF with different fiber lengths L for one and both fiber ends opened at ambient conditions, respectively.

Because the Raman signal scales exponentially with the fiber length, realistic effective fiber lengths will scale in the range of $0.5 - 1.2\,\mathrm{m}$ for the presented HC-PCF. The fiber filling by diffusion would result in measurement times in the range of minutes to hours for a complete filling of the core with gaseous analytes (Tab. 3.1). Moreover, the introduction of a multi-component gas mixture with different diffusion constants would result in different diffusion speeds. However, real-time gas sensing applications demand a general detection of concentration changes in the low second range. Conclusively, a

quantitative gas sensing in HC-PCF in combination with filling times of less than several seconds cannot be covered by the diffusion regime.

3.6.2 Flow regime

The determination of flow characteristics inside a capillary or microstructured hollow-core fiber is based on kinetic molecular principles, driven by a pressure gradient between both fiber ends. In general, the flow of gas compositions is governed by the dimensionless Knudsen number, $K_n = \lambda_m/d$, with λ_m being the mean free path of a gas molecule and d the capillary or hollow core diameter [11, 86]. High Knudsen numbers, i.e. $K_n \gg 1$, indicate a region of free molecular flow, where molecules most likely collide with the inner capillary walls, rather than with each other. Knudsen numbers around 1 define a so-called slip or transitional flow, where intermolecular collisions and wall collisions play an important role for capillary flow characteristics. Small values of K_n describe the hydrodynamic or Poiseuille flow region, characterized by a parabolic flux variation across the capillary radius with almost zero flow near the tubing walls.

The mean free path can be determined by $\lambda_m = k_B T / \left(\sqrt{2} \, \pi \, d_m^2 \, p \right)$ with k_B the Boltzmann constant, T the temperature, d_m the molecule diameter, and p the pressure. Using an exemplary HC-PCF core diameter of 5.8 µm and a mean free path of $\lambda_m = 58.8\,\text{nm}$ for molecular nitrogen (at atmospheric pressure and $T = 273.15\,\text{K}$) [88] results in a Knudsen number of 0.01, i.e. the Poiseuille flow regime [86].

Poiseuille flow assumes a dynamic viscosity η for the flowing gas, which is independent of the pressure p. The change in volume dV within the time dt is then given by [105]

$$dV = \frac{\pi r^4 \Delta p}{8 \eta L}\, dt \,, \tag{3.7}$$

with r being the capillary radius, Δp the pressure difference between both fiber ends, and L the capillary/fiber length. A steady-state flow was assumed, i.e. non-changing pressures at any point in the system. In a steady-state flow system, the filling time of the capillary's inner volume can be estimated as

$$t_{\text{fill}} = \frac{8 \eta L}{\pi r^4 \Delta p} V = \frac{8 \eta L^2}{r^2 \Delta p}. \tag{3.8}$$

The filling time scales with the square of the capillary length L and anti-proportional to the square of the capillary radius r. Therefore, filling times are significantly dependent on length and core diameter of a microstructured photonic crystal fiber. Figure 3.10 shows the estimated filling times for two different fiber lengths 0.3 m and 1.0 m with varying differential pressure from $0 - 19\,\text{bar}$. The filling time between the hollow core with diameters of 5.8 µm and 6.6 µm and the small holes of the microstructured cladding region with diameter size of $\sim 1\,\text{µm}$ are compared exemplary for "HC-580-02" and "HC-660-02". The Poiseuille regime for filling the fiber indicates mainly reduced gas analyte filling times for short enough fiber lengths in combination with high input pressures much larger than the ambient pressure [135].
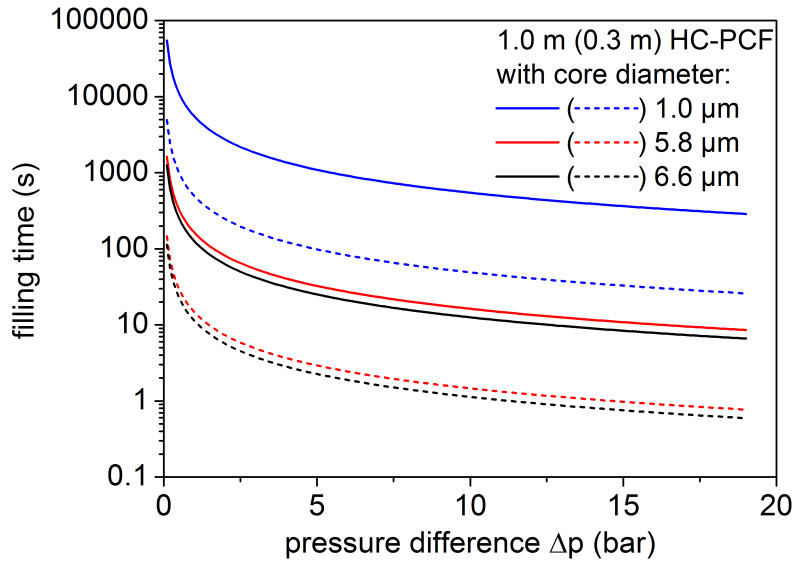
Figure 3.10: Simulated filling time of a HC-PCF with fiber core diameters of 5.8 µm (red) and 6.6 µm (black) compared to that with a core diameter of $\sim 1\,\mu m$ (blue) for the microstructured cladding region: The filling gas is ambient air with a dynamic viscosity of 17.1 µPa s (at 273.15 K) [119]. Two different fiber lengths, 0.3 m (dashed lines) and 1.0 m (solid lines), are considered according to Poiseuille flow regime (Eq. 3.10).

Only for high pressures (> 10 bar) and short fiber lengths (< 0.3 m), the filling time would take some seconds, exemplarily shown in Fig. 3.10 for the HC-PCF "HC-580-02" and "HC-633-02" with hollow-core diameters of 5.8 µm and 6.6 µm. Contrary, small pressure differences will significantly increase the filling time for gaseous analytes to several hundreds of seconds. Furthermore, the filling times for an individual cladding hole are around some hundreds of seconds (Fig. 3.10). It has to be mentioned, that the successful filling of hollow core and microstructured region within several seconds cannot be achieved at the same time, even for very short fiber lengths in combination with high gas pressures. Because their will be no relevant Raman signal contribution from the microstructured cladding region, gas residuals inside the small hollow capillaries from a previous concentration detection will be of no effect for any real-time gas monitoring application.

All in all, the trade-off between sensing speed and detection sensitivity has to be stressed out. Fiber lengths much shorter than the optimum effective fiber length lead to a rapid analyte filling of the fiber core, but the absolute sensor sensitivity ability is decreased by a reduced analyte Raman signal generation along the fiber. Fiber lengths around the optimum effective fiber length in dependency of the fiber attenuation will increase the analyte Raman scattering output at the expense of longer filling times (Fig. 3.10). The different fiber length for each experiment is consequently stated in this thesis.

4 Fiber-enhanced Raman spectroscopy with HC-PCF

The challenge in Raman spectroscopy is that it is based on the Raman effect, which is intrinsically weak compared to other effects like fluorescence or photon absorption. About one out of 10^6 photons will be inelastically scattered by the Raman effect [77]. Introducing conventional Raman spectroscopy to a competitive multi-gas sensor technique, a tremendous enhancement for compensation of the generally very low absolute scattering cross sections for gas molecules with $\sim 3.3 \times 10^{-31}$ cm^2 sr^{-1} mol^{-1} [55] has to be applied. And here the HC-PCF as a novel type of fiber comes into play. This fiber realizes enhanced light-analyte interaction over long optical path lengths and for very small sample volumes less than 1 µL inside the hollow core. In this chapter, a fiber-based Raman system utilized for the quantification of gas concentrations will be described and characterized. Finally, quantitative fiber-enhanced Raman measurements in the field of biogene gas sensing and human breath analysis are presented.

4.1 Fiber-enhanced Raman spectroscopic (FERS) setup

The basic fiber-based Raman spectroscopic setup for the quantitative analysis of multi-gas samples illustrated in Fig. 4.1 will be briefly described. In the following sections, each individual optical component will be characterized in more detail. Changes of individual components or analysis procedures between certain measurements will be indicated at the paragraphs if necessary. Subsequent software procedures and methods for processing of raw data are discussed below in section 4.2.

4.1.1 General setup for Raman measurements

The presented fiber-based Raman spectroscopic setup consists of 3 switchable continuous-wave (cw) operated diode-pumped solid-state (DPSS) lasers. The individual laser beam passes through a Keplerian telescope (T) with different possible magnification, after being reflected by a dichroic mirror (DC) into a microscope objective lens (OL), which focuses the excitation laser light into the microstructured optical fiber (MOF). Both fiber ends are fixed in specially constructed fiber adapter assemblies designed by Di Yan [62] (A_1, A_2 with input (I) and output (O) port), which sit on a three-axis nano-positioning system (model "MAX313D", Thorlabs Inc.). The transmitted laser light is measured by a powermeter (PM: model "PM100D, Thorlabs Inc.) at the other fiber end (A_2). The backscattered Raman signal from one fiber end (A_1) is collected by the objective lens and passes the dichroic mirror (DC) before a Raman edge filter (E), which additionally blocks the strong Rayleigh signal for each laser wavelength. A pinhole (P) spatially filters the Raman light. The Raman signal is focused by an achromatic lens (L) on the slit of the spectrometer (SPEC) and is imaged onto a liquid nitrogen (LN$_2$) cooled CCD detector.
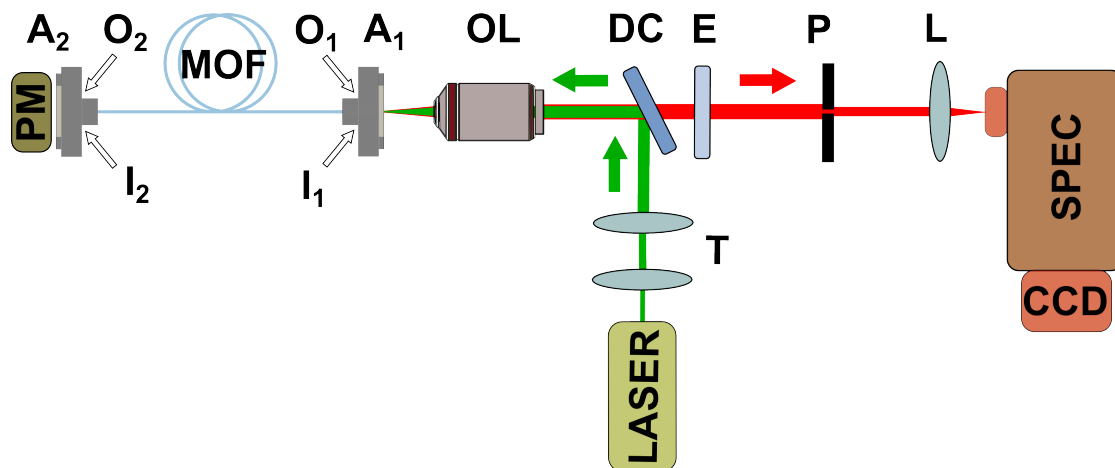
Figure 4.1: Design of the fiber-enhanced Raman spectroscopic setup, consisting of a laser, Keplerian telescope (T), long-pass dichroic beam splitter (DC), objective lens (OL), fiber adapter assembly (A_1 and A_2 with input (I_1, I_2) and output (O_1, O_2)), microstructured optical fiber (MOF), powermeter (PM), pinhole (P), edge filter (E), aspheric lens (L), spectrometer (SPEC), and CCD detector, is shown.

4.1.2 Laser source

Normally, commercially available Raman systems are equipped with lasers with some hundred milliwatts of output power. However, the low particle density of gases at atmospheric pressure in combination with intrinsically low Raman scattering cross sections demand higher laser power for compensation. For the presented setup, the signal can be generated by 3 switchable lasers, two frequency-doubled Nd:YAG lasers at 532 nm (model Opus) and 660 nm (Model Lux) from LaserQuantum Ltd., and a single-frequency laser at 607 nm from Lasos Lasertechnik GmbH. These lasers are all cw-operated DPSS lasers with maximum output powers of up to 3.2 W (Tab. 4.1).

parameter/model	Opus [124]	Lasos [71]	Lux [123]	unit
wavelength	532.2	606.5	659.3	nm
bandwidth	1.0	0.8	1.0	cm^{-1}
power	3.2	0.06	1.0	W
beam diameter	1.8	0.7	0.65	mm
M^2	1.1	1.0	1.2	-
divergence Θ	0.4	1.1	1.5	mrad
rms noise	0.4	1.3	0.6	%

Table 4.1: An overview of the selected cw-operated DPSS lasers referring to important system parameters, which had to be considered for FERS measurements within this thesis, is presented.

They generally feature excellent beam quality expressed by the measurable quality factor M^2, ranging from 1.0 - 1.2 (Tab. 4.1). The pointing and power stability of DPSS lasers, as well as the wavelength stability, can be strongly improved by the temperature stabilization of the laser ground plate. Accordingly, the lasers were equipped with a thicker fan-cooled laser plate. The laser temperature was stabilized down to $\Delta T = 0.1\,K$ resulting in general power stabilities better than 0.3 %. The experimentally determined power stability for 200 mW with a standard deviation of 0.04 % for the temporal discretization of 1 second is shown in Appendix A.2. The power stability, next to the

stability of the laser beam coupling, is crucial and the main source for the overall error of the quantification process.

4.1.3 Coupling optics

Cw-operated DPSS lasers often radiate laser beams in the form of a spatial Gaussian beams [169]. These beams can be described by the Gaussian function $I(r, z) = P/\left(\pi\, w(z)^2/2\right) \cdot \exp\left(-2\, r^2/w(z)^2\right)$ [136]. Here, $w(z)$ is the beam radius at position z, r is the radial distance from the center axis of the beam, and w_0 the distance from the beam axis where the laser intensity I drops to $1/e^2$ of the maximum value. The beam radius varies along the propagation direction according to [136] by

$$w(z) = w_0\sqrt{1 + \left(\frac{z}{z_R}\right)^2}\,,\qquad(4.1)$$

with the minimum beam waist w_0. The Rayleigh length $z_R = M^2\, \pi\, w_0^2/\lambda$ determines the length over which the beam can propagate without diverging significantly. The beam divergence Θ in the far field with $z \gg z_R$ is defined by $\Theta = M^2\, \lambda/(\pi\, w_0)$ [136]. If the fundamental mode TEM_{00} with diameter $2\, w_0$ is focused by a lens with focal length f, the beam waist w_f represents the distance from the beam axis at the focus plane given by

$$w_f = \sqrt{w_0^2 \frac{f^2}{z^2 + z_R^2}}\,.\qquad(4.2)$$

For the special case $z \gg z_R$, i.e. a well-collimated laser beam, with the additional condition $z_R \gg f$, the beam waist w_f can be calculated by

$$w_f = M^2 \frac{\lambda\, f}{\pi\, w_0}.\qquad(4.3)$$

Increasing the laser beam diameter consequently decreases its divergence with the relation $d \times \Theta = \mathrm{const.}$ for small Θ. A telescope consisting of 2 lenses with focal lengths f_1 and f_2 is used to expand (or decrease) the beam diameter (divergence) by the magnification $A = |\, f_2/f_1\,|$ together with the resulting divergence $\Theta' = \Theta/A$.

telescope	laser	λ (nm)	laser beam diameter (mm)	$2\, w_f$ (µm)	NA_{eff}
w/o	Opus	532	1.8	3.8	0.09
	Lasos	607	0.7	5.3	0.04
	Lux	660	0.7	5.2	0.03
w	Opus	532	3.6	3.3	0.18
	Lasos	607	3.5	4.3	0.18
	Lux	660	3.3	4.0	0.16

Table 4.2: An overview of the calculated beam diameter $2\, w_f$ in the focal plane and the effective numerical aperture NA_{eff} for the used microscope objective lens, according to the laser parameters from Tab. 4.1, is presented. All values for the setup without (w/o) telescope and with (w) telescope are listed. The laser beam at 532 nm was magnified by a factor of 2, the laser beams at 607 nm and 660 nm by a factor of 5.

Laser light, that is coupling into the fiber, should always match the fiber acceptance numerical aperture NA_{fiber}. The magnification of an objective lens is a function of

the effective lens numerical aperture NA_{eff}. Laser beams smaller in diameter than the objective lens aperture result in a smaller objective lens numerical aperture $NA_{objective}$. Matching the objective lens' numerical aperture $NA_{objective} = NA_{eff}$ to NA_{fiber} is of great experimental importance: Small excitation laser beam diameters resulting in $NA_{eff} \ll NA_{fiber}$ lead to larger focal beam diameters $2\,w_f$ than the fiber core diameter. Large laser beam diameters, characterized by $NA_{eff} \gg NA_{fiber}$ (and usually generated by the application of a beam magnification telescope), have the effect of smaller focal spot diameters (cf. Tab. 4.2). For both cases, parasitic silica Raman signal will be generated as previously discussed (cf. Sec. 3.5.2).

The calculated values of beam diameter $2\,w_f$ and effective numerical aperture NA_{eff} for the 3 different lasers comparing the implementation of a telescope and without one are shown in Tab. 4.2. Adjusting the NA_{eff} to the value of ~ 0.2 by the setup-implementation of a telescope (T, Fig. 4.1) leads to smaller focal beam diameters compared to no NA matching (Tab. 4.2), which is the first step to ensure a minimization of parasitic silica Raman signal.

4.1.4 Fiber assembly and filling

In order to quantify reliable and continuously monitor a multi-gas composition, special fiber assemblies were designed by Di Yan [62] to achieve the essential, highly stable optical coupling. The adapters for each end of the fiber solved several critical tasks at the same time: (1) the laser coupling and collection of the Raman backscattered light through an optical window, (2) the collection mainly of the transmitted laser light for permanent monitoring with a powermeter, and (3) the fast reproducible gas flushing of the fiber with a multi-gas composition. The schematic design is shown in Fig. 4.2.
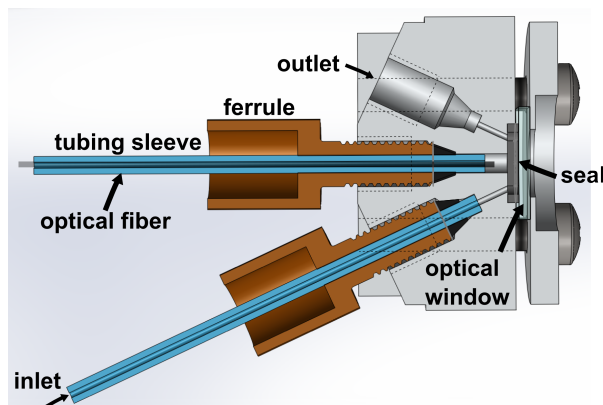

Figure 4.2: Schematic illustration of the fiber adapter assembly for the alignment-free optical coupling and gas filling of the HC-PCF. The assembly mainly consists of ferrules, tubing sleeves for the mounting of the HC-PCF (middle), and the HPLC tubing for gas inlet and outlet (bottom and top). The laser is coupled through an optical window of BK7 material into the HC-PCF, and the Raman signal is collected in the backscattering geometry [82].

The adapter consists of the body including the fiber fixation, gas entrance, exit port, the sealing, a thin glass plate acting as an optical window, and a cover part with screws. Special ferrules fix the fiber within the adapter with a minimum distance between fiber end facet and optical window. The special high-pressure tubing further provides the filling and flushing of the fiber and dead volume within the fiber adapter up to absolute pressures of 20 bar. The adapter ensures the unperturbed alignment of the fiber for the gas detection. The adapter was improved for low working distance microscope objective lenses down to 3 mm for one fiber end and a permanent monitoring of the transmitted laser light with the powermeter for the other (cf. Fig. 4.1). The unfocused laser beam passing the thin optical window will only generate a negligible silica Raman signal.

The minimized dead volume within each fiber adapter is less than 100 nL. The two-way gas flow for each adapter assembly enabled fast flushing of the dead volume before fiber fillings within seconds for moderate gas pressures.
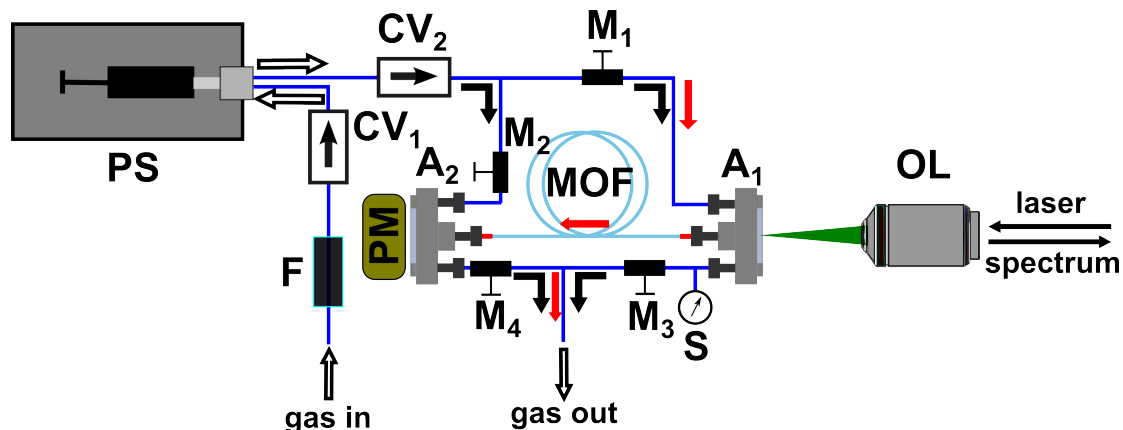

Figure 4.3: Scheme of the setup for fast and precise filling of the microstructured optical fiber (MOF) with different gas mixtures consisting of a mid pressure pump system (PS), fiber adapter assemblies (A_1 and A_2, see Fig. 4.1), check valves (CV), magnetic valves (M), powermeter (PM), microstructured optical fiber (MOF), microscope objective lens (OL), sensor for pressure and temperature (S), and sinter filter (F). Both tubing, connected to input and output of both fiber adapter assemblies, were flushed and filled with all magnetic valves being opened (black arrows). Closing the magnetic valves M_2 and M_3 realized the flushing and filling of the MOF with a gas mixture (red arrows). It could be switched between modes via these software-controlled magnetic valves (M). The Raman analysis was non-consumptive and did not change the gas composition.

The arrangement for flushing and filling the fiber is schematically presented in Fig. 4.3. The rapid filling of the optical fiber gas sensors with multi-gas compositions was essential for fast FERS monitoring with changing gas concentrations. The neMESYS mid pressure pump system (PS, cetoni GmbH) consisted of a metal gas syringe with 50 ml volume (cetoni GmbH) and provided a pressure load of about 20 bar. Thereby, the dead volume of the fiber adapter assemblies and all tubing next to a fiber filling could be flushed within seconds (Fig. 4.3).

The general filling procedure included first, the gas composition passing a sinter filter (F) with a pore size of 0.5 µm. Then it was filled into the syringe of the pressure pump system, and afterwards the dead volume of the setup was flushed by the gas loaded syringe. All magnetic valves (M_1 - M_4) were opened, such that the gas flow could follow the direction, which is illustrated by the black arrows in Fig. 4.3. Afterwards, the magnetic valves M_2 and M_3 were closed and the gas composition passed exclusively through the HC-PCF, presented by the red arrows in Fig. 4.3. Finally, all magnetic valves (M_1 - M_4) were closed to maintain a stable overpressure along the fiber for quantitative FERS measurements. The whole measurement procedure was fully automatized by a LabVIEW routine (National Instruments). It reads and controls all 4 magnetic valves, the pressure pump system, the powermeter, and the spectrometer.

Applying the software-controlled routine for the setup measurement process, a rapid measurement with the steps of fast gas filling, Raman gas analysis, and new gas filling could be achieved within some tens of seconds. No further optical readjustment of the backscattered arrangement (Fig. 4.1) was necessary. The individual measurement time is dependent on the application and the concentration of the gaseous analyte.

4.1.5 Filters

Additional Rayleigh scattering and laser light reflection from the fiber end facet and optical components are collected by the microscope objective lens. This light has the same wavelength as the laser beam. This Rayleigh light is around 3 orders of magnitude stronger than the Raman signal [77]. It will be blocked by a dichroic mirror for 532 nm laser wavelength (Semrock RazorEdge Dichroic, model "LPD01-532RU-25") by more than 6 orders of magnitude. The function of the dichroic mirror in a 45 °-arrangement is the reflection of laser light to the fiber and the transmission of backscattered Raman signal from the fiber within the setup.

An additional long-pass edge filter was installed after the dichroic filter in order to suppress the Rayleigh signal. Different filters are used for the different excitation wavelengths at 532 nm (Semrock RazorEdge filter, model "LP03-532RU-25"), at 607 nm (customized long-pass edge filter), and at 660 nm (Semrock ultrasteep long-pass edge filter, model "LP02-664RU-25"). Their individual transmittance curves are shown in Appendix A.1. The transition width is of crucial importance since pure rotational lines of molecular hydrogen can be found at low wavenumber regions starting at 354.3 cm^{-1}, which refers to the vibrational Raman band $S_0(0)$ of molecular hydrogen [55]. Most of the commercially available edge filters show transition widths of 100, 150, or 300 cm^{-1}, which is important in later experiments. It has to be mentioned, that the long-pass transmission of these edge filters are not uniform with regard to the wavelength. Strong pronounced ripples around the order of percent transmittance modulation are visible in the transmission wavelength range (cf. Fig. A.1). This structure can experimentally interfere with a possible spectral fine structure. A calibration procedure, which will be later introduced, includes these optical component characteristics.

4.1.6 Light collection optics

The light collection optics for the backscattered Raman signal consists of the objective lens, which couples the laser beam into the fiber, and the focus lens in front of the entrance slit of the spectrometer. This achromatic doublet lens with focal length of 75 mm (Thorlabs, model "AC254-075-A") creates a focal length shift of $\Delta d_f = 400\,\mu$m for a wavelength range from $530 - 630$ nm. The chromatic aberration originating from the lens optics is negligible due its relatively large focal length. The low loss transmission is guaranteed by an AR-coating. Together with the focal length of 9 mm for the utilized microscope objective lens, the backscattered Raman signal emerging from the hollow core is magnified to 50 µm in diameter at the spectrometer slit plane. The acceptance *NA* of the spectrometer is important for signal collection and should be matched with the Raman signal collecting optics (cf. 4.1.7).

4.1.7 Spectrometer

The collected backscattered Raman light from the HC-PCF is focused by an achromatic doublet with $f = 75$ mm (Thorlabs Inc.) onto the spectrometer slit. The spectrometer (Acton 2550i, Princeton Instruments) with focal length of 500 mm is equipped with a width-adjustable slit, different gratings, and a CCD detector [93]. Three different dispersive gratings with 600, 1800, and 2400 lines/mm can be chosen within the spectrometer. The fixed aperture ratio is $f/\# = f/6.5$ [93]. The corresponding acceptance *NA* for the spectrometer can be calculated to ~ 0.077. The magnification of 7.5 for the fiber radiated Raman signal with diameter 6 µm to 45 µm at the spectrometer slit plane was realized by the microscope objective lens and the achromatic doublet. The original *NA* of the radiated Raman signal approximately equal to the fiber *NA* with 0.2 is decreased to 0.027 by the used achromatic doublet. This value is much smaller than the acceptance *NA* of the spectrometer. Even for a certain lens misalignment, the Raman signal will be

fully collected. In other words, a minimum focal length of 26 mm for the doublet lens will be accepted losslessly by the spectrometer, but usually results in a higher chromatic aberration. An achromatic lens in combination with a large focal length, on the other hand, will guarantee negligible chromatic aberrations for the spectrally broad Raman light. The silica Raman signal originating from the microstructured fiber cladding with a *NA* higher than 0.2 will be collected. The spatial pinhole (P) in Fig. 4.1 nevertheless cuts out this parasitic Raman signal.

Another aspect is the spectral resolution of the spectrometer, which will be critical for different measurement scenarios. The detection of a multi-gas composition will involve wavenumber regions up to 3000 (4200) cm^{-1} including Raman vibrational bands of molecular methane (hydrogen) [166]. Thus, a low dispersive grating is preferred for a single measurement regarding fast acquisitions for real-time applications. On the other hand, labeling experiments (e.g. $^{12}CO_2/^{13}CO_2$) demand a higher spectral resolution for line separation, which provides a high precision for the quantification of gas concentrations and their alterations [82].

Spectral resolution The spectral resolution of a spectrometer is mainly governed by 3 parameters: (1) the focal length of the spectrometer, (2) the number of lines per mm of the grating, and (3) the spectrometer slit width. The focal length is somehow fixed. Larger focal lengths will increase the spectral resolution but decrease the capability of light collection defined by the $f-$number. Here, the spectrometer slit width could be manually set from 5 µm to 3 mm.

Gratings with a higher number of grooves per millimeter will dramatically increase the spectral resolution. Nevertheless, the blazing angle for standard gratings is optimized to lower wavelengths for an increasing groove density. The 2400 lines/mm grating features its highest reflection efficiency in the low UV region. The introduced experiments are generally accomplished with the help of the 600 lines/mm grating. The resolution was further adjusted by the slit width and scales in wavenumbers inversely linear with the slit width for large enough slit widths. Because the image of fiber core spans to 50 µm in diameter on the slit plane, a general width of $60 - 100$ µm was used throughout the experiments. The highest possible resolution of ~ 0.8 cm^{-1} will be achieved with the 2400 lines/mm grating and the smallest slit width of 5 µm [82].

4.1.8 CCD array

A back-illuminated deep depletion CCD with 1024×1024 pixels and an individual pixel size of 13 µm $\times$ 13 µm was used. The slit, with a height of 13 mm, was imaged on this LN$_2$-cooled CCD array with a magnification of 1 by a Czerny-Turner monochromator. Contrary to thermo-electrical cooling via a Peltier-element, which allows to cool down the CCD detector to a temperature of -80 °C without additional water-cooling, the LN$_2$ technique allows cooling down to temperatures of -130 °C. This will dramatically decrease the dark noise. The back-illumination technique provides a high quantum efficiency of 95 % in the wavelength range of interest, i.e. VIS range. The deep depletion feature, i.e. a high resistivity epitaxial silicon substrate CCD, expands the high efficiency range of > 90 % in the VIS region to 900 nm. The etaloning effect of a back-illuminated CCD occurring at the IR range, which results in spectral fringes, is slightly suppressed by the eXcelon^{TM} technology (by Princeton Instruments) [94].

Various noise sources were state in a previous Sec. 2.4. The dark current noise was generally minimized by appropriate cooling of the detector chip. The read-out noise, resulting from the AD conversion during read-out of each CCD pixel, can be significantly reduced by applying the software-based binning operation. In general, the pixels can be binned vertically and/or horizontally. The horizontal binning may reduce the spectral

resolution due to summing neighboring pixels horizontally. In the case of Raman spectroscopic detection of vibrational and rotational Raman gas bands featuring very sharp bandwidths, there will be no significant benefit for horizontal binning. Vertical on-chip binning provides a collective read-out of vertical pixel blocks, i.e. bins.

The read-out of a spectrum from the eXcelon^{TM} 1024BR CCD chip without vertical on-chip binning lasts about $(1024 \cdot 1024)/100\,\text{kHz} = 10.5\,\text{s}$ [94]. A spectrum with only 5 vertical pixel lines will reduce the read-out to a total of 0.1 s. The primary benefits of (vertical) binning are an improved SNR and higher frame rates. Binning provides an increase in SNR due to reduced read noise contributions. Normally CCD read-out noise is added during each read-out step, thus read-out noise will be added to each pixel during normal operation. In binning mode, the read-out noise adds to each superpixel, which has the summed signal contribution from multiple pixels. For the ideal case, the SNR improvement is equal to the binning factor. This experimental SNR dependency on vertical binning is shown in Fig. 4.4. Between the two extrema, one horizontal pixel line and full binning of all 1024 vertical pixel lines, the SNR varies by nearly one order of magnitude. The general electronic read-out noise limits the maximum SNR.
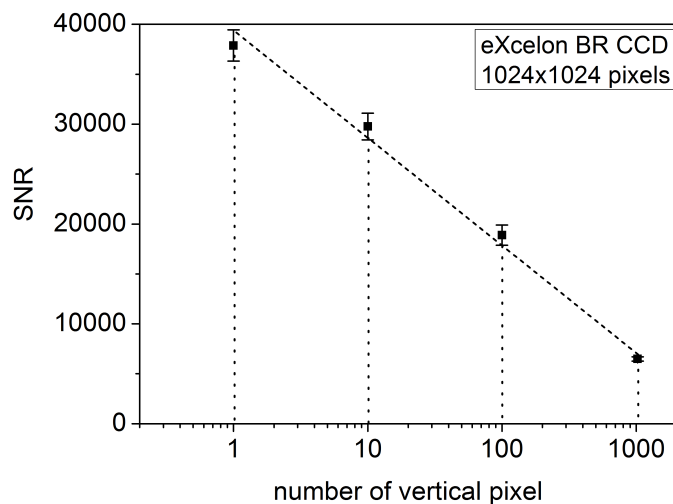

Figure 4.4: The SNR dependence for a complete on-chip binning (1 pixel line) to no on-chip binning (1024 pixel lines) is shown for the presented CCD detector. The SNR was determined by analyzing the characteristic phonon band shift of monocrystalline silicon at 521 cm^{-1} (cf. Fig. 5.3a) for 4 different numbers of read-out pixel lines. The latter could be selected within the spectrometer software.

The spectrometer-implemented 16-bit analog-to-digital-converter (ADC) limits the maximal read-out counts, i.e. the dynamic range of the measurement. Depending on the internal software gain, the number of counts for an individual pixel is $100\,000\ \text{e}^-/1.5\,\text{e}^- = 65\,536$ ($100\,000\ \text{e}^-/6\,\text{e}^- = 16\,667$) with internal spectrometer gain 3 (gain 1) for 100 kHz read-out frequency. For general binning, the following maximal values independent of the number of vertical pixel lines with $250\,000\ \text{e}^-/1.5\,\text{e}^- = 166\,667$ ($100\,000\ \text{e}^-/6\,\text{e}^- = 41\,000$) for gain 3 (gain 1) are realistic [94]. This implies that the number of vertical pixels cannot be increased arbitrarily without reaching the detector saturation. Contrarily, decreasing the number of vertical pixel lines can increase the spectrometer's SNR and thus the precision at the same acquisition time or it allows for shorter acquisition times at the same precision level (cf. Fig. 4.4).

Furthermore, applying full chip binning throughout the experiment would introduce a spectral curvature over the detector chip height, which is caused by the spectrograph's astigmatism. An unnaturally distorted and asymmetric Raman line broadening and shift would be the consequence. Due to the image properties originating from the Raman signal collection of the fixed fiber core diameter, vertical binning of $3 - 10$ segments, i.e.

$39 - 130\,\mu m$, has been utilized in most of the Raman measurements during this work. Thus, the intrinsic spectrometer astigmatism for less than 10 vertical pixel lines was never present.

4.1.9 Mass flow controller assisted experiments

The highly accurate quantification of a mixture with different gas concentrations is realized with the help of mass flow controllers (MFC). The metal-sealed thermal MFC (model "GF40", Brooks Instruments) could be operated in 3 different flow rate regimes: $3 - 10$ standard cubic meter per minute (sccm), $93 - 281$ sccm, and $861 - 2600$ sccm. For the reference conversion factor of 1.0 for nitrogen within the calibrated range from $1 - 10\,$bar differential pressure with a general flow control range of $2 - 100\,\%$ is provided [92].

With the help of total of 4 MFC with different flow rates, pure gases could be reduced in concentration to some tens of ppm by mixing with the Raman-inactive noble gas argon on the one hand before entering the HC-PCF. On the other hand, different low concentrated multi-gas mixtures with $< 1\,$vol. % were reduced to some ppm - sub-ppm in concentration. The flow accuracy of each MFC is specified to $1\,\%$ of the defined gas flow in the flow control range of $35 - 100\,\%$, and $0.35\,\%$ of the full scale for a flow range from $2 - 35\,\%$ relatively[1] [92]. However, an out-of-specification utilization of these MFC would result in a relatively large error in trace gas concentration[2].

Mixing of a multi-gas mixture with defined concentrations and the filling by the mid pressure pump (Sec. 4.1.4) is operated with a LabVIEW-based software. Flow rates and mixing ratio for the MFC mixing system could be controlled and automatically monitored. Furthermore, a homogenous mixing of trace and carrier gases before the fiber filling was ensured by a sinter filter ("FE73A-05S", Dk-Lok GmbH). The specified pore size of 0.5 µm resulted in the necessary turbulent flow regime. The highly precise mixing of differently concentrated multi-compound mixtures including molecular hydrogen was essential for the simulated breath gas detection, which will be introduced in Chap. 6.

4.2 Data acquisition and processing

4.2.1 Cosmic ray removal

Before any quantitative measurement can be carried out from a Raman spectrum, several preprocessing steps are essential. This involves the correction of the Rayleigh wavenumber to $0\,\mathrm{cm}^{-1}$, the number and position of pixel lines, the wavenumber calibration, and the correction for cosmic rays. Another important step for the accurate Raman quantification is the baseline correction. After all these steps, the accurate extraction of the Raman signal is possible. The schematic flow chart for this data processing is given in Fig. 4.5.

For long-acquisition time spectra, usually for very low concentrated gas compounds, several cosmic ray events were frequently encountered. The read-out of a few vertical pixel lines (< 10) could tremendously decrease cosmic ray signal contributions in the region of interest (ROI). In literature, two types of correction technique exist. Either spatial spectral information [202, 98] or temporal spectral information [24, 141, 87, 49] is used. Spatial correction incorporates a single scan and requires only one spectrum. This is highly recommendable for rapid acquisition applications.

---

[1]e.g. $0.0035 \cdot 281\,\mathrm{sccm} \cong 1.0\,\mathrm{sccm}$ for a flow up to 98 sccm realized by a MFC with a flow range of $93 - 281$ sccm

[2]The MFC with flow range of $93 - 281$ sccm would provide a relative error of 5 % at an adjusted out-of-range flow rate of 20 sccm, which consequently results in a concentration error of 5 %.
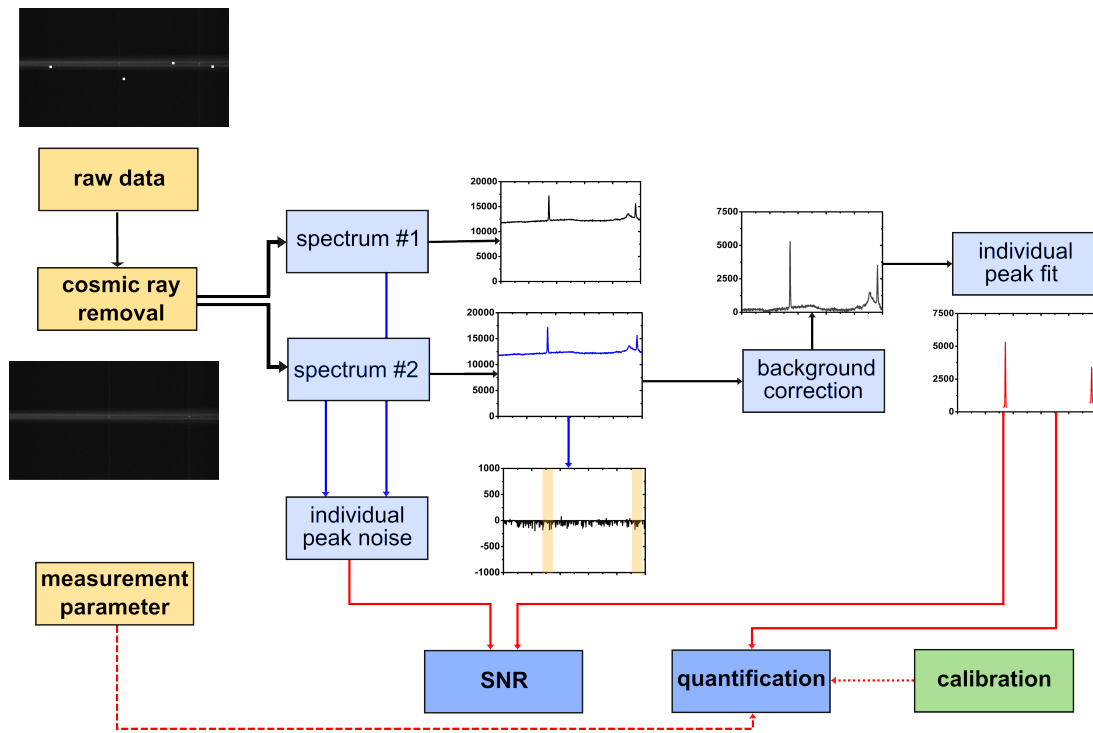
Figure 4.5: Scheme for the applied processing chain, which indicates the action of each individual step. Details are found in the text.

One single scan technique for spatial correction is the Differential Cosmic Ray Removal (DCRR), which requires a two-dimensional spectral input [44]. This technique is very efficient if a significant pixel binning is applied in the acquisition. Contrary, for long acquisition times, i.e. several tens of seconds, the method of Temporal Cosmic Ray Removal (TCRR) with the principle of spectral difference comparison can be used [44]. Hence, at least two subsequent spectrum recordings are determined and pixel-wise compared. If the spectra differ less than a predefined value, the data points are averaged and resulting in a new output value. Otherwise the smaller value without cosmic ray fraction is taken. The predefined threshold has to be set appropriately, i.e. large enough such that the noise fluctuations are included and small enough for detection of most of the cosmic ray events. TCRR turned out to be fast enough, robust, easy to implement, and very efficient in removal of cosmic rays. For experiments with long acquisition times, usually related to measurement of low concentrated gaseous analytes, TCRR was implemented; otherwise DCRR was used.

4.2.2 Peak intensity analysis

Two different types of peak intensity determination have been considered. An easy-to-apply method is based on summing individual intensity contributions from all pixels for each individual peak within the spectral profile. This method provides very accurate intensity values especially for highly resolved spectra, where different line features do not overlap. Another method is the convolution of individual peak lines. This includes fitting of a combination of Gauss and Lorentz profiles to the peak, i.e. a Voigt profile [3]. In general, the pure or pseudo-Voigt profile is influenced by other spectroscopic or optical "functions" like optical components, fibers, filter optics, the spectrometer grating, and the pixel structure of the CCD detector.

Four parameters, i.e. position, intensity, FWHM of the peak, and Gauss-Lorentz relation, will fully describe the Voigt profile. First, an isolated peak with adequate peak intensity without overlap from other peaks was chosen from a measured spectrum and

stored pixel-wise in a calibration set. Otherwise, the peak was extract from a calibration spectrum without convolution. The line shape function was fitted to the peak and a sub-pixel translation is acquired by numerical peak shape interpolation. Different peak shapes caused by different thermally excited states or line broadening effects, such as Doppler broadening, pressure broadening, etc. [43], resulted in individual fitting functions. Afterwards, a baseline correction was performed as individual offset. Spectral wavenumber drifts due to thermal drift of the fiber coupling or variations for the optical parts have been compensated by the sub-pixel approximation.

The calibration is integrated in the customized LabVIEW acquisition software. The Raman signal intensity is divided by the absolute gas pressure inside the fiber, inverse absolute temperature, laser input power, fiber model, and a special function for fiber length and fiber coupling to a steady monitored fiber transmission. The Raman background was subtracted by a predefined spectrum from Raman inactive gases like the easily available noble gas argon including the parasitic silica Raman background, which will be generated by the microstructured optical fiber. A two-point calibration should be performed for accurate quantification of any gas compound within a gas mixture or single gas. This was either performed by measuring a pure gas or a higher concentrated gas mixture with known concentration. The unknown concentrations c_j are then correlated to the measured peak intensities I^A by

$$I_i^A(\tilde{\nu})\Big|_{i=1...k} = \sum_{j=1}^{m} I_{ij}^C(\tilde{\nu}) \cdot c_j \,, \tag{4.4}$$

with the calibration gas C, the analysis gas A, the intensity I, i the number of CCD pixel, and m the number of gases. Best results for the calibration matrix $I^C(\tilde{\nu})$ were carried out with 3 differently concentrated gas measurements: the zero concentration or noble gas detection, pure gas, and one concentration between 0 % and 100 % for the diluted gas component.

4.3 Analysis of the setup performance and multi-gas quantification

4.3.1 Raman signal scaling and linearity

The design of a fiber gas sensor for quantitative multi-component gas detection is based on an accurate calibration. The length of the fiber plays an important role for signal scaling and was already discussed qualitatively before. Although the Raman signal scales linearly with the effective volume length (cf. Eq. 2.13), the bandgap characteristics will create an exponential dependency on the fiber length.

First of all, the Raman signal should scale linearly with the intensity of the exciting field for fixed measurement parameters. State-of-the-art cw-DPSS lasers provide laser output powers of more than 10 W, are compact, and have an excellent beam quality. Very compact and miniaturized lasers for Raman spectroscopy exhibit output powers of some 100 mW. The application of high power lasers in the W-regime compared to the mW-range introduces a Raman signal scaling improvement of at least 2 orders of magnitude in the laboratory. This can result either in a theoretically 100 times smaller acquisition time or a 100 times higher sensitivity with some limitations, which are discussed later.
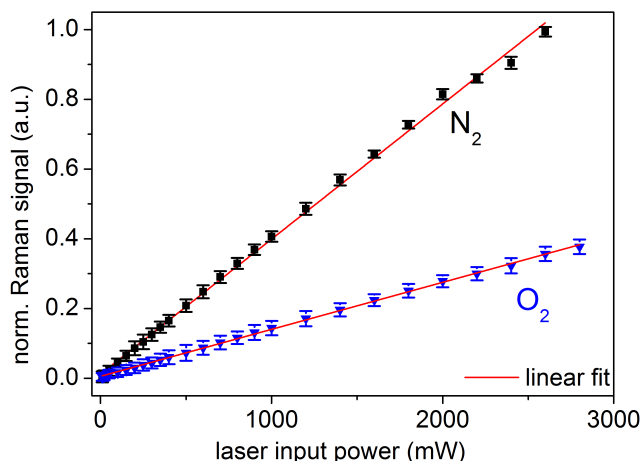
Figure 4.6: Illustration of linearity and scalability for the fiber-enhanced Raman signals of N_2 ($\sim$ 78 vol. %) and O_2 ($\sim$ 21 vol. %) in ambient air for increasing laser powers (at $p = 1$ bar, $T = 21$ °C, with a fiber length of 0.4 m HC-PCF "HC-580-02" (NKT Photonics) for 1 s exposure time, and application of the 600 lines/mm grating). Peak areas at 1556 cm^{-1} for O_2 (blue) and 2331 cm^{-1} for N_2 (black) were integrated and fitted (red) respectively. For better illustration, the individual Raman signals for O_2 and N_2 were normalized to that of the N_2 Raman peak at 2.8 W laser output power.

It was experimentally found, that the Raman signal of the individual gaseous analytes inside the hollow fiber core scales linearly with the laser input power and for each gas compound. This is exemplarily shown in Fig. 4.6 for the integrated Raman peak of the simultaneously measured gas components nitrogen and oxygen naturally occurring in ambient air. The output power of the 532 nm "Opus" laser varied from $10 - 2800$ mW [124]. Each Raman spectrum was repetitively measured for 5 times. The signal reproducibility, which is mainly determined by the fiber coupling, is illustrated as error bar for each measurement. The pointing stability for the laser coupling is a result of spatial drifts originating from temperature changes and air fluctuations in the laboratory. The temperature drift mainly affects optical components and thus leads to spatial drifts for the laser coupling procedure.

A linear scaling of Raman signal is as well realized over the gas pressure (cf. Eq. 2.13). The HC-PCF represents a closed system filled with gaseous analyte at a constant temperature and constant particle density, i.e. the molecule number of gas per unit volume, during the acquisition process. Thus applying the ideal gas law, the Raman signal intensity will scale linearly with increasing pressure for the analyte inside the fiber core. The utilized fiber adapter assembly has a seal tightness for up to 20 bar, resulting in a 20$\times$ higher density of gas molecules for the same fiber volume in the range of nL/cm. The resulting linear scaling is shown in Fig. 4.7 up to an absolute pressure of 9 bar. This dramatically increases the sensitivity for shorter acquisitions.

Conclusively, higher sensitivities (or lower acquisition times) can be mainly achieved by controlled adjustment of the laser power and gas pressure inside the bandgap fiber. An excellent linearity between Raman intensity and laser intensity as well as pressure was shown. This can provide a substantial increase in sensitivity by $\sim$ 2 orders of magnitude.
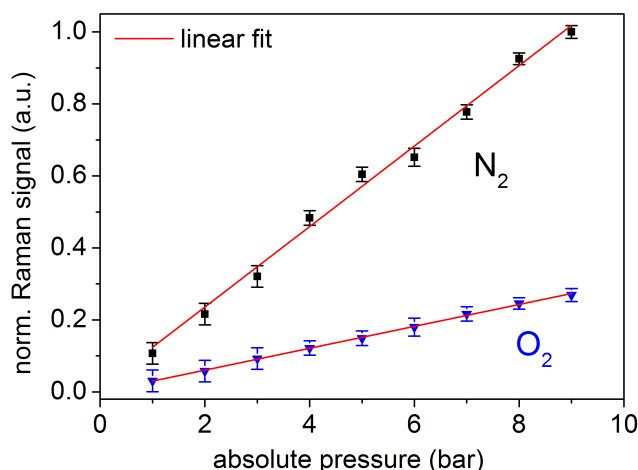
Figure 4.7: Illustration of linearity and scalability for the fiber-enhanced Raman signals of N_2 (~ 78 vol. %) and O_2 (~ 21 vol. %) in ambient air for increasing absolute pressure up to 9 bar inside the HC-PCF (at $T = 21\,°C$, 100 mW laser power at 532 nm excitation wavelength, with fiber length of 0.4 m HC-PCF "HC-580-02" (NKT Photonics), 1s exposure time, and application of the 600 lines/mm grating). Peak areas at 1556 cm^{-1} for O_2 (blue) and 2331 cm^{-1} for N_2 (black) were integrated and fitted (red), respectively. For better illustration, the individual Raman signals for O_2 and N_2 were normalized to that of the N_2 Raman peak at 9 bar absolute pressure.

4.3.2 Dynamic range, signal-to-noise ratio, and limit of detection
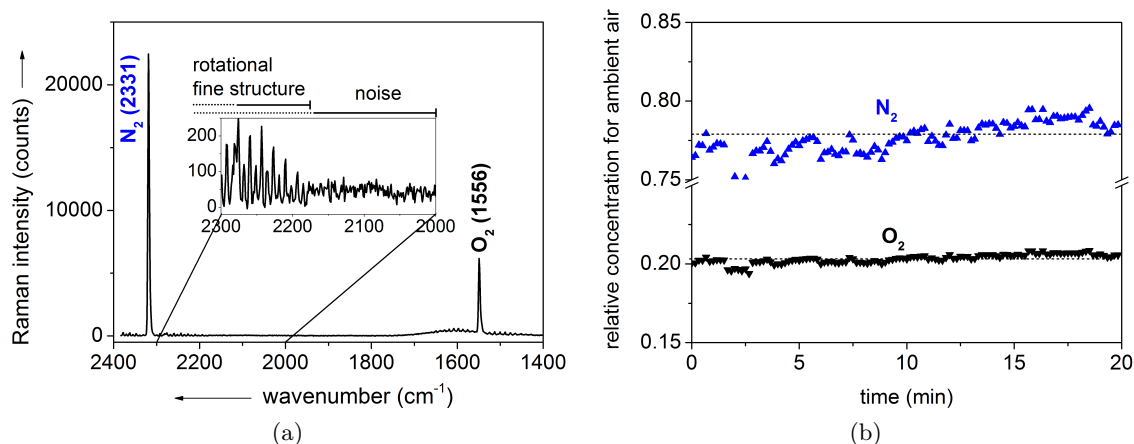

Figure 4.8: Performance test of FERS by monitoring of ambient N_2 and O_2. A measurement series with an individual acquisition time of 1 s, which has been repeated each 10 s for a total time period of ~ 20 min, was performed (with the 532 nm laser at 0.2 W output power in combination with a 0.7 m HC-PCF "HC-580-02" (NKT Photonics) and the 600 lines/mm grating). (a) A single Raman spectrum with the Q-branches of N_2 and O_2 for ambient conditions is presented. The inset shows the background noise next to the rotational fine structure of the N_2 Q-branch at 2331 cm^{-1} more detailed. (b) The time trend of relative intensities of these 2 major components in ambient air: Each data point represents a single measurement as shown for N_2 (blue) and O_2 (black).

Reproducibility of the Raman signal is a crucial requirement for quantitative measurements of a multi-gas composition. If the Raman signal scales linearly for the analyte concentration over the whole dynamic range, simple and fast calibration of the gas sensor can be utilized and a two-point calibration for the concentration will be sufficient. A stable signal noise background also leads to a spectrally unaffected Raman signal after

background correction as described previously. The exact LOD depends on the gas sensor characteristics, i.e. mainly on the fiber attenuation characteristics, and the actual differential Raman scattering cross sections of each gas component. Consequently, an almost $\sim 10\times$ higher relative Raman scattering cross section of CH_4 compared to that of N_2 results usually in a $10\times$ lower LOD for former compared to last (Tab. 2.2). The actual performance of the FERS setup in relation to the SNR, the LOD, and the precision within the dynamic range is presented. Fig. 4.8 and Fig. 4.9 exemplarily reveal the performance for ambient air.

Signal-to-noise ratio Fig. 4.8 shows a Raman spectrum of ambient air at ambient conditions after all data processing steps. For convenience, the height of the *Q*-branch for N_2 and O_2 is taken as the signal intensity I_{tot}. The signal peak noise is extracted from the difference spectrum of two sequential measurements (cf. Sec. 2.4). The peak noise σ_{peak} was determined to 13 (16) counts for N_2 (O_2). The SNR ratio is simply defined as I_{tot}/σ_{peak}. The concluding O_2 and N_2 concentrations and their precisions are tabulated in Tab. 4.3. The SNR for the measurement of ambient air resulted in ~ 7000 (~ 2000) for N_2 (O_2). It should be mentioned that an improvement in SNR are mainly related to the hardware characteristics and the way of acquiring the data. The accurate fitting process and the correct setting of the acquisition time will determine the SNR and the precision for time series acquisition.

gas component	time series			single spectrum
	c_{gas}	σ_{stat}	σ_{stat}/c_{gas}	SNR
	(%)		(%)	
N_2	77.90	1.49	1.91	6718
O_2	20.42	0.43	2.11	1728

Table 4.3: Averaged concentration c_{gas}, standard deviation σ_{stat}, and concluding precision σ_{stat}/c_{gas} are stated for N_2 and O_2 referring to the time series of ambient air in Fig. 4.8: The SNR was determined by the integrated Raman peak signal and peak noise. A single Raman spectrum was taken every 10 seconds with laser power of 200 mW (at 532 nm) in a 0.7 m long "HC-580-02" PBG fiber at an acquisition time of 1 s with $p = 1$ bar and $T = 21\,°C$.

Precision In Fig. 4.8b the relative intensities of the two main components N_2 and O_2 in ambient air are plotted for a time interval of ~ 20 min. The small fluctuations of amplitudes indicate the stability. Results for the statistical analysis of relative intensities and standard deviation are presented in Tab. 4.3. The standard deviation σ_{stat} is below 1.5 % and the precision σ_{stat}/c_{gas} is better than 2 %, which is related to the repeatability of a single measurement and should be taken into account for the requirements of the individual application (Fig. 4.8b). This measurement precision is related to statistics and therefore can be easily determined from a time series.

Limit of detection According to Sec. 2.4 the minimum detectable spectral feature should be higher than $3\times$ the noise σ_{peak}. In other words, the LOD is defined as $3 \cdot \sigma_{peak}/SNR$. The LOD is theoretically related to the minimum detectable amount of the analyte. In literature, the noise often equals the signal standard deviation at a flat region, which is located next to the Raman peak intensity in the spectrum. Nevertheless, this assumption does not take the additional peak noise into account. Furthermore, in the case of a high concentrated gas compound and/or a broad silica Raman background (cf. Sec. 3.5.2), individual bands and a fluorescence characteristics add to the peak noise. Consequently, the estimated LOD for a given SNR will be higher than taking a

flat region for the noise contribution. Thus for the SNR in Tab. 4.3, two subsequent Raman spectra of ambient air were subtracted and the peak noise as standard deviation around the vibrational Raman line was examined, respectively.

To show the performance over a wide dynamic concentration range accompanied by an extremely high linearity sufficient for a two-point sensor calibration, a concentration series measurement for molecular hydrogen in carrier gas nitrogen is presented in Fig. 4.9. This calibration plot ranges from 10 ppm to 5 vol. % or 50 000 ppm by volume hydrogen concentration in carrier gas nitrogen. The HC-PCF "HC-633-02" [146] (NKT Photonics) with length of 0.5 m in combination with the frequency-doubled Nd:YAG laser at 660 nm excitation wavelength and 0.8 W output power were used throughout the calibration plot measurement. The investigated hydrogen rotational peak $S_0(1)$ was integrated from 583.4 – 589.0 cm^{-1} (cf. 5.4). Each measurement error (SD) was determined by a sequential measurement series with $N = 5$ (Fig. 4.9).

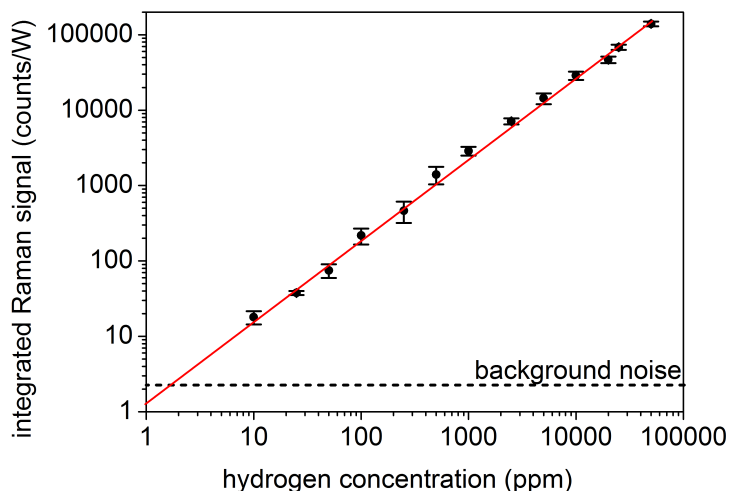Figure 4.9: Linear dependency of the integrated Raman signal for H_2 in carrier gas N_2 for different hydrogen concentrations: The investigated rotational hydrogen Raman peak $S_0(1)$ was integrated from 583.4 – 589.0 cm^{-1}. The background noise level at 2.8 counts/W for 10 ppm hydrogen is marked with a dashed line. It was assumed that this background noise, which was extracted from the measurement with lowest hydrogen concentration at 10 ppm, will not change significantly for hydrogen concentrations < 10 ppm.

These hydrogen Raman signal variations mainly arose as a consequence of thermally-induced variations of the laser light coupling into the HC-PCF. Because the Raman signal scales linearly with the molecule concentration, the linear fit with low error bars demonstrates an excellent linearity in Fig. 4.9. Although the maximum hydrogen concentration was fixed to 5 vol. %, extending the sensor range to 100 vol. % would practically constitute no difficulty for any detectable gas compounds. Overall, a minimum signal background noise of 2.8 counts/W for 0 ppm hydrogen in nitrogen was measured. By measuring the concentration of 10 ppm and 25 ppm, the integration of the rotational hydrogen Raman peak resulted in a value of 17.9 counts/W and 37.6 counts/W. This leads to a noise equivalent LOD of around 4.7 ppm for SNR = 3 (cf. Sec. 2.4) by volume H_2 in accordance to DIN 32456[3]. The detection of low concentrated molecular hydrogen for human breath analysis is shown in Chap. 6. Hence, even lower hydrogen concentrations around 5 ppm were detected by an improved FERS setup leading to a noise-equivalent LOD of < 1 ppm in accordance to DIN 32456.

---

[3]Applying the LOD determination for a hydrogen concentration of 1000 ppm (not in accordance with DIN 32456), the SNR would erroneously lead to $c_{LOD} = LOD_{1000} \cdot c_{1000} = (3 \cdot 2.8/2876) \cdot 1000\,\text{ppm} = 2.9\,\text{ppm}$.

4.4 First quantitative FERS measurements

In the first part of this chapter, the fiber-based Raman gas sensor for potential multi-component gas quantification was introduced in detail. The ability for rapid detection of gaseous analytes in a concentration range from 10 ppm to 100 vol. % makes FERS applicable in the field of greenhouse-gas relevant interrogations and clinical diagnosis by human breath analysis. First quantitative multi-component gas measurements will be presented in the following part.

4.4.1 Biogenic multi-gas composition

Tracing of climate-relevant atmospheric gases like CH_4, CO_2, N_2O, N_2, or O_2 is important in the field of environmental gas sensing and for real-time gas composition monitoring. CH_4, next to CO_2, is an important climate relevant gas with a 21 times higher global warming potential than CO_2 [60]. Forest soils showed to be significant sinks for CH_4, but also sources for NO, CO_2, and N_2O, whereas wetlands represent major sources for CH_4 [96]. The production of N_2O contributes to the catalytic stratospheric ozone destruction and atmospheric N_2O increases through microbial denitrification by heterotrophic bacteria, e.g. *Pseudomonas*, and through autotrophic denitrifiers [157]. The monitoring of gas composition exchanges is of significant importance for the understanding of dynamic soil-microbe-plant interactions within the climate-sensitive ecosystem.
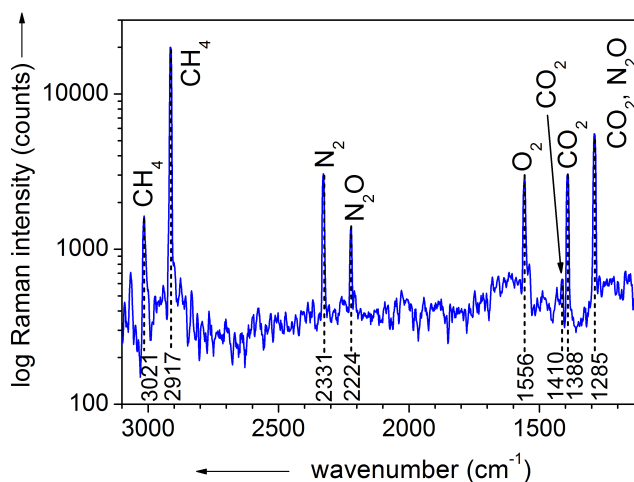

Figure 4.10: The FERS measurement of a biogenic multi-gas composition, consisting of climate relevant gases CO_2, CH_4, and N_2O together with N_2 and O_2 (each ~ 1 vol. % in Raman inactive Ar carrier gas), is presented. The Raman spectrum was acquired with one single measurement within 70 ms acquisition time for a laser power of 1.5 W at 532 nm excitation wavelength, the utilized 600 lines/mm grating, and an absolute gas pressure of 10 bar within the 0.7 m long HC-PCF "HC-580-02".

A mixture of these 5 important biogenic gases was analyzed in order to show the analytical performance of the presented FERS setup. The high reliability and specificity for the Raman method is demonstrated in Fig. 4.10. The vibrational modes of all five gases covered a spectral range of up to 3100 cm^{-1}. The spectrum was achieved by using the 532 nm laser with 1.5 W output power, 10 bar absolute gas pressure along the HC-PCF "HC-580-02" with length of 0.7 m, the 600 lines/mm grating, and a total acquisition time of 70 ms. Previous two-point-calibrations with pure gases of Ar, N_2, O_2, etc. led to the quantified values presented in Tab. 4.4.

gas component	measured conc. (%)	certified conc. (%)	absolute deviation (%)	SNR
N_2	1.15	1.12	0.03	266
O_2	1.01	0.915	0.095	182
CO_2^*	1.10	1.02	0.08	193
N_2O	0.870	0.985	0.115	123
CH_4	1.00	1.08	-0.08	1940

Table 4.4: Quantitative FERS analysis of a biogenic gas composition (N_2, O_2, CO_2^*, N_2O, and CH_4): Each individual peak was analyzed for the Raman measured concentration in comparison with the certified values from Linde AG prepared in compliance with DIN EN ISO 6141. The absolute deviation and the SNR are listed. *: The highest band of molecular CO_2 at 1388 cm^{-1} was integrated.

This example demonstrated the high accuracy and specificity of FERS for the quantification of climate-relevant biogenic gas compositions. The low acquisition time should be emphasized for gas concentrations in the low percent region. The absolute sensitivity in terms of LOD is presented later in Sec. 6.2.2 and cannot be determined from Fig. 4.10 according to DIN 32456.

4.4.2 Exhaled human breath analysis

Human breath analysis possesses a huge potential for the non-invasive monitoring of early-disease states. Exhaled human breath is a composition of different major compounds like N_2, O_2, CO_2, and H_2O in combination with trace compounds in the range of ppm - ppt [25]. The simultaneous quantification of exhaled human breath samples is easy to accomplish with the patient and enables fast diagnosis and continuous bedside observation of intensive care patients. Nevertheless, the accurate quantification of the human exhaled breath consisting of many gases in different concentration ranges simultaneously is one major challenge in the field of clinical diagnostics of metabolic disorders and diseases. Important gaseous markers for the detection of important diseases include CO for mitochondrial oxidative stress, CH_4 and H_2 for colonic fermentation of undigested or unabsorbed oligosaccharides [27, 69, 67, 53], and NH_3, $^{12}CO_2$, and $^{13}CO_2$ for the diagnosis of *Helicobacter pylori* infection by means of isotopic-labeled $^{13}CO_2$, i.e. by the^{13}C urea breath test (UBT) [72, 117].

In order to demonstrate the high specificity in combination with the ability of fast detection, the Raman spectrum of 27 nL exhaled human breath within the hollow core of a 0.7 m long HC-PCF was analyzed and quantified within a measurement time of 1 s (Fig. 4.11). The exhaled human breath was directed into the fiber with the help of a membrane pump. The candidate had to blow into a mouth piece until the tubing and finally the HC-PCF was fully flushed by pushing the exhaled breath into the fiber core with the help of a membrane pump at 2 bar absolute pressure. Raman peaks of the major components $^{14}N_2$ (2331 cm^{-1}), $^{16}O_2$ (1556 cm^{-1}), and $^{12}CO_2$ (1388 cm^{-1} and 1285 cm^{-1}) are observable. The gaseous components $^{14}N^{15}N$ and $^{13}CO_2$ with minor concentrations were detected simultaneously to (6000 ± 1100) ppm and (400 ± 100) ppm together with the major components and thus a concentration range of 4 orders of magnitude was covered (Tab. 4.5).
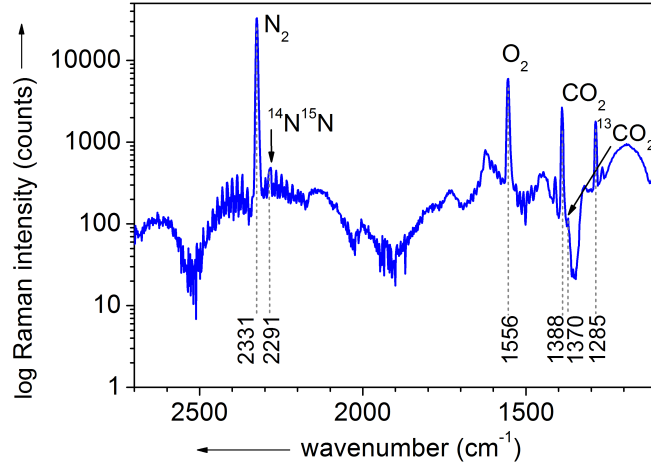
Figure 4.11: Fiber-enhanced Raman spectrum of 27 nL (~ 1.5 nmol) of exhaled human breath, which shows N_2, O_2, and CO_2 as the permanent gases together with the lower concentrated isotopologues $^{14}N^{15}N$ and $^{13}CO_2$ in the ppm range. The spectrum was acquired in 1 s with the help of the 600 lines/mm grating, 3.2 W laser output power at 532 nm excitation wavelength, and a 0.7 m long "HC-580-02" HC-PCF.

gas component	measured conc. (%)	theoretical conc. (%)	rel. scattering cross section
$^{14}N_2$	77.8±0.4	78.1	1.00
$^{16}O_2$	16.0±0.2	16.0-17.0	1.02
$^{12}CO_2$	4.40±0.09	3.0-4.0	1.10*
$^{13}CO_2$	0.04±0.01	0.033-0.044	1.13+
$^{14}N^{15}N$	0.60±0.11	0.58	1.00

Table 4.5: FERS-based detection and quantification of $^{14}N_2$, $^{16}O_2$, $^{12}CO_2$, $^{13}CO_2$, and $^{14}N^{15}N$ within exhaled human breath: Relative Raman scattering cross sections and the detected gas concentrations in comparison to literature values [55]. * and + refer to the strongest Fermi diad band of $^{12}CO_2$ and $^{13}CO_2$ at 1388 cm^{-1} and 1370 cm^{-1}, respectively.

The experimentally derived different gas concentrations within the exhaled human breath sample were in good agreement with the literature values (cf. Tab. 4.5). The shown result emphasizes the generally high dynamic range for FERS and reveals the potential for ^{13}C-labeled marker detection. This has been successfully applied in breath analysis [117, 97], whereas the ^{15}N tracer technique is not yet commonly applied in clinical diagnostics of human breath analysis. Rapid diagnostics of multi-component gas samples is benefited by fast detection in the few seconds scale in combination of small breath sample volumes, provided by hollow core fibers with sample volumes of some tens of nanoliters. This will be presented more thoroughly in the next chapters.

4.4.3 Highly resolved FERS of isotopic-labeled gases

The clinical diagnosis of ^{13}C-labeled CO_2 by terms of human breath analysis requires the specific identification of the ^{13}C-label in the low ppm concentration region on a generally high natural $^{12}CO_2$ background in exhaled breath next to the other natural isotopes [109, 190, 167]. In order to demonstrate the unique capabilities of FERS for selective and quantitative isotope gas analysis in a high dynamic range, high-resolution FERS measurements of natural CO_2 next to N_2 were performed. All present natural

isotopes with typical spectral signatures have been included with the help of a high groove-density dispersive grating at 2400 lines/mm together with a spectrometer slit width of minimum 70 µm (Fig. 4.12 and Fig. 4.13). A spectral resolution of about $1.9\,cm^{-1}$ (FWHM) was obtained.

The fiber-enhanced Raman spectrum of CO_2 was acquired by a laser output power of 0.1 W at a laser wavelength of 532.15 nm and a fiber length of 0.7 m ("HC-580-02"). Two subsequent measurements of pure CO_2 were taken: one for a full peak assignment with a total exposure time of 40 s (Fig. 4.12) as a qualitative measurement, the other for a higher-resolved spectral elucidation of the isotopologues with a total exposure time of 12 s, resulting in a saturation of the CCD pixels from the two most intense CO_2 Raman bands at $1285\,cm^{-1}$ and 1389 cm^{-1}, as a quantitative measurement (not shown).
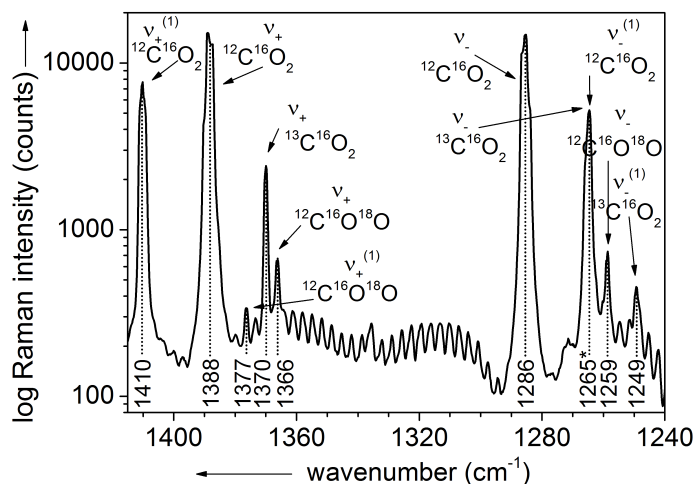

Figure 4.12: Fiber-enhanced high-resolution Raman spectrum of pure CO_2: The Raman spectrum shows in detail the Fermi diad of the different natural isotopes $^{12}C^{16}O_2$ (ν_+ and ν_-), $^{13}C^{16}O_2$ (ν_+ and ν_-, * at 1266 cm^{-1}), and $^{12}C^{16}O^{18}O$ (ν_+ and ν_-), respectively, as well as the hot bands of $^{12}C^{16}O_2$ ($\nu_+^{(1)}$ and $\nu_-^{(1)}$), $^{13}C^{16}O_2$ ($\nu_-^{(1)}$), and $^{12}C^{16}O^{18}O$ ($\nu_+^{(1)}$). (The Raman spectrum was acquired with one single measurement at an acquisition time of 40 s, with 0.1 W laser power at 532 nm, the applied 2400 lines/mm grating, and the 0.7 m long HC-PCF "HC-580-02" at ambient gas pressure and temperature.) [82]

The fundamental symmetric stretching mode ν_1 of CO_2 is Raman active, whereas the bending vibration ν_2 and the asymmetric stretching vibration ν_3 are IR active, but not Raman active. However, the first overtone $2\,\nu_2$ of the CO_2 bending vibration is Raman spectroscopically allowed, but substantially weaker than the fundamental vibration ν_1. Because this overtone vibration and another fundamental are comparable in frequency, they will interact via the anharmonic part of the Hamilton operator if allowed by symmetry. The resulting mixing of the corresponding wave functions leads to a change in Raman signal intensity and frequency shift to 1286 cm^{-1} and 1388 cm^{-1} for the bands ν_1 and $2\,\nu_2$ This was first described by Fermi in 1931 [56]. The resulting doublet band structure in the region of the symmetric CO_2 stretching vibration with frequencies ν_+ and ν_- corresponding to the intensities I_+ and I_- is known in literature as Fermi diad [194, 199, 153, 12, 31, 91, 176, 6, 73]. Next to this diad, weaker so-called hot bands appear due to excitations from the thermally excited state ν_2 with frequencies $\nu_+^{(1)}$ and $\nu_-^{(1)}$ and the condition $\nu_+^{(1)} + \nu_-^{(1)} = \nu_1 + 2\,\nu_2$. The frequencies $\nu_+^{(1)}$ and $\nu_-^{(1)}$ are relatively shifted to the fundamental bands and occur at wavenumbers 1410 cm^{-1} and 1265 cm^{-1} for $^{12}C^{16}O_2$. The Fermi diad of the isotope $^{13}C^{16}O_2$ appears at lower wavenumbers of 1370 cm^{-1} and 1266 cm^{-1} for ν_- and ν_+ next to the hot bands $\nu_-^{(1)}$ and $\nu_+^{(1)}$ at 1249 cm^{-1} and 1390 cm^{-1} (Fig. 4.12, Tab. 4.6). Even the band double structure of the isotope $^{12}C^{16}O^{18}O$ at 1366 cm^{-1} (ν_+) and 1259 cm^{-1} (ν_-) was detected, next to one hot band

at 1377 cm^{-1} ($\nu_+^{(1)}$) and the ro-vibrational fine structure of CO$_2$. Table 4.6 summarizes all detected isotopic bands of measured pure CO$_2$ and compares them to other measured values in literature. It should be noted, that the lower band ν_- (^{13}CO$_2$) of natural CO$_2$ is almost completely covered by the much more intense hot band $\nu_-^{(1)}$ (^{12}C^{16}O$_2$), as well as the band $\nu_+^{(1)}$ (^{13}CO$_2$) by ν_+ (^{12}C^{16}O$_2$) for the specifically used spectral resolution (cf. 4.12).

	^{12}C^{16}O$_2$	^{13}C^{16}O$_2$	^{12}C^{16}O^{18}O
$\nu_-^{(1)}$	1264.6 (1265.3)	1249.3 (1248.7)	– (1250.0)
ν_-	1285.4 (1285.5)	1266.1 (1266.6)	1258.6 (1259.4)
ν_+	1388.8 (1388.2)	1369.9 (1370.3)	1366.1 (1366.0)
$\nu_+^{(1)}$	1410.1 (1409.5)	1390.2 (1388.8)	1376.3 (1376.5)

Table 4.6: Measured vibrational frequencies in cm^{-1} for the Fermi diad, ν_- and ν_+, and the hot bands $\nu_-^{(1)}$ and $\nu_+^{(1)}$ of natural ^{12}C^{16}O$_2$ and its higher concentrated isotopes ^{13}C^{16}O$_2$ and ^{12}C^{16}O^{18}O from Fig. 4.12 in comparison to literature values [95], which are shown in brackets. The hot band $\nu_-^{(1)}$ of ^{12}C^{16}O^{18}O at 1250.0 cm^{-1} was not detected in Fig. 4.12 due to the insufficient spectral resolution, relatively weaker Raman intensity, and an overlap with the stronger hot band $\nu_-^{(1)}$ of ^{13}C^{16}O$_2$ at 1249.3 cm^{-1}.

The baseline subtracted peak area of ^{12}C^{16}O$_2$ was integrated from $1385.6-1395.1$ cm^{-1}, resulting in 150 575 counts and a peak height of 61 968 counts in total for quantitative analysis. The Raman peak noise was determined to 27 counts. The highest Raman peak of ^{13}C^{16}O$_2$ summed up to 1645 counts with 873 counts peak height for 1368.1 - 1371.9 cm^{-1}. Furthermore, the peak area from $1365.0-1367.6$ cm^{-1} resulted in 575 counts and a height of 241 counts for peak assignment for the naturally contained ^{12}C^{16}O^{18}O.

The natural abundance of ^{18}O and ^{13}C are 0.2 % and 1.1 % respectively, resulting in a natural abundance of 1.09 % and 0.39 % for ^{13}C^{16}O$_2$ and ^{12}C^{16}O^{18}O [52]. By comparison of the above-mentioned peaks, an absolute concentration of (1.08 ± 0.03) % and (0.38 ± 0.04) % was determined for the measured isotopes ^{13}C^{16}O$_2$ and ^{12}C^{16}O^{18}O, which is in a very good agreement with the theoretical values.

For the quantitative analysis, the overall measurement was repeated with the identical setup, but the combination of the 660 nm laser and the HC-PCF "HC-633-02" contrary to Fig. 4.12. The fiber length was chosen to 1.2 m together with 0.2 W laser output power. The individual CO$_2$ peaks of the achieve Raman spectrum were integrated and quantified (Tab. 4.7).

^{12}C^{16}O$_2$	ν (cm^{-1})	I_{th}	I_{exp}
$\nu_-^{(1)}$	1264.6	0.05	0.05±0.005
ν_-	1285.4	0.73	0.72±0.02
ν_+	1388.8	1.00	1.00±0.03
$\nu_+^{(1)}$	1410.1	0.08	0.08±0.01
ν_+(^{13}C^{16}O$_2$)	1369.9	0.015	0.014 ±0.002

Table 4.7: Comparison of FERS-based quantified intensities I_{exp} with theoretical values I_{th} [156] for ^{12}C^{16}O$_2$ and the major isotope compound ^{13}CO$_2$. The individual intensity I is related to the strongest band ν_+ for ^{12}C^{16}O$_2$.

In recent years, ^{15}N-labeling experiments have become a powerful tool investigating rates and regulations of microbially mediated nitrogen loss processes in soil by determina-

tion of the fluxes for N_2 and its products [34]. In general, nitrogen is naturally contained to 78.01 vol. % in ambient air. The concentrations of the nitrogen isotopologues are determined to 99.261, 0.737, and 0.0001 % for $^{14}N_2$, $^{14}N^{15}N$, and $^{15}N_2$ [181].
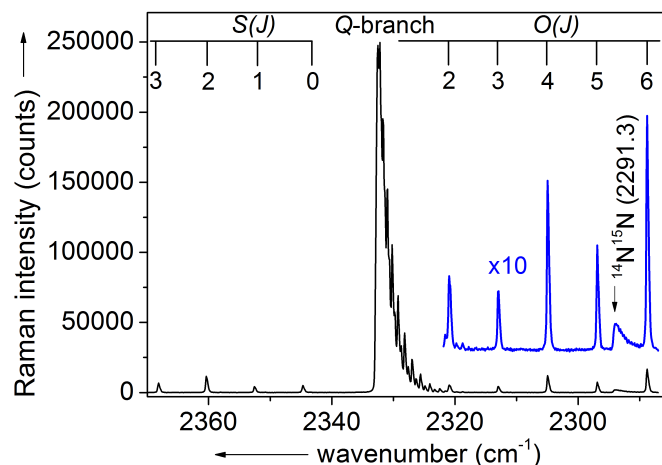

Figure 4.13: Fiber-enhanced high-resolution Raman spectrum of pure N_2: The ro-vibrational fine structure of the *O*- and *S*-branch next to the strong *Q*-branch is resolved. The Raman peak of the $^{14}N^{15}N$ isotope is marked by an arrow. (The Raman spectrum was acquired with one single measurement at an acquisition time of 240 s with 20 mW laser power at 607 nm, the applied 2400 lines/mm grating, and a 1.2 m long HC-PCF "HC-633-02" at ambient gas pressure and temperature.)

The potential of FERS was further shown by the highly sensitive and specific quantification of the nitrogen isotopologues in ambient air at ambient conditions. This high spectrally resolved Raman measurement was achieved by application of the 607 nm cw DPSSL at an output power of 20 mW in combination with a 1.2 m long HC-PCF "HC-633-02" and the help of the 2400 lines/mm grating. The overall exposure time summed up to 240 s. This Raman spectrum is dominated by the *Q*-branch of natural nitrogen at 2329 cm^{-1} (Fig. 4.13). The spectrally resolved *Q*-branch showed the typical asymmetric shape due to different ro-vibrational energy levels with spacing, according to the model of the anharmonic oscillator. Besides, the rotational-vibrational transitions of nitrogen, namely the *O*- and *S*-branches, roughly extending from $2000 - 2600$ cm^{-1} [77]. The boson character of $^{14}N_2$ reveals an intensity alteration with a 6:3 relation of the statistical weight of nuclear spin states for even and odd *J* values (cf. Sec. 2.3). The individual *Q*-branches of $^{14}N_2$ and $^{14}N^{15}N$ were fitted and integrated. The peak area for $^{14}N_2$ from 2328.4 - 2333.9 cm^{-1} and $^{14}N^{15}N$ from $2290.0 - 2294.6$ cm^{-1} resulted in $461\,372$ counts and $3\,223$ counts with a standard deviation of 55 counts for the individual peak noise. The resulting experimentally derived relative abundance with (0.70 ± 0.05) % is in good agreement with the theoretically expected value of 0.74 %. It has to be stated that the spacing of $6\,B$ between *Q*-branch and the closest *O*- and *S*-branch, as well as the spacing of $4\,B$ between each adjacent transition line of *O*- and *S*-branches were accurately detected (cf. Sec. 2.3).

4.5 Summary

In this chapter an advanced FERS setup was presented, which is superior to state-of-the-art fiber- or capillary-based Raman spectroscopic setups in terms of LOD and high spectral resolution, as well as the capability for for fully-automatized gas fillings and multi-gas quantification. The innovative FERS setup was presented leading to an overall high dynamic range of up to 6 orders of magnitude with a time resolution

of seconds and minimum detectable concentration levels in the low ppm range. The simultaneous FERS quantification of climate-relevant gases like CH_4, CO_2, N_2, O_2, and N_2O had been demonstrated next to the straight-forward detection of homonuclear diatomic gases and characteristic isotopes, e.g. $^{13}CO_2$ and $^{13}CO_2$, as well as $^{14}N_2$ and $^{14}N^{15}N$, which are relevant for metabolic pathway monitoring. 27 nL of exhaled human breath, consisting of the low concentrated compounds $^{14}N^{15}N$ and $^{13}CO_2$ next to the major breath components, had been quantified simultaneously over a dynamic range of 4 orders of magnitude with just one single measurement. The great potential of FERS for characterization of greenhouse gas fluxes and bedside clinical diagnosis of metabolic diseases will be further carried out in the next two chapters.

5 Fiber array spectral translator-based Raman imaging of HC-PCF

The previous chapter introduced the analytical potential of FERS for highly sensitive multi-gas measurements in the low ppm-range. Next to a tremendous fiber enhancement with the factor of several thousand compared to conventional Raman spectroscopy, FERS measurements revealed a likewise intrinsically high background and noise level. This Raman noise originated from the fiber's material fused silica, which forms the microstructured region around the hollow core. A Fiber-based Raman gas sensor can extract advantages from the quantitative and qualitative elucidation of this signal distribution coming from the photonic bandgap structure.

The following chapter introduces the fiber array-based spectral translation Raman imaging of different fiber signal distributions for gaseous and liquid filled HC-PCF. The qualitative and quantitative localization of analyte Raman signal and silica Raman signal is shown and discussed.

5.1 Fiber array spectral translator-based Raman imaging (FAST-RI)

The combination of previously introduced FERS with fiber array spectral translator-based Raman imaging [104, 177, 187, 186], which was designed and set up by Michael Brückner [16] enables the spatially-resolved detection of Raman signal across the fiber cross section. A combined setup will be briefly introduced.

Optical design

The hyperspectral (HR) setup, developed and realized by Michael Brückner, is based on hyperspectral Raman imaging and combines multiple concepts [177]. The essential approach for hyperspectral imaging on fiber arrays is a method called fiber array spectral translation (FAST). The main idea is based on imaging the probe's scattering signal, which is collected on a fiber array. One end of this array is connected to spectrometer slit. The linear arrangement of these fibers in the slit plane results in an imaging of the 3-dimensional spectral information to the 2-dimensional CCD detector. FAST offers the advantages of moderately efficient imaging at a full spectral range, which is essentially limited by the spectrometer range, combined with a high spectral resolution [177]. The number of fibers in the array limits the relevant applications for FAST-RI. Nevertheless, Raman spectroscopic imaging of the fiber's cross section with FAST can reveal signal and noise contributions to the Raman gas sensor's SNR. An increased SNR encourages the development of Raman gas sensors with novel types of MOF with moderate attenuation.

The schematic illustration of the setup is shown in Fig. 5.1. This setup enabled the coupling of laser light into both ends of a MOF, which realized the discrimination of forward and backward Raman scattering collection. The switchable laser coupling for forward and backward scattering Raman signal detection was realized by a flipping mirror (FM). Before hitting the mirror, the laser light was expanded via a telescope (T) to later match the fiber's *NA* of 0.2. The expanded beam was then reflected by a Raman edge filter (E_1 or E_2) and coupled via a microscope objective lens (OL_1 or OL_2) into the fiber adapter assembly [62] (A_1 or A_2), which contained the MOF.
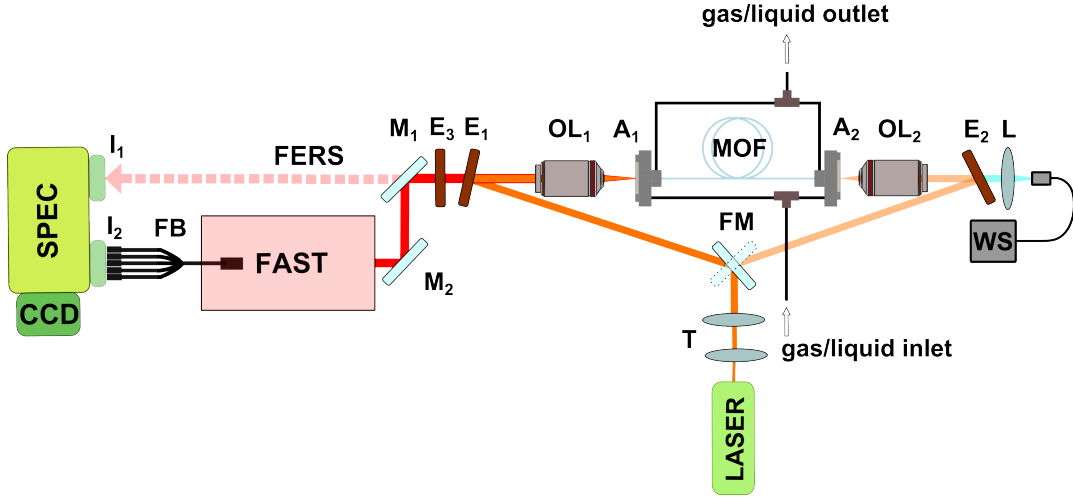
Figure 5.1: Schematic illustration for the combination of the FERS setup with the FAST-RI setup [16] consisting of a laser for the forward and backward scattering option (switchable by a flipping mirror (FM)), telescope (T), edge filters (E$_1$ or E$_2$, E$_3$), two objective lenses (OL$_1$ or OL$_2$), fiber adapter assemblies (A$_1$, A$_2$), microstructured optical fiber (MOF), aspheric lens (L), mirrors (M$_1$, M$_2$), fiber bundle (FB, quadratic-to-slit), spectrometer (SPEC) with 2 input ports (I$_1$, I$_2$) for either FERS- or FAST-measurements, CCD detector, and fiber-based white light source (WS).

Different lasers were used for both arrangements (cf. Tab. 4.1) based on the different HC-PCF. Depending on the excitation wavelength, the laser beam was reflected by the individual long pass edge filter (E$_1$, E$_2$) (cf. Sec. 4.1). The microscope objective lens (OL$_1$ or OL$_2$: "L Plan 20x/0.35 EPI SLWD", Nikon Corporation) with a 20x magnification, a *NA* of 0.35, and a focal length f_{OL} of 10 mm provided a long working distance up to 25 mm. Either back scattered or forward scattered Raman signal was collected and collimated by the same objective lens and passed through the same edge filters (E$_2$ and E$_3$) to eliminate the high amount of Rayleigh scattering signal.

The combination of FAST-RI and FERS enabled either the previously described application of FERS-based monitoring of multi-component gas mixture (red arrow, Fig. 5.1) or the FAST-RI-based inspection of different HC-PCF cross sections described in this chapter (FAST, Fig. 5.1). Without further setup rearrangement, the flipping mirror M$_1$ realized the switching between both applications. Within the FAST-RI part, an amorphous silicon sample was installed for the calibration routine and removed before a FAST-RI measurement [16, 104, 177, 187, 186].

The custom-built fiber optic bundle included 64 single fibers. The fiber bundle was arranged in an 8 × 8 square pattern at the collection end and a 1 × 64 linear stack at the detection end directly connected to the entrance slit of the spectrometer. The white light source (WS) was coupled into the fiber via the microscope objective lens OL$_2$ after being collimated by an achromatic lens L$_1$ with $f = 10$ mm. The fiber end facet together with the transmitted white light could be captured by the CMOS camera within the FAST setup (Fig. 5.1). Adjusting both mirrors M$_1$ and M$_2$ via the coll. "beam walk" allowed to choose the ROI for the fiber cross section before the initiation of a FAST-RI measurement. This procedure was independent of the laser coupling to the fiber. The principle of a FAST-RI measurement is described more detailed in [16]. This chapter will only focus on the FAST-RI-supported measurements and discussion for different HC-PCF signal cross sections.

Spatial resolution

Focusing the Raman signal on the reference sample plane within the FAST part (Fig. 5.1) resulted in a signal *NA* of 0.2. In general, *d* represents the minimal resolvable distance which is the minimum distance between two distinguishable objects/points in an image. The specific image resolution $1/d$ for the diffraction limited optical system with a *NA* of 0.2 is expressed as [161]

$$d = 0.61 \, \frac{\lambda}{NA} = 1.56 \, \mu\text{m} \tag{5.1}$$

for the wavelength λ of 500 nm. The lateral resolution can be improved by a higher *NA* for the optical imaging within the setup. The restriction in lateral resolution by Eq. 5.1 was sufficient for the FAST-RI-based investigation on the Raman signal distribution for different HC-PCF. An overall magnification of 80 for the fiber cross section to the entrance fiber bundle side (FB, Fig. 5.1) was achieved. Thus, one image pixel length of the HR Raman image equaled 1.56 μm in the sample plain (within FAST, Fig. 5.1) of the microstructured optical fiber (Eq. 5.1).

Data processing and correction

Fig. 5.2 schematically shows the typical procedure for a FAST-RI measurement [16, 104, 187, 186]. Before a hyperspectral investigation of the fiber cross section, necessary preparative measurements had to be realized. This included the determination of the background image, of a wavenumber calibration function, of the line/peak shift, and an acquisition of the normalization.

The first step for each measurement series was the acquisition of the background without laser illumination of the reference/fiber sample for the initial background correction. The relative line (or peak) shift of the Raman signal originated from the dispersive feature of the gratings and the dimension of the CCD detector. The preliminary detection of monocrystalline silicon (Fig. 5.3a) as reference sample appeared beneficial for the normalization and wavenumber correction steps. The latter was performed by the analysis of more than one spectral peak and a subsequent linear or polynomial fitting next to the Rayleigh line correction to 0 cm^{-1} for the conversion pixel to wavenumber.
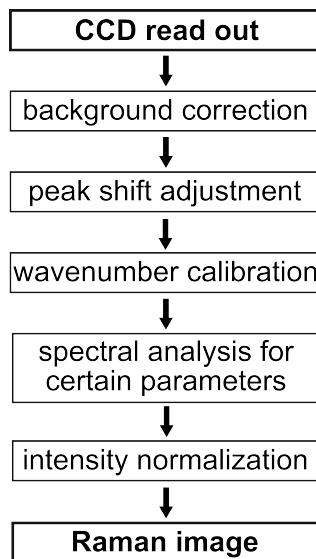

Figure 5.2: Scheme for data acquisition and correction for a single FAST-RI measurement. [16, 104, 187, 186]

The homogenous sample illumination was followed by a homogenous illumination of

the fiber bundle with scattered light from the sample. Imaging of the linear fiber array onto the CCD detector resulted in a transfer function of the fiber bundle (Fig. 5.3b). Different transmission of different bundle fibers, as well as the spectrometer imaging, mainly contributed to this transfer function resulting in a normalization error, i.e. the maximum deviation to the mean value of the intensity for all pixels. The integration over 30 pixels for the silicon phonon vibration at $521\ \mathrm{cm^{-1}}$ represented the reference for the normalization. Implementing this normalization process decreased the error for the transfer function down to $(3.1 \pm 0.6)\,\%$ (Fig. 5.3b).
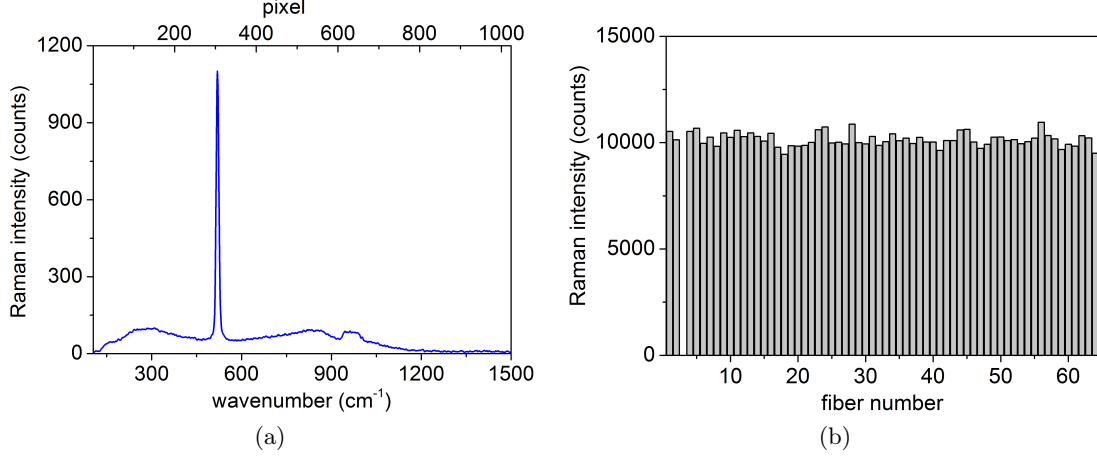

(a) (b)

Figure 5.3: (a) Raman spectrum of monocrystalline silicon with characteristic phonon band shift at $521\ \mathrm{cm^{-1}}$. (b) Raman intensity for transfer function of the fiber optic bundle done by integrating and averaging of the silicon peak over 30 pixels around $521\ \mathrm{cm^{-1}}$. Fiber #3 was damaged and therefore not used throughout all the experiments. (532 nm excitation wavelength, 300 mW laser power, 5 s exposure time, 5 accumulations, 600 lines/mm grating)

Measurement parameters

Unless otherwise stated, the measurement parameters for the following results are listed in Table 5.1.

fiber	arr.	analyte	λ_{exc} (nm)	P_0 (mW)	L (m)	T (%)	p (bar)	meas. time (s)	Fig.
HC-580-02	f	H_2	532	0.2	0.7	22	5	5×5	5.8
	b	H_2	532	0.2	0.7	27	5	5×5	5.8
	b	H_2	532	0.2	1.0	15	5	5×5	5.9
HC-633-02	b	N_2	660	0.3	1.0	70	5	5×2	5.6
	b	H_2/N_2	660	0.3	1.5	60	5	5×5	5.7
HC-1060-02	b	EtOH	532	0.05	0.3	16	70*	5×1	5.11

Table 5.1: Important measurement parameters used for different FAST-RI measurements of hydrogen, nitrogen, and ethanol (EtOH): laser excitation wavelength λ_{exc}, laser power P_0, HC-PCF length L with corresponding laser beam transmittance T, absolute pressure p inside the fiber, and the total measurement time as accumulations × exposure time. HC-PCF [145, 146, 144, 142] (NKT Photonics) for different arrangements (f: forward scattering, b: backward scattering) and different analytes are listed. The corresponding FAST Raman images are stated and will be described in more detail in the following sections. *70 bar differential pressure were used to fill the HC-PCF non-selectively from one fiber end.

5.2 FAST-RI of Raman signal distributions in HC-PCF

Hollow-core fiber sensors have to fulfill a low attenuated guiding mechanism for a wide range of applications [30, 47, 114, 175]. Simplifying the fiber design as much as possible would make such sensors more practical and useful for commercialization. Nevertheless, simplified HC-PCF lead to confinement loss [120, 75] and all applications struggle certain bending losses for gaseous, selectively, and non-selectively filled HC-PCF [2]. The real-time Raman imaging of fiber cross sections can reveal information, which is useful for the design, fabrication, and revision of these drawbacks for novel types of microstructured fibers.

Here, an optimal overlap of the fiber core mode field and the analyte for highly efficient and simplified Raman fiber sensors is sought. Such an investigation in Raman signal distribution was performed by the utilization of FAST-RI in this chapter. In doing so, HC-PCF were hyperspectrally analyzed for the Raman signal distribution of different gaseous analytes. Especially the signal distribution at a low wavenumber region of < 1300 cm^{-1} turned out to be relevant for analytical comparison of fiber-silica and analyte Raman signal. Molecular hydrogen and its pure vibrational Raman shifts cover this region [77]. It is therefore of particular importance to initially discriminate the Raman spectroscopic features of molecular hydrogen.

5.2.1 Raman spectroscopic discrimination of molecular hydrogen

Fig. 5.4 shows a typical (a) ro-vibrational and (b) pure rotational Raman spectrum of molecular hydrogen, which was measured within a HC-PCF. The vibrational Raman transition of hydrogen is dominated by the separated Q-branch lines around 4155 cm^{-1} (Fig. 5.4a). Although these vibrational transitions occur at a very high wavenumber region > 4000 cm^{-1} with relatively high HC-PCF attenuation losses for the Raman signal, the hydrogen Q-branch is still detectable due to a generally high enhancement by the FERS setup.
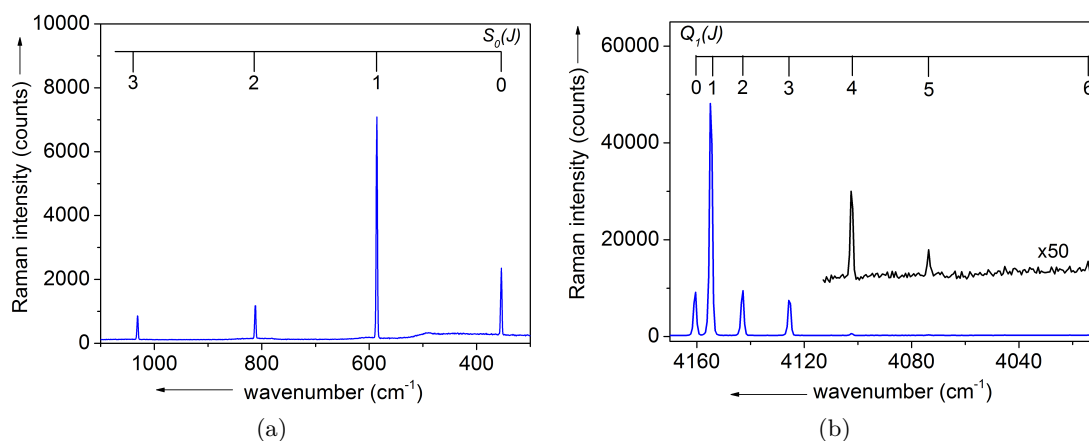

Figure 5.4: (a): Fiber-enhanced rotational Raman bands of the rotational hydrogen S-branch (for 660 nm laser wavelength, 372 mW laser power, and an acquisition time of 0.4 s). (b): Fiber-enhanced ro-vibrational Raman bands of the vibrational hydrogen Q-branch (for 607 nm laser wavelength, 23 mW laser power, and an acquisition time of 100 s). The black spectrum was 50 times enhanced for a better illustration of the low intensive Q-branch transitions at smaller wavenumbers. Both spectra for 5 vol. % H_2 in rest carrier gas N_2 were measured with the help of a 600 lines/mm grating and a 0.5 m long HC-PCF "HC-633-02" at $p_{abs} = 6$ bar and $T = 21$ °C.

The characteristic bands of the hydrogen Q-branch are determined by the thermal population of rotational ground state energy levels with an intensity relation of 3:1 between odd and even J values due to different spin states (cf. Sec. 2.3). To obtain

the initial energy state population, the vibrational energies of molecular hydrogen can be inserted into Eq. 2.6. This results in $N_{\nu_1}/N_{\nu_0} \simeq 10^{-6}$. Therefore it can be assumed, that hydrogen is in the vibrational ground state at ambient conditions. Since hydrogen is allocated in two nuclear spins $I = 1$ and $I = 0$, the vibrational Raman transitions $Q_1(0)$, $Q_1(2)$, $Q_1(4)$, and $Q_1(6)$ are related to para-H_2, whereas $Q_1(1)$, $Q_1(3)$, and $Q_1(5)$ are related to ortho-H_2 (Fig. 5.4a). The vibrational line $Q_1(1)$ at 4155.2 cm^{-1} shows the highest intensity under ambient conditions [77].

The excitation energies of the rotational transitions are $\sim kT$, thus several excited states are usually populated at room temperature. For the rotational Raman spectrum of hydrogen at lower wavenumbers, i.e. $300 - 1300$ cm^{-1}, para-H_2 is represented by the states $S_0(0)$ and $S_0(2)$, whereas $S_0(1)$ and $S_0(3)$ are belonging to ortho-H_2 [77]. The most intensive rotational hydrogen band at 587.1 cm^{-1} refers to $S_0(1)$ and will be thoroughly examined within this thesis (Fig. 5.4).

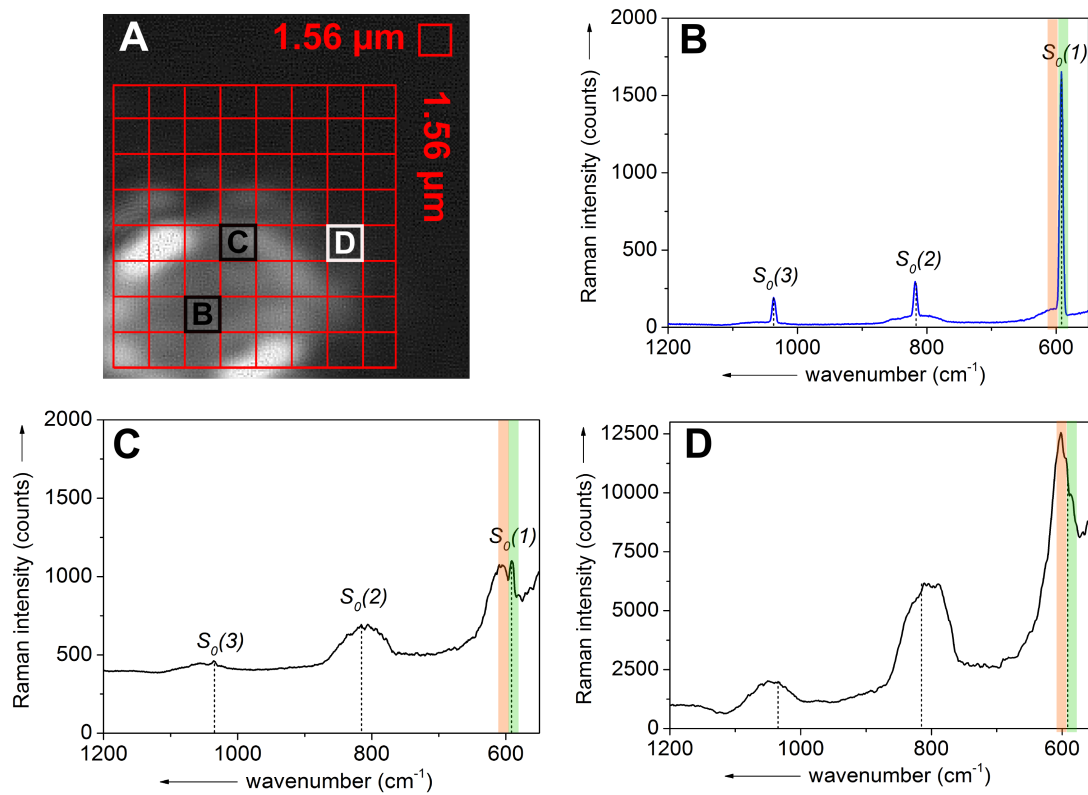### 5.2.2 Raman signal and silica background distribution

Figure 5.5: Example of FAST-RI for the HC-PCF "HC-633-02" filled with 5 vol. % molecular hydrogen in rest carrier gas nitrogen. A: Microscopic image of fiber cross section with transmitted light from a white light source. The ROI for the Raman signal collection is marked by the red 8×8 squared area. B-D: 3 Raman spectra were collected from 3 characteristically different fiber regions: (B) the center of hollow fiber core, (C) the edge of the fiber core, and (D) the microstructured region surrounding the fiber core. All 3 graphs exemplarily show the different Raman spectroscopic content of hydrogen signal (pure rotational bands $S_0(1) - S_0(3)$) and silica background signal guided in the hollow fiber core and surrounding microstructured region of the HC-PCF. The green (red) marked region further illustrates the contribution of the pure rotational hydrogen band $S_0(1)$ (silica D_2 band) to the signal distribution over fiber cross section for the resulting FAST-RI graph shown in Fig. 5.7.

The applied FAST method is very rapid compared to other hyperspectral techniques, which are normally using an acousto-optic modulator (AOM) for individual scans along the spectral region [177]. The modal distribution of a fiber cross section can change tem-

porally fast due to e.g. laser coupling instabilities or thermal drifts. Long measurement times, therefore, would not reflect instantaneously achieved hyperspectral information. In this case, a FAST-RI graph, which can be obtained within seconds, overcomes the drawback of long acquisition times for standard techniques.

Figure 5.5 together with Fig. 5.7 show an exemplary FAST-RI measurement of H_2 in the HC-PCF "HC-633-02". This HC-PCF consisted of a hollow core with a diameter of $(5.8 \pm 1)\,\mu m$ and a microstructured region with a dimension of $\sim 37\,\mu m$ [146]. The microscope image of the fiber end facet with transmitted white light in Fig. 5.5 was captured by a CMOS detector (within FAST, Fig. 5.1) before the initiation of a FAST Raman imaging process. The white light illumination demonstrates the mechanism of the photonic bandgap effect. The white light was mainly guided in the hollow fiber core and further to a high amount in the inner ring of honeycomb-like fiber cladding region. The 8×8 squared area (red, Fig. 5.5A) illustrates the ROI including the region of the hollow core and the first ring of the microstructured region, which was hyperspectrally imaged within one single measurement. Although the fiber structure and corresponding guiding mechanism was identifiable by the microscopic image, an additional utilization of FAST-RI revealed information on the different signal distribution (Fig. 5.7).

Three characteristic areas of the hyperspectrally investigated fiber cross section are exemplarily shown in Fig. 5.5. The Raman signal of the gaseous analyte was mainly guided in the hollow core (B). The Raman spectrum in (D) defines a superposition of weak hydrogen Raman signal at the outer fiber core region and a high content of silica Raman signal, which was guided within the hollow core. The inner ring of the microstructured region (C) confined the silica Raman signal and nearly no Raman intensity of molecular hydrogen is detectable (Fig. 5.5). The modal distribution of both, gas Raman signal and parasitic silica Raman signal, can be identified immediately with the help of FAST-RI in one single measurement. Therefore, the Raman signal of the strongest vibrational hydrogen band $S_0(1)$ at 587 cm^{-1} and the silica band D_2 around 606 cm^{-1} (Fig. 3.8) have been individually integrated for each Raman spectrum. An interpolated 8×8 pixels FAST Raman image was the result (Fig. 5.7).
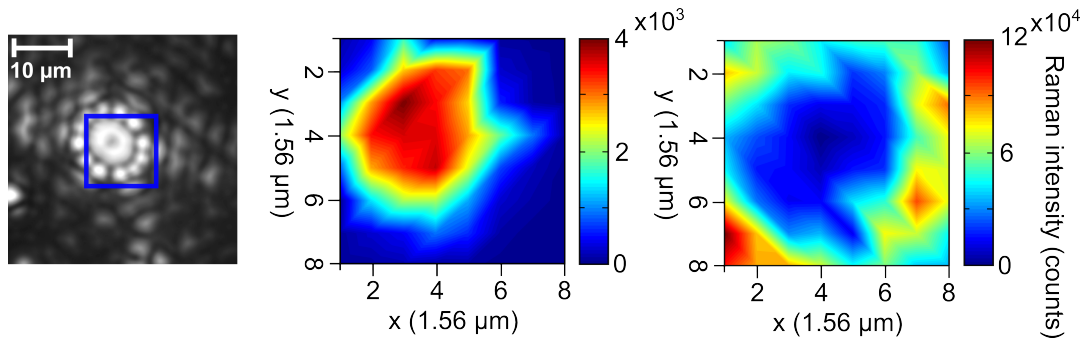

Figure 5.6: Left: Microscopic image of fiber cross section ("HC-633-02") with transmitted light from a white light source (WS, Fig. 5.1). The blue frame indicates the ROI with a dimension of $12.5\,\mu m \times 12.5\,\mu m$. FAST Raman images of the vibrational nitrogen Raman band were integrated around 2331 cm^{-1} (middle) and for the fluorescence contribution of silica around 2500 cm^{-1} (right). Both FAST Raman images are interpolated for better illustration of the guiding mechanism. Measurement parameters can be found in Tab. 5.1.

Another example for the Raman signal contribution of molecular nitrogen at 2331 cm^{-1} is shown in Fig. 5.6. The Raman signal distribution for nitrogen mirrors that of hydrogen in Fig. 5.7. Nevertheless, only the less intense fluorescence content of silica Raman signal in the higher wavenumber region will contribute parasitically to the nitrogen signal at these high wavenumber regions with > 2000 cm^{-1} (cf. Fig. 3.8). The honeycomb-like shape of the microstructured region is partly resolved by the signal distribution of the

silica Raman signal. Isolated signal peaks in Fig. 5.6 (right) most likely refer to these structural properties of the cladding and the highly attenuated PBG-like light guidance in each single of its small hollow cores (cf. Sec. 3.4).

5.2.3 Photonic bandgap effect and Raman signal distribution

The already presented microstructured cladding region in the form of hexagonal-shaped honeycombs provides a 2-dimensional photonic bandgap effect for these fiber types. Depending on the structure parameters like pitch and air hole diameter, the number of hole rings and the dimension of the hollow core primarily define the bandgap characteristics for the designed wavelength region [10]. The designed spectral transmission window usually spans around 100 nm in the VIS range. Especially for the margins of this spectral bandgap region, e.g. around the margins 530 nm and 630 nm for the HC-PCF "HC-580-02", the attenuation is relatively high. This is the consequence of a stronger signal leakage from the hollow core into the surrounding microstructured cladding region [10].

In contrast, the utilized HC-PCF "HC-633-02" is designed for the VIS-IR region with a design wavelength of 633 nm and the photonic bandgap spans from 605 - 750 nm [146]. The applied excitation laser at 660 nm is spectrally close to the designed wavelength and will be guided with low attenuation losses. However, the effective transmission window for a multi-component gas mixture will be spectrally limited to 750 nm, which equals a wavenumber region of 1800 cm^{-1}, i.e. is slightly higher than the typical fingerprint region to 1500 cm^{-1} (cf. Fig. 3.6).

The FAST-RI-obtained signal distribution for the rotational hydrogen Raman band at a low wavenumber region (587 cm^{-1}) was compared to the vibrational Raman band of nitrogen at a high wavenumber region (2331 cm^{-1}) within a Raman fingerprint region < 3000 cm^{-1} for Fig. 5.7. The 660 nm excitation laser in combination with the HC-PCF "HC-633-02" was utilized for this measurement. The hydrogen Raman signal at 686 nm featured a low attenuation by the plateau-like photonic bandgap (Fig. 3.6), whereas the nitrogen Raman signal spectrally outside the designed bandgap at 780 nm underwent a major attenuation. The latter was related to a stronger leakage into the microstructured cladding region resulting in a higher mode field diameter (MFD) (Fig. 5.7). The 19$\times$ higher concentrated molecular nitrogen showed only a 2$\times$ higher Raman signal intensity compared to molecular hydrogen due to its relatively strong signal attenuation (cf. Fig. 3.6).
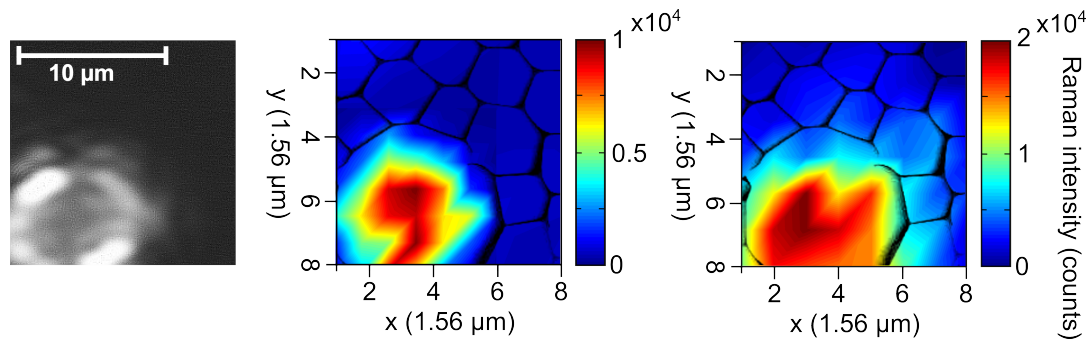

Figure 5.7: Microscopic image (left) of the HC-PCF cross section ("HC-633-02") with transmitted light from a white light source and a dimension of 12.5 μm × 12.5 μm. The corresponding FAST Raman images for the rotational hydrogen band $S_0(1)$ integrated around 587 cm^{-1} (middle) and the vibrational nitrogen band integrated around 2331 cm^{-1} (right) are further shown. Both FAST Raman images are interpolated and an exemplary honeycomb-like HC-PCF structure is overlayed (black) for better illustration of the guiding mechanism, respectively.

5.2.4 Raman signal comparison of forward and backward Raman scattering

Hollow-core photonic bandgap fibers present a unique guiding mechanism based on a honeycomb-like microstructured cladding region formed by fused silica. For the resulting silica Raman signal it was predicted, that it mainly arose from the cladding structure. Furthermore, it will be most effectively guided within the hollow fiber core next to the analyte Raman signal. The combination of FAST-RI and FERS represented an excellent option to quantitatively and qualitatively compare the signal and noise distribution for forward and backward Raman scattering signal collection without any further setup modifications (Fig. 5.1). In doing so, the 532 nm excitation laser in combination with the HC-PCF "HC-580-02" for feasible subsequent FAST-RI experiments of both fiber end cross sections were used under same experimental conditions.

Fig. 5.8 shows the microscopic white light image and the FAST Raman image comparing the forward and backward scattering Raman signal collection by integrating the vibrational hydrogen band $S_0(1)$ at 587 cm^{-1} and the D_2 silica Raman band at 606 cm^{-1}, respectively.
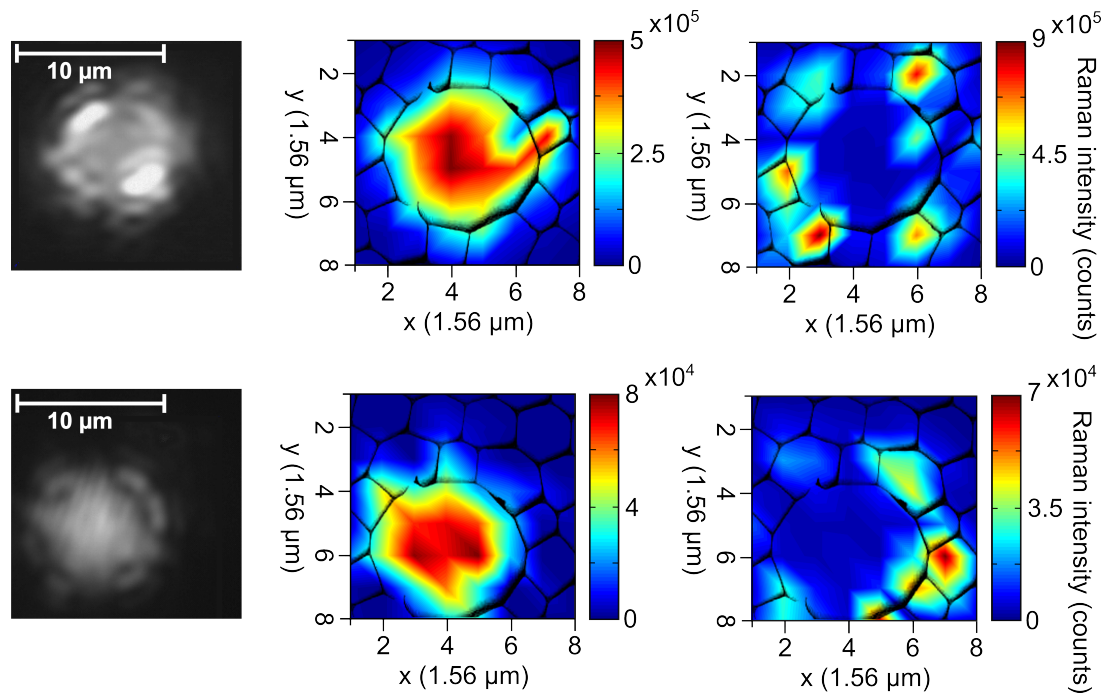

Figure 5.8: Microscopic image of the "HC-580-02" fiber cross section with a dimension of 12.5 μm × 12.5 μm illuminated by transmitted light from a white light source (left) with corresponding FAST Raman image of the vibrational hydrogen band $S_0(1)$ at 587 cm^{-1} (middle) and the D_2 Raman band of silica integrated around 606 cm^{-1} (right) applying the forward (bottom) and backward (top) scattering arrangement (cf. Fig. 5.1). All FAST Raman images are interpolated and an exemplary honeycomb-like HC-PCF structure is overlayed (black) for better illustration of the guiding mechanism, respectively.

The highest intensity of the hydrogen Raman signal emitted from the hollow fiber core was more than 5× higher for backward scattering arrangement compared to forward. Both signals can be described with a Gaussian-like mode [145, 146], where most of the Raman signal is confined inside the core. However, the real inhomogeneous honeycomb structure of the microstructured cladding and imperfection of the core will deform the Raman signal. This effect seemed to be clearer for the backscattering arrangement since the strongest Raman signal will be generated within the first centimeters of the HC-PCF (Fig. 5.8 bottom middle).

Furthermore, an overlap of the strong laser mode and the fiber silica material will

generate major silica noise at the illumination fiber end. The forward scattering arrangement in combination with sufficiently long fiber lengths could "clean" this parasitic silica noise signal distributed inside the inner ring of the microstructured region, because of its poor optical guidance. This effect can be further emphasized by the utilization of even longer fibers. However, fiber lengths substantially longer than the effective fiber length will lead to an additional attenuation of the analyte Raman signal guided inside the hollow core (cf. Sec. 3.5). In Fig. 5.8, the hydrogen Raman signal inside the core, as well as the silica Raman signal in the microstructured region, was attenuated by this mechanism. Forasmuch, the highest intensity of the silica Raman signal is $\sim 10\times$ lower for the forward compared to the backward scattering arrangement. For each individual FAST Raman image in Fig. 5.8, the Raman signal intensity was manually background corrected and integrated since a generally automatized fitting procedure for the silica Raman signal contribution turned out to be difficult, i.e. due to peak shifts and different peak shapes along the fiber cross section. The individual silica noise contribution was then set in relation to the individual hydrogen signal intensity. Comparing both relations of the backward and forward scattering collection, the latter could decrease the relative noise contribution by a value of (18 ± 9) %.

In summary, silica Raman noise suppression resulting in a general SNR improvement can be achieved by two methods:

1. The higher silica noise contribution for the backward scattering configuration primarily arose in the outer fiber core region. It could be filtered by an appropriate spatial pinhole. This technique will be introduced in the next chapter.

2. The forward-scattered silica Raman signal will be substantially filtered within the poorly guiding honeycomb-like microstructure of the fiber cladding. The fiber length has to be chosen such that large contributions of this noise signal will be cleaned under preservation of the analyte Raman signal. Thus, the effective fiber length governed by the attenuation characteristics has to be meticulously chosen in advance for the application of the forward scattering configuration.

5.2.5 Raman signal distribution for fiber bending

Using the HC-PCF "HC-580-02" in combination with excitation laser light at 532 nm introduced several characteristics: (1) Since the laser wavelength at 532 nm is spectrally located at the edge of the photonic bandgap, even minor fiber instabilities will dramatically change the guiding properties for the excitation laser light. These laser intensity instabilities will result in Raman signal instability independent of the Raman signal guiding governed by the fiber attenuation. (2) A certain fiber bending or a difference in absolute gas pressure inside the fiber will affect this sensitive guiding mechanism as well. Sufficient bending will introduce losses for the coupled laser mode and Gaussian-like Raman signal inside the core. This is a consequence of the individual signal, which is confined in the core and is provoked to leak to the surrounding cladding ring by deforming the structure through fiber bending [121]. (3) Only an increase in the number of cladding rings can strongly reduce the fiber bending losses [2]. Nevertheless, this number is fixed by the fiber design and subsequent fiber drawing process.

The influence of fiber bending on the modal characteristics for the backward scattered Raman signal was investigated for two different bending diameters with the help of FAST-RI. Respectively a bending diameter of 3 cm and 10 cm for a 1.5 m long HC-PCF "HC-580-02" in combination with an excitation laser wavelength of 532 nm were applied. The resulting FAST Raman image for the vibrational hydrogen band $S_0(1)$ integrated around 587 cm^{-1} and the D_2 silica Raman band integrated around 606 cm^{-1} are shown in Fig. 5.9.

The decrease in bending radius from infinity (Fig. 5.8) to 10 cm resulted in a certain Raman signal modification for the fiber core. The deformation for the Gaussian-like Raman signal of molecular hydrogen and a spatial peak shift from the fiber center in one direction to the surrounding first cladding ring resulted (Fig. 5.9). Contrary, the silica Raman signal was located at the edge of the hollow core almost congruent with the center of gravity of the hydrogen signal. When the bending radius was decreased to 3 cm, this characteristic strongly evolved (Fig. 5.9 right). The maximum silica Raman intensity increased and the fundamental mode further deformed with a general stretching to the inner ring of the microstructured cladding on one axis.
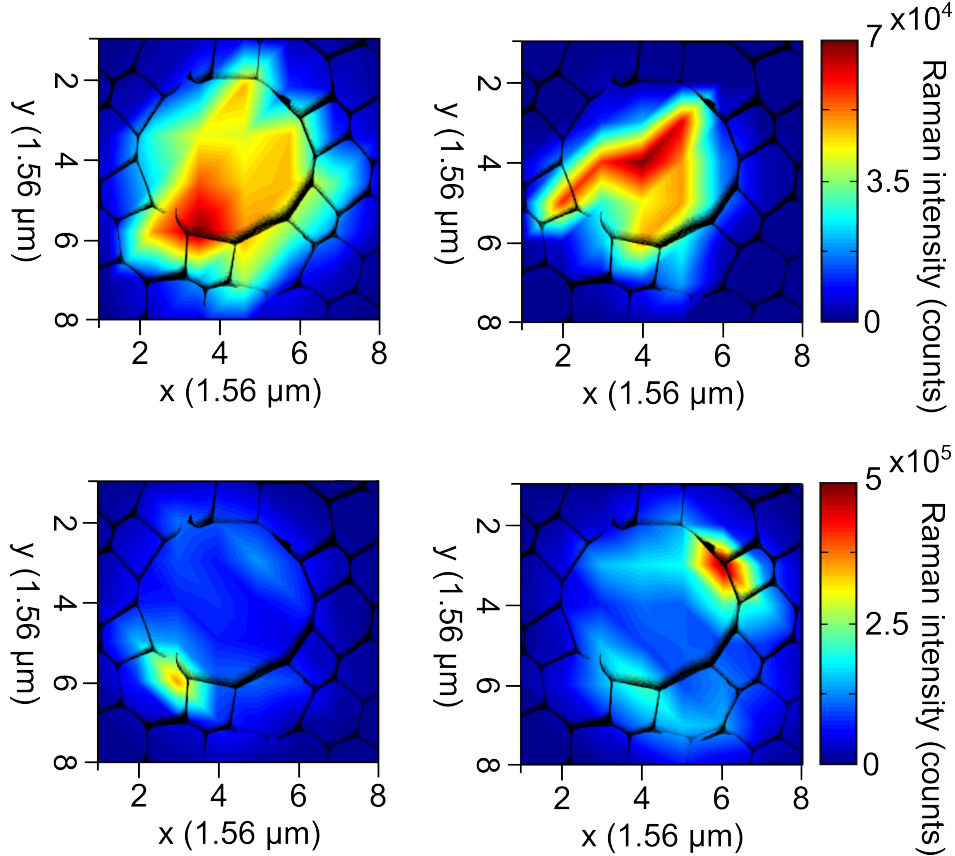

Figure 5.9: Resulting signal distribution for induced fiber bending losses of the HC-PCF "HC-580-02" at 532 nm excitation laser wavelength. All FAST Raman images correspond to the vibrational hydrogen Raman band $S_0(1)$ at 587 cm^{-1} (top) and the D_2 silica Raman band integrated at 606 cm^{-1} (bottom) for a bending radius of 10 cm (left) and 3 cm (right) in opposite directions. All FAST Raman images are interpolated and an exemplary honeycomb-like HC-PCF structure is overlaid (black) for better illustration of the guiding mechanism, respectively.

The brief analysis on fiber bending for two different bending radii much smaller than the minimally recommended demonstrates qualitatively the influence of this strong effect on the Raman signal distribution. FAST Raman imaging of Stokes signal on the effect of extreme fiber bending in relation to the photonic bandgap guiding mechanism in HC-PCF has been shown for the first time. These events should be avoided if experiments are carried out with these special fibers.

5.2.6 FAST-RI of non-selectively liquid-filled HC-PCF

Liquid-core filled HC-PCF have been applied successfully as biosensors in literature [106, 108, 107]. One possibility is filling the hollow core selectively with the analyte-solution mixture and leaving the small cores of the surrounding microstructured region

untouched. This can be achieved by different techniques: (1) either filling the holes with UV-curable glue with the help of deducing different flow velocities for the hollow core and holes of the microstructured region, (2) or applying a collapsing technique [183]. After closing the small holes for each procedure and the following selective filling of solution to the fiber core, splicing at the point of unaffected bandgap structure will lead to an attenuated total internal reflection (ATIR) for this type of preparation [13]. Such time-consuming sample filling is not suitable in a clinical environment, which requires simple and rapid detection methods.

Another possibility is filling the entire fiber. Filling the hollow core, as well as the microstructured cladding region, leads to a non-selectively filled fiber [39]. Further, the photonic bandgap and its characteristically wavelength transmission band will be shifted significantly compared to its gas filled counterpart [107]. The excitation wavelength will not match that of the non-filled HC-PCF. The bandgap shift is governed by [10]

$$
\lambda = \lambda_0 \left[\frac{1 - \left(\frac{n_{\text{liq}}}{n_{\text{SiO}_2}} \right)^2}{1 - \left(\frac{n_{\text{air}}}{n_{\text{SiO}_2}} \right)^2} \right]^{1/2} , \tag{5.2}
$$

where λ_0 is the wavelength for the original bandgap and the fiber' refractive indexes for fused silica n_{SiO_2} and air n_{air}, next to that for the filled hollow cores with liquid solution changing n_{air} to n_{liq}.

Usually, different liquid solvents like water and ethanol with refractive indexes of 1.33 and 1.36 at 589.29 nm are used for liquid fiber sensing. If the HC-PCF "HC-1060-02" (NKT Photonics) [142] (cf. Fig. 3.5) with center wavelength of 1060 nm for gaseous analytes is non-selectively filled by either water or ethanol, a bandgap shift to the VIS spectral region will result in accordance to Eq. 5.2. More specifically, a wavelength shift for $\lambda_0 = 1060\,\text{nm}$ to $\lambda_{\text{EtOH}} \cong 531\,\text{nm}$ ($\lambda_{H_2O} \cong 601\,\text{nm}$) for ethanol (water) with $n_{\text{SiO}_2} = 1.4607$ and $n_{\text{air}} = 1$ at 532 nm will be the consequence [172].
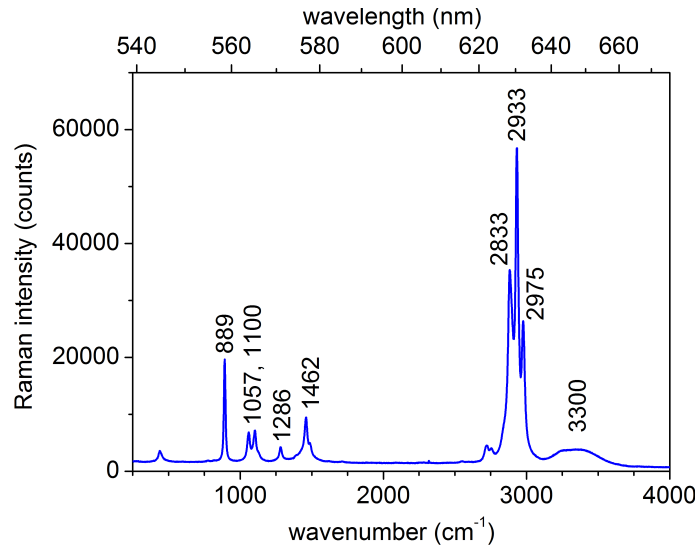

Figure 5.10: Raman spectrum for an ethanol filled glass cuvette. (50 mW laser power, 532 nm excitation wavelength, 2 s exposure time, 600 lines/mm grating, 100 µm slit width)

Fig. 5.10 shows the Raman spectrum of ethanol in the typical fingerprint region. The fiber was assembled with both ends into the fiber adapters (Fig. 4.2). Then the fiber was filled with ethanol (96 % from Sigma-Aldrich) by a pressure difference of 70 bar via an ultra-high performance/pressure liquid chromatography (UHPLC) pump (X-LC 3185PU pump, Jasco Inc.) at the distel-end. The achieved FAST Raman image for the

backward Raman scattering arrangement is shown in Fig. 5.11. Three individual Raman spectra representing (A) the center of the fiber core, (B) edge of the core, and (C) the first ring of the microstructured region are plotted together with the microscopic image of the fiber end facet. The characteristic C-C stretching band of ethanol at 889 cm^{-1}, as well as the D_2 silica Raman band at 606 cm^{-1} are conspicuous in the Raman spectrum "A". Both Raman bands were integrated resulting in two different FAST Raman images for Fig. 5.11, bottom left and right. In comparison, the symmetrical C-H stretching ethanol band at 2933 cm^{-1} (cf. Fig. 5.10) was integrated and resulted in the FAST-RI graph of Fig. 5.11, bottom middle.
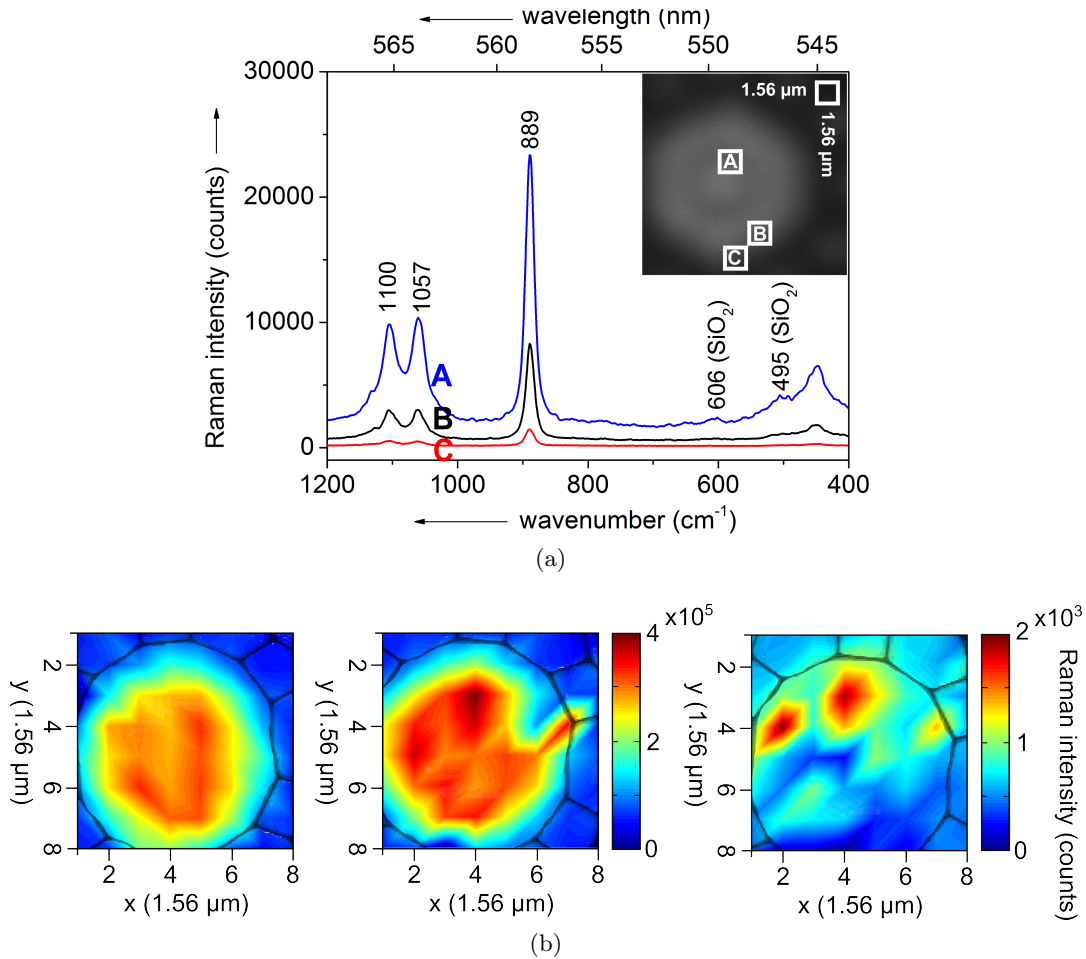

Figure 5.11: (a): 3 ethanol Raman spectra for different spots (A-C) on the fiber cross section: The ethanol was non-selectively filled into the HC-PCF "HC-1060-02". Inset: Microscopic image of the fiber cross section with transmitted light from a white light source. The regions A-C illustrate the simultaneous FAST-RI collection of the corresponding Raman spectra. (b): FAST Raman images of 2 different ethanol bands integrated around 889 cm^{-1} (left) and 2933 cm^{-1} (middle), and the D_2 silica Raman band integrated around 606 cm^{-1} (right): All FAST Raman images are interpolated and an exemplary honeycomb-like HC-PCF structure is overlayed (black) for better illustration of the guiding mechanism, respectively.

The Gaussian-like Raman signal of both ethanol bands is completely confined inside the filled hollow core with a comparable MFD. This is a consequence of the shifted broad transmission window with low attenuation up to ~ 650 nm including the fingerprint region up to 3000 cm^{-1}. The more intense ethanol Raman band at 2933 cm^{-1} compared to that for 889 cm^{-1} (Fig. 5.10) further revealed a higher FAST-RI signal intensity (Fig. 5.11).

Similar to the previous findings of the FAST Raman signal imaging for gaseous ana-

lytes (Fig. 5.6, 5.8), it was expected that a silica Raman signal content will be present within liquid-filled HC-PCF, but to a fairly low amount. This contribution was hyperspectrally resolved in Fig. 5.11. The silica noise signal was mainly confined within the filled hollow core, but not in the first microstructured cladding ring. However, the signal intensity was more than 2 orders of magnitude lower than that of the ethanol Raman signal. Contrary to the earlier results, a possible spatial filtering of the silica noise proves to be difficult since it was located to a high content in the fiber core next to the solvent signal. Filtering out this signal will consequently cut out analyte signal. A resulting increase in SNR for the utilization of a spatial pinhole is put in question (cf. Chap. 6). Although the maximum intensity of parasitic silica Raman signal was low (Fig. 5.11), the detection of low concentrated biological, chemical, pharmaceutical, or medical analytes (e.g. mefloquine [62], creatine [129], cyanocobalamin [191]) in liquid solvents like water or ethanol in HC-PCF will lead to Raman signal intensities at the same level. It is predicted, that the Raman signal detection of the solved analyte present in traces requires spatial filtering of the silica background noise for concentration levels in the μmol range.

5.3 Summary

FAST-RI-based experiments for different HC-PCF, either gas or liquid filled, were carried out. Two facts make the measurement and the constructional combination unique: (1) The utilization of HC-PCF within the FERS setup provided high Raman signal enhancement leading to rapid FAST imaging with adequate SNR levels. (2) The utilized FAST-RI buildup, designed by Michael Brückner, realized a fast imaging technique, since an AOM in combination with a wavelength scanning is not required. A time resolution of several seconds resulted. Both accounted for a precise and fast Raman imaging process for signal contributions of a novel type of fiber for different analytes and measurement conditions. In comparison, other scanning or AOM-based hyperspectral imaging techniques can comprise coupling instabilities or even Raman signal changes on a second time scale.

fiber	arr.	gas/liquid component (Raman shift)	Fig.	$d_{\text{theo.}}^{\text{core}}$ (μm)	MFD$_{\text{theo.}}$ (μm)	MFD$_{\text{exp.}}$ (μm)
HC-580-02	f	H_2 (587 cm^{-1})	5.8	6.6 ± 1	5.3 ± 1	7.3 ± 1.5
	b	H_2 (587 cm^{-1})	5.8	6.6 ± 1	5.3 ± 1	7.9 ± 1.6
HC-633-02	b	N_2 (2331 cm^{-1})	5.6	5.8 ± 1	4.4 ± 1	7.0 ± 1.4
HC-1060-02	b	C_2H_6O (889 cm^{-1})	5.11	10 ± 1	7.5 ± 1	8.8 ± 0.8
	b	C_2H_6O (2933 cm^{-1})	5.11	10 ± 1	7.5 ± 1	9.2 ± 1.1

Table 5.2: Comparison of the manufacturer-specified fiber core diameter $d_{\text{theo.}}^{\text{core}}$ and mode field diameter MFD$_{\text{theo.}}$ ([145, 146, 142]) compared to the experimentally obtained MFD$_{\text{exp.}}$ for different HC-PCF. The arrangement (f: forward scattering, b: backward scattering) and corresponding previously introduced FAST Raman images are listed.

The different MFD were obtained from the Raman intensity distributions following the "International Organization for Standardization" (ISO) 11146 standard. The analyte Raman signal for each FAST Raman image in Fig. 5.6 - 5.9 and Fig. 5.11 was fitted by a pseudo-Voigt profile with major contribution by a Gaussian function. The experimentally determined MFD in comparison to the manufacturer-specified fiber core diameter $d_{\text{theo.}}^{\text{core}}$ and mode field diameter MFD$_{\text{theo.}}$ resulted (Tab. 5.2). For HC-PCF in the VIS range, the experimentally determined MFD always exceeded the specified

manufacturer values. Regarding the fiber cross section as product of the preceding fiber processing of fiber stripping, cleaving, and cleaning, the fiber end facet faced certain imperfections next to a deficient PBG structure. Both observations mitigated for the HC-PCF "HC-1060-02", which featured an almost perfect microstructured cladding region on a larger scale (cf. Fig. 3.5) in comparison to that for the VIS range. Further, the highly suitable core diameter for VIS-laser applications resulting in reduced parasitic silica Raman signal from the quartz glass microstructure, as well as a distinguished laser and Raman signal guiding.

In summary, the Raman signal distribution on the fiber cross section could be qualitatively and quantitatively analyzed by the implementation of the existing FERS setup into a FAST-RI setup. The difference between forward and backward scattering FERS built-up led to the result that a forward scattering signal collection provided an intrinsically higher SNR for gaseous analytes filled inside the hollow core. Nevertheless, the optimal fiber length has to be known in advance, which makes the application of forward scattering less easy-to-apply. With these findings, the utilization of a spatial pinhole function for a backward scattering collection will be rather applied within an improved FERS setup (Chap. 6). It will turn out, that this implementation could increase the sensitivity in terms of LOD down to the ppb region in comparison to the previous chapter.

Bending sensitivities and resulting losses play a major role for the analytical accuracy and precision of such a fiber Raman multi-gas sensor. It was shown that instabilities like rapid pressure differences inside the fiber or extreme fiber bending are counteracting the sensor's robustness and long-term detection stability. Especially applying a HC-PCF with the Raman excitation wavelength spectrally located at the PBG boundary will make the fiber sensor susceptible for this performance. As a consequence, experiments with the HC-PCF "HC-633-02" are presented throughout the next chapter. Particularly, utilization of either the 607 nm or the 660 nm excitation laser will cover the low attenuation PBG fiber (Fig. 3.6) and still provide a sufficient relative transmission window without the previously discussed susceptibilities.

6 Optimizing Stokes Raman scattering in gas-filled HC-PCF

In the previous two chapters the design and application of FERS was introduced and further combined with an additional FAST-RI setup. The Raman spectroscopic imaging of different HC-PCF cross sections pointed out the origin of parasitic silica Raman signal distribution. Generally, this prevented a further noise content reduction for the Raman gas sensor accuracy in terms of precision and sensitivity. This chapter will introduce an improved FERS setup based on the findings in the two preceding chapters. Finally, the arising potential of FERS for clinical diagnostics of metabolic disorders in terms of human breath analysis will be introduced and discussed.

6.1 Silica Raman signal reduction

6.1.1 Improved FERS setup

Given the findings of the last chapters, the existing FERS setup from Fig. 4.1 was modified. Chap. 5 effectively demonstrated the statistical content of parasitic silica background Raman signal inside the hollow fiber core. With these findings, it is obvious that the spatial filtering of the silica Raman signal will cause a tremendous Raman noise level decrease. The ability of monitoring in the low concentration region could introduce Raman spectroscopy and especially FERS as a game changer for new applications such as clinical diagnostics for metabolic disorders and diseases.
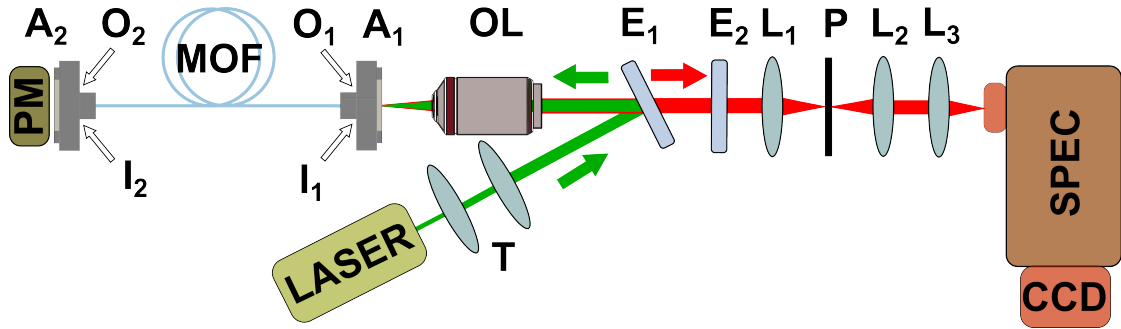

Figure 6.1: Schematic sketch of the improved FERS setup consisting of laser, telescope (T), edge filters (E_1, E_2), objective lens (OL), fiber adapter assemblies (A_1, A_2) with input (I_1, I_2) and output ports (O_1, O_2) respectively, microstructured optical fiber (MOF), power meter (PM), telescope consisting of two achromatic lenses (L_1, L_2) with spatial pinhole (P) in the focal plane, aspheric lens (L_3), spectrometer (SPEC), and CCD detector (cf. Fig. 4.1).

The improved FERS setup shown in Fig. 6.1 is based on the built-up from Sec. 4.1 and the applied modifications are listed below:

1. The dichroic beam splitter reflecting the laser beam into the microscope objective lens was replaced with an excitation-wavelength specific long-pass Raman edge filter (E_1) (cf. Sec. 4.1). This resulted in a generally higher laser beam reflectivity of $\sim 99.99\,\%$ compared to $\sim 98\,\%$ for the so far used dichroic beam splitter. A small incident angle $< 5\,°$ for the Raman edge filter minimized any beam displacement

or distortion for the Raman signal transmission or laser beam reflection compared to the 45 °-arrangement.

2. A Keplerian telescope was implemented after the second Raman edge filter (E_2). The telescope consisted of two achromatic doublet lenses with focal length of $f_1 = 35$ mm and $f_2 = 40$ mm (Fig. 6.1: L_1, L_2). Based on the findings of the FAST-RI investigations, spectral filtering or modification can be optically applied within the image plane after the first lens L_1 [22].

3. Consequently, the backscattered Stokes Raman signal was spectrally filtered from the silica Raman signal by a pinhole (P) at the image plane within this telescope. The signal filter function will be described.

6.1.2 Spatial pinhole function

Although the hollow fiber core comprises most of the optical power in the center for the Gaussian-like Raman signal distribution, a small content of silica Raman signal located at the outer fiber core will propagate as well (cf. Chap. 5). The overall detection sensitivity will benefit by a spatial cut-off for this distinct spatially distributed silica Raman signal. The first approach is the restriction of silica Raman signal radiated from the microstructured region surrounding the core. This signal contribution is characterized by a *NA* larger than that guided within and radiated from the central hollow fiber core. To restrict or even cut-out these signal contributions, two mechanisms were added in the previous FERS setup from Chap. 4 (Fig. 4.1).

1. Initially, the collimated silica Raman signal was removed with the help of a spatially adjustable pinhole for the collimated beam after the Raman signal collection by the microscope objective lens. Nevertheless, silica Raman contributions from the central core region would be still present to a relatively high amount in the analyte Raman signal.

2. The circular Raman signal was imaged from the fiber cross section to the slit plane, which resulted in an approximate diameter of 45 µm and 278 µm for the hollow core and microstructured cladding of the HC-PCF. Secondly, the described binning option of the CCD detector could be controlled as a vertical Raman signal filter. Binning of 5 vertical pixel rows will collect the core-originated Raman signal of the gaseous analyte, but leaving out the silica Raman signal, that originated from the outer part of the hollow core. This most likely would be extended to the adjacent vertical pixels on the CCD array. Furthermore, the spectrometer slit width should be reduced down to ~ 50 µm to cut out most of this silica Raman signal in the horizontal direction.

These techniques can be easily applied to conventional Raman spectroscopic setups, especially the second method, which would not require additional optical elements. The resulting reduction in complexity and quantity of optical elements, therefore, can be beneficial for potential sensor miniaturization.

6.1.3 Improved spatial pinhole function

The detection of Raman signal for very low concentrated tracers with both applied methods in combination was still insufficient. This is partly obvious at the low wavenumber region < 1000 cm^{-1}, referring to the so far FERS-based measurements of the low concentrated multi-gas mixtures in Chap. 4. Silica Raman signal originating from the hollow core center with a fiber $NA \leq 0.2$ will not be filtered by the cut-off-like pinhole function

regarding a collimated Raman signal. Additively, the fiber cross section should be imaged before the CCD detector and spatially cleaned by removing parasitic silica Raman signal. Thus, an additional pinhole (P, Fig. 6.1) was added to the basic FERS setup from Chap. 4. The microscope objective (OL, $f = 10\,\mathrm{mm}$) and the first achromatic lens (L$_1$, $f = 35\,\mathrm{mm}$) magnified the fiber core end facet with diameter of $\sim 6\,\mathrm{\mu m}$ and MFD of 4.4 µm to an effectively expanded diameter of 21 µm and 15 µm in the focal plane at the pinhole position (P). Different pinholes sizes of 10, 15, 25, 30, and 50 µm were used to quantitatively analyze the SNR of the Stokes Raman signal and optimize the Raman gas sensor in terms of sensitivity (Fig. 6.2a)[1].
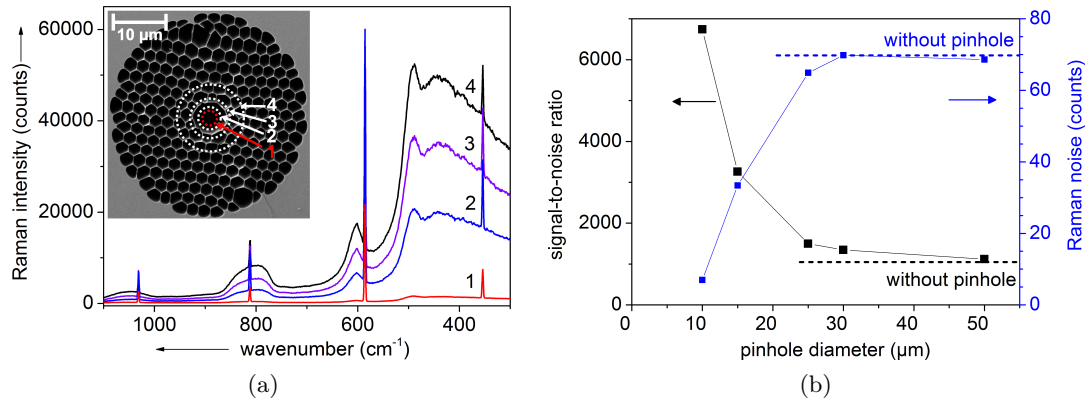

Figure 6.2: (a): Fiber-enhanced rotational Raman spectrum of the rotational hydrogen *S*-branch with underlying silica Raman signal background. The reduction of the silica background with the help of an additional filtering pinhole is shown for several diameters: 10 µm (1), 15 µm (2), 25 µm (3), no pinhole (4). Inset: REM image of the fiber end-face, where the circular areas marked with 1, 2, 3, and 4 equal to the collection areas for the pinholes sizes 10, 15, 25, and 50 µm (i.e. effectively no pinhole) in the Fourier plane, whereas the red circle illustrates the hollow-core diameter (Fig. 6.1), respectively [79]. (b): Evaluated SNR (black) and Raman noise (SD, blue) for the applied pinhole sizes with diameter 10, 15, 25, 30, and 50 µm. The rotational hydrogen line $S_0(1)$ from (a) was fitted and integrated around 587 cm^{-1}, respectively.

The smallest pinhole size with a diameter of 10 µm represented an effective collection diameter of 2.9 µm at the fiber end face ("1", Fig. 6.2a). This size resulted in a minor reduction of Raman signal for the rotational hydrogen Raman transitions and more importantly in a major cut-out of parasitic silica Raman signal. Applying the smallest pinhole led to the best improvement in SNR for the specific rotational hydrogen band $S_0(1)$. Here, the Raman signal was increased by a factor of 6 and the Raman peak noise (SD) was reduced by 10. The quantitative dependency of SNR (black) and peak Raman noise (blue) on different pinhole diameters is illustrated in Fig. 6.2b. Thus, the application of pinhole diameters larger than 15 µm, which corresponded to a MFD of 4.4 µm, did not provide any beneficial noise filtering.

In order to quantify the enhancement of the improved FERS setup, the vibrational hydrogen Raman peak at 587 cm^{-1} was first analyzed for the improved spatial pinhole. Secondly, only the spatial pinhole (Fig. 4.1) was applied and finally, under identical conditions, the HC-PCF was carefully removed from the fiber assembly adapter and an-

---

[1]Albeit, the presented optical magnification of the fiber core's Raman signal will decrease the optical resolution and thus will make it harder to filter the spatially less separated signal in the image plane (P, Fig. 6.1), 2 facts have to be considered: (1) The minimal pinhole size was restricted to a minimum diameter of 10 µm for the mentioned MFD of 4.4 µm. (2) A reduction in the Raman signal imaging factor by applying an achromatic lens with smaller focus length (than the objective lens focal length) will consequently increase the Raman signal *NA* before entering the spectrometer slit. A higher signal *NA* than the spectrometer *NA* would result in a collected Raman signal decrease, if the setup will not be modified.

alyzed without any filtering as a reference. The individual SNR was related to acquisition time, different laser output power and fiber pressure. The resulting normalized SNR in units of $(\text{bar} \cdot \text{mW} \cdot \sqrt{\text{s}})^{-1}$ and the stated enhancement factors of all 3 arrangements are quantitatively summarized in Tab. 6.1.

H_2 - $S_0(1)$ band	int. peak intensity I_{peak} (counts)	peak noise σ_{peak} (counts)	SNR	normalized SNR $((\text{bar} \cdot \text{mW} \cdot \sqrt{\text{s}})^{-1})$	enhanc. factor
conventional	2778	0.40	6945	0.2	1
spat. pinhole	6083	0.56	10863	210.7	1053
impr. pinhole	59367	1.20	49473	1049.7	5249

Table 6.1: Comparison of the detection ability for hydrogen in the case of conventional Raman spectroscopy, i.e. the detection of the focus volume, and FERS in combination with a spatial (cf. Fig. 4.1) or the improved spatial pinhole (cf. Fig. 6.1) as described by means of SNR and enhancement is tabulated. The SNR was normalized to time $\sqrt{t}$, laser power P_L, and pressure p for better comparison. The investigated rotational hydrogen peak $S_0(1)$ was integrated from $583.4 - 589.0$ cm^{-1}.

Relative signal enhancements of 1053 and 5249 were derived for the FERS configuration with applied spatial (Fig. 4.1) and improved pinhole (Fig. 6.1) in contrast to conventional Raman spectroscopy without the utilization of a MOF (Tab. 6.1). The corresponding Raman spectra can be found in the Appendix A (Fig. A.3).

6.2 Performance of improved FERS setup

6.2.1 Highly sensitive hydrogen detection

Raman spectroscopic comparison of molecular hydrogen   The Raman spectroscopic characteristics of molecular hydrogen was introduced in Sec. 5.2. Furthermore, the advantages and disadvantages for the FERS-based detection of either the vibrational Q_1-branch or the rotational S_0-branch in molecular hydrogen as either the most intense vibrational or pure rotational Raman transition at room temperature has to be carefully examined and balanced against each other.

hydrogen transition	fiber trans. (%)*	int. peak intensity I_{peak}	peak noise σ_{peak}	SNR	norm. SNR $((\text{bar} \cdot \text{mW} \cdot \sqrt{\text{s}})^{-1})^+$
$S_0(1)$	75.0	18296	5.5	3327	11
$Q_1(1)$	0.2	59236	12.5	4739	1

Table 6.2: Comparison of the fiber transmission, peak intensity, peak noise, and the resulting SNR for the most intense rotational and vibrational modes of hydrogen at room temperature is presented. * The fiber transmission values were obtained for a 0.5 m long "HC-633-02" at the wavelength 686 nm and 812 nm referring to the hydrogen transitions $S_0(1)$ at 660 nm excitation and $Q_1(1)$ at 607 nm excitation. $^+$ The experimental parameters can be found in Fig. 5.4.

The fiber bandgap characteristics of the HC-PCF "HC-633-02" in combination with the DPSS laser emitting at 660 nm provided low attenuation for the pure rotational hydrogen bands. However high losses at high wavenumber regions around 4150 cm^{-1} were present independently of the used excitation laser wavelength, i.e. the utilization of the 607 nm DPSS laser (cf. Fig. 3.6).

A thorough examination revealed that the S_0-branch have advantages over the Q_1-branch with regard to quantitative analysis:

1. The Q_1-branch at the high wavenumber region is effectively silica Raman background-free and no other molecular ro-vibrational bands (of the multi-gas analyte) will emerge in contrast to the low wavenumber region. Nevertheless, the characteristic fiber bandgap provides high attenuation losses at this high wavenumber region > 3000 cm^{-1} (see Tab. 6.2). This loss cannot be sufficiently compensated.

2. The relative Raman scattering cross sections for the most intense S_0-branch is larger than that for the Q_1-branch at ambient conditions independent of the excitation wavelength in the VIS (see Tab. 2.2). Extremely low fiber attenuations for the rotational S_0-branch in combination with high laser output powers at 660 nm excitation wavelength and the introduced pinhole-based Raman signal filter led to a generally higher SNR for the detection of the pure rotational hydrogen transitions.

3. Conclusively, by rigorously examining the SNR of the strongest pure rotational and (ro-)vibrational peak of hydrogen, it was found that the SNR of the $S_0(1)$-branch was 11 times higher compared to the $Q_1(1)$-branch (Tab. 6.2).

Determination of LOD One drawback for the FERS-based detection of rotational hydrogen bands is the parasitic background Raman signal of the fiber silica material itself. The consequent LOD restriction was overcome by the introduction of the improved spatial pinhole-filter function (Sec. 6.1). The linear scaling for the hydrogen Raman signal with decreasing H_2 concentration down to 10 ppm molecular hydrogen in carrier gas nitrogen has been shown earlier in Fig. 4.9. This minimum detectable concentration could be further minimized through cutting out the fiber silica signal, which is concentrated at the outer core region.
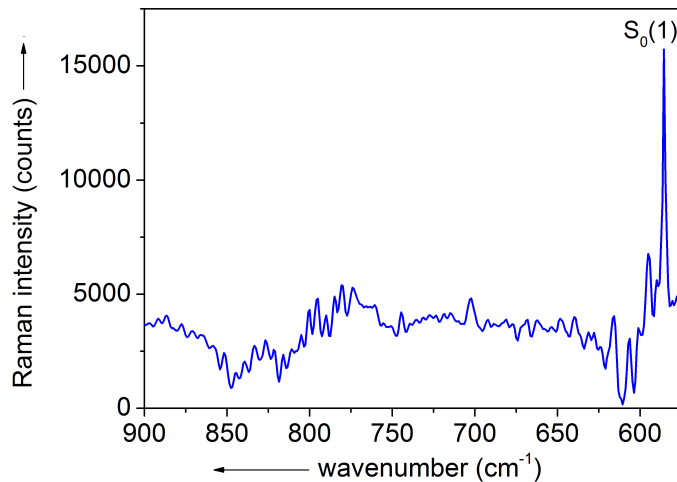

Figure 6.3: Raman spectrum of 5 ppm H_2 in 95 ppm N_2 with rest Ar. The peak height of the strongest rotational hydrogen band $S_0(1)$ at 587 cm^{-1} is 11239 counts. The standard deviation of the noise was determined to be 229 counts. The noise-equivalent LOD equals 306 ppb for the condition SNR = 3. (0.6 W laser power at 660 nm excitation wavelength, 1.5 m long HC-PCF "HC-633-02", 600 lines/mm grating, 15 s acquisition time, $p_{abs} = 9$ bar, and $T = 21\,°C$)

The consequent expansion of the overall detection range of 7 orders of magnitude for molecular hydrogen at a minimum noise-equivalent LOD of ~ 300 ppb is shown in Fig. 6.3. Here, a preceding measurement of 0 ppm H_2 in Raman-inactive Ar at the same parameters was spectroscopically subtracted from the measurement of 5 ppm H_2. For

the latter[2], a peak height of 11239 counts together with a standard deviation of 229 counts resulted by integrating the rotational hydrogen band $S_0(1)$ around 587 cm^{-1}.

Sensor response time   The demands on hydrogen sensors are the indication of concentrations in the range of $0.01 - 10$ vol. % (safety) or $1 - 100$ vol. % (fuel cells) accompanied by fast response and recovery times of ~ 1 s, simple operation and maintenance, as well as sufficient accuracy and sensitivity in the range of $< 5 - 10$ % [85]. A FERS-based hydrogen detection fits all these requirements and is therefore suitable for a wide field of hydrogen detection [139]. In order to specify the sensor response, it was necessary to conduct the hydrogen Raman signal evolution for concentration changes of hydrogen between 1, 2.5, and 3 vol. %. These concentration differences are present around the lower flammability limit (LFL) of 4 vol. % for hydrogen in atmosphere [115]. The FERS setup in Fig. 6.1 was applied together with the introduced mid-pressure system for filling the fiber with an accurately concentrated gas mixture provided by the MFC system. In order to ensure fast filling rates in the range of several seconds, the fiber was filled at an absolute pressure of 2 bar for the individual gas mixture. It has to be stated, that a minimal pressure difference of ~ 0.2 bar was required for the gas flow by MFC operation. According to Eq. 3.8, a theoretical filling time of 27.1 s concluded for the used HC-PCF "HC-633-02" with 0.5 m length at $d_{\mathrm{core}} = 5.8$ µm and $\Delta p \simeq 1$ bar. Every 3 seconds a single Raman spectrum with 1 s of total exposure time was acquired (Fig. 6.4).
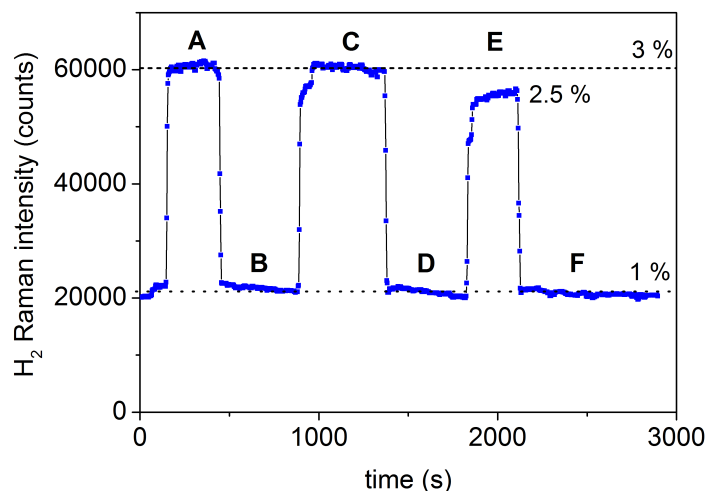

Figure 6.4: Temporal sensor response for FERS-based hydrogen detection with changing hydrogen concentrations of 1.0, 2.5, and 3.0 vol. % as indicated in the graph. The individual acquisition time was 1 s with a time resolution of 3 s. A 0.5 m long HC-PCF "HC-633-02" in combination with 0.2 W laser output power at 660 nm excitation wavelength (with 600 lines/mm) was experimentally used. The HC-PCF was filled by a pressure difference of ~ 1 bar to atmospheric pressure. The most intense rotational hydrogen Raman transition $S_0(1)$ was automatically fitted and integrated for the concentration monitoring. The presented MFC system was applied to provide the different hydrogen concentrations through the accurate dilution of an initial mixture of 5 vol. % hydrogen in rest carrier gas nitrogen mixture with pure argon. The different plateaus A-F are evaluated in Tab. 6.3.

The most intense rotational hydrogen Raman band $S_0(1)$ was fitted and integrated automatically via the LabVIEW software, thus concentration monitoring for a predefined calibration data set was the result. The data of integrated peak intensity, peak noise, and precision for each concentration step is summarized in Tab. 6.3. The precision for

---

[2]It has to be mentioned, that the performed subtraction of pure Ar Raman signal (i.e. parasitic silica Raman signal) was used for illustrative purpose in Fig. 6.3. A general subtraction of another spectrum will increase the noise by $\sqrt{2}$, since the variation in signal and blank are additive [127].

all 3 repetitive steps of 1.0, 2.5, and 3.0 vol. % ranged from $0.9-2.6\%$ (Tab. 6.3). Given the applied pressure difference of 1 bar between fiber input and output during filling, the signal evolution appeared within a mean response time t_{90} of 27.0 ± 2.0 s in accordance to the predicted response time of 27.1 s. Generally, higher pressure differences up to 9 bar (compared to the applied 1 bar) would theoretically lead to lower filling times (t_{90}) of 4.5 s. Therefore, a generally faster responsive hydrogen sensor can be easily realized by applying either higher pressures or shorter fiber length with an accompanied decline in achievable LOD.

plateau	A	B	C	D	E	F	unit
H_2 concentration (%)	3.0	1.0	3.0	1.0	2.5	1.0	
response time t_{90}	25.9	25.6	27.3	29.0	30.0	24.2	s
precision σ_{stat}/I_{mean}	0.8	1.7	0.9	2.6	0.9	1.9	%

Table 6.3: Sensor response evaluation for the plateaus A-F from Fig. 6.4: Different concentrations of 1.0, 2.5, and 3.0 vol. % in terms of the response time t_{90} and precision σ_{stat}/I_{mean} over time have been examined respectively. The measurement parameters can be found in Fig. 6.4.

6.2.2 Simulation of multi-component breath gas analysis

The previously presented results proved fiber-enhanced Raman gas analysis to be highly sensitive for several multi-gas applications in clinical diagnostics superior to showing no cross-sensitivity, comprising of non-invasiveness, being label-free and painless. Exhaled molecular hydrogen, as well as the VOC methane, serves as a biomarker for colonic fermentation [67]. Molecular hydrogen in the concentration of several to tens of ppm within exhaled breath is only generated during anaerobic metabolism linked to metabolic disorders including lactose intolerance, fructose malabsorption, and bacterial overgrowth syndrome [27, 53, 66, 69]. The detection method of these metabolic disorders and diseases by the so-called hydrogen breath test (HBT) is well-known in literature [68, 67, 171].

In order to establish FERS as a novel miniaturized technique for easy and fast performance of HBT in terms of simultaneous methane and hydrogen detection, the spectral fingerprint of both by the combination of pure rotational and (ro-)vibrational Raman spectroscopy was rigorously examined. Previously, a 11 times higher SNR for the rotational band $S_0(1)$ over the vibrational band $Q_1(1)$ was shown for molecular hydrogen (Tab. 6.2). The combination of rotational and vibrational Raman spectroscopy for simultaneous hydrogen detection with other gas molecules within a fiber-limited spectral range is of fundamental importance for further miniaturization. This can be realized through compact spectrometers with fixed gratings and limited spectral ranges with a suitable resolution [81]. It was feasible to monitor the concentrations of hydrogen and methane selectively within a complex gas mixture such as exhaled human breath including the major compounds N_2, O_2, $^{12}CO_2$, and $^{13}CO_2$ as shown in Fig. 6.5. With a beneficially characteristic Raman spectroscopic fingerprint for each individual component, a simultaneous FERS monitoring of such a complex multi-gas mixture consisting of CO_2, O_2, N_2O, CH_4, and H_2 with each 1 vol. % and rest N_2 was acquired for the first time. Here, the utilization of the 607 nm DPSS laser at 62 mW output power, a 1.5 m long HC-PCF "HC-633-02", and the 1800 lines/mm grating resulted in an acquisition time of 4 s (Fig. 6.5).
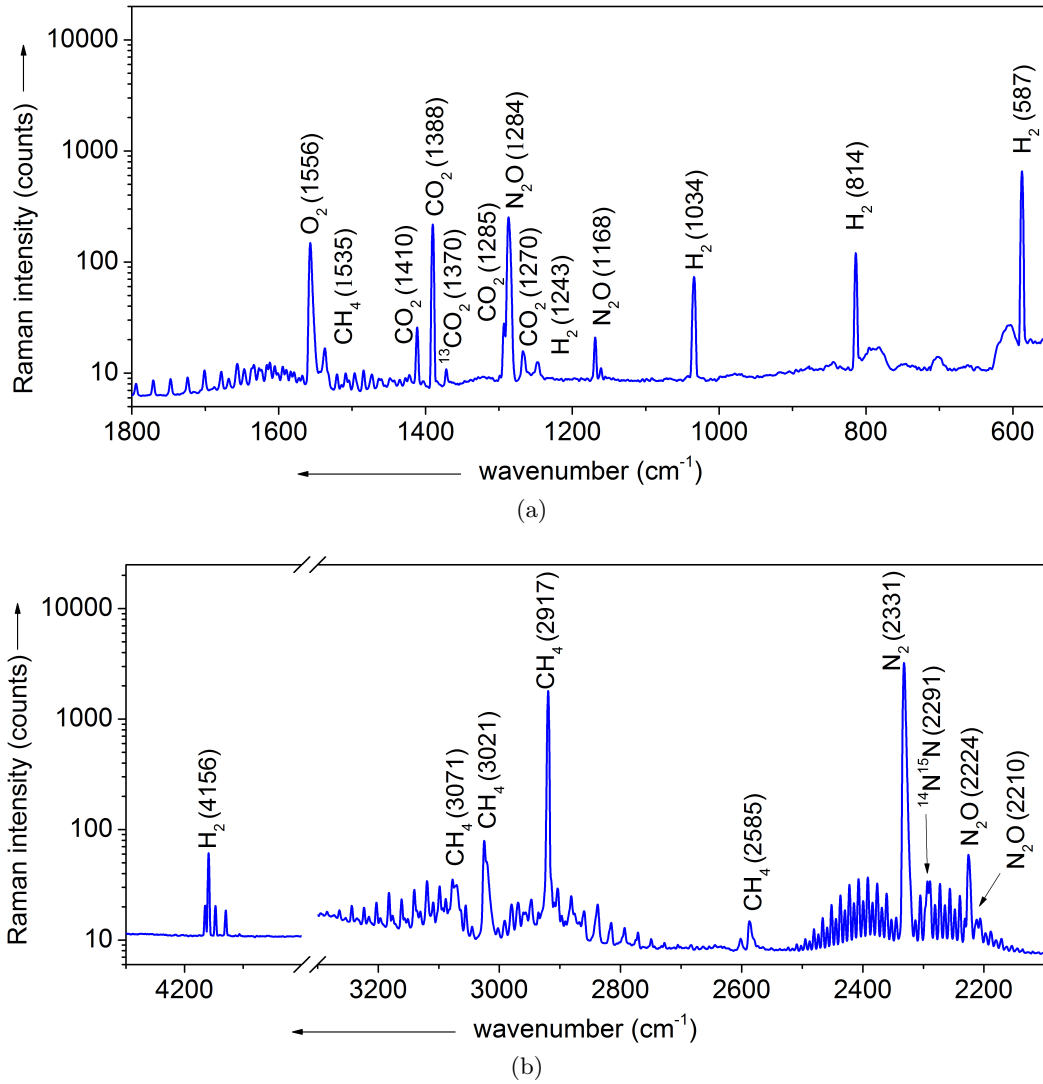
Figure 6.5: Fiber-enhanced Raman spectrum for the combination of pure rotational and ro-vibrational bands of a complex gas mixture. The 1800 lines/mm grating was used within the experiment. (a): Pure rotational Raman bands of H_2 and ro-vibrational Raman bands of $^{12}CO_2$, $^{13}CO_2$ N_2O, O_2, CH_4, and N_2 in the wavenumber region $550 - 1800$ cm^{-1}. (b): Ro-vibrational Raman bands of N_2O, $^{14}N_2$, $^{14}N^{15}N$, CH_4, and H_2 in the wavenumber region $2100 - 4300$ cm^{-1}. The highly resolved spectrum was acquired in 4 s of measurement time with the help of the 607 nm laser at 62 mW output power in combination with a 1.5 m long HC-PCF "HC-633-02" (at $p_{abs} = 6$ bar and $T = 21\,°C$). Each investigated gaseous compound was concentrated with 1 vol. % respectively with rest nitrogen [79].

Besides the so far investigated spectral signature of hydrogen, the typical Fermi diad of the major natural $^{12}CO_2$ and the diad of its hot bands had been identified in Fig. 6.5. Both Q-branches of the symmetric stretching mode ν_1 at 1286 cm^{-1} and the first overtone of the bending mode $2\,\nu_2$ at 1388 cm^{-1} are obvious. Furthermore, the hot bands at 1270 and 1410 cm^{-1}, as well as the naturally concentrated $^{13}CO_2$ at 1370 cm^{-1}, could be detected. The high-resolution spectrally-resolved Raman spectrum was further dominated by the Q-branch of $^{14}N_2$ at 2331 cm^{-1}. This Raman transition band was accompanied by rotational transitions, namely the O- and S-branch, which show the typical $(2J+1)$-degeneracy in combination with the Boltzmann distribution ($\sim \exp(-J^2)$). Furthermore, the intensity alternation of 2:1 from the statistical weight of the nuclear spin states of even and odd J within the ro-vibrational $^{14}N_2$ transitions became apparent. Likewise, the $^{16}O_2$ exhibited a ro-vibrational fine structure around the Q-branch

transitions at 1556 cm^{-1}. Contrary to $^{14}N_2$ with its total nuclear spin of $I = 1$ and the resulting intensity variation, this Q-branch of $^{16}O_2$ was accompanied by rotational lines with only odd J due to a total spin number of $I = 0$ (cf. Sec. 2.3). Molecular methane shows many vibrational transitions, namely the C-H symmetric stretching band ν_1 including a rotational fine structure, the asymmetric stretching mode ν_3, the bending mode ν_2, and the bending mode overtone $2\nu_4$, which can be observed in Fig. 6.5. All rotational and ro-vibrational assignments are summarized and referenced in Tab. 2.2.

Simulated Raman-spectroscopic hydrogen breath test Molecular hydrogen with concentrations higher than 20 ppm will only be observed in exhaled breath of diseased patients due to anaerobic metabolism of the colon bacteria *Escherichia coli* [151]. An increase of 20 ppm above the basal concentration within 90 min after oligosaccharide ingestion is considered as a positive HBT [42]. Contrary, the cut-off value of 12 ppm over basal concentrations after 90 min holds for the diagnosis of small bacterial overgrowth in the small intestine [201]. For methane detection in exhaled human breath related to metabolic disorders and diseases, a sensitivity of 5 - 100 ppm is required. Therefore, adequate concentration series of 3 sequential measurements for 0, 5, 10, 20, and 50 ppm of H_2 and CH_4 were performed simultaneously. Two successive measurements for H_2 in the low wavenumber region < 1000 cm^{-1} and for CH_4 in the high wavenumber region > 2500 cm^{-1} with a total acquisition time of 10 s were performed for every measurement point, since the 600 lines/mm grating provides only a spectral range of ~ 900 cm^{-1} (at 660 nm). It has to be highlighted, that between each measurement step, the total volume of the tubing, fiber adapter assemblies, and the HC-PCF was flushed with pure argon, i.e. 0 ppm of methane and hydrogen.
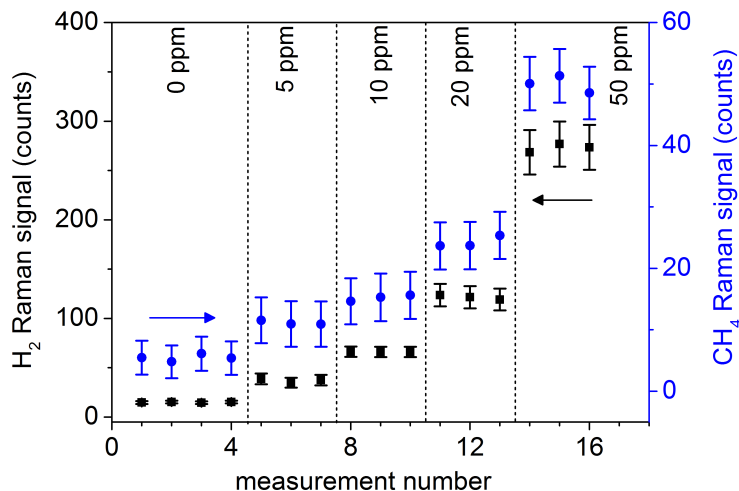

Figure 6.6: Simulation of fiber enhanced Raman spectroscopic monitoring of typical concentrations in a hydrogen breath test. The values of the Raman intensities were corrected for the background values of 0 ppm H_2 (15 counts) and 0 ppm CH_4 (6 counts) respectively. Stepwise monitoring of the Raman signal for H_2 and CH_4 concentrations of 0, 5, 10, 20, and 50 ppm followed. (0.2 W laser power at 660 nm excitation wavelength, 1.5 m "HC-633-02" HC-PCF, 600 lines/mm grating, 10 s acquisition time, $p_{abs} = 6$ bar, and $T = 21\,°C$.)

A minimal Raman background noise of 15.1 (5.4) counts with an average standard deviation of 1.5 (2.7) counts and a total precision of 0.4 (0.5) counts for molecular hydrogen (methane) were measured. The experimentally obtained values for the standard deviation of the peak noise σ_{stat}, SNR, and precision σ_{stat}/I_{mean} are summarized in Tab. 6.4. The noise-equivalent LOD can be determined to $LOD_{5\,ppm} = 3/7 \cdot 5$ ppm $= 2.1$ ppm for hydrogen in this experiment.

Although the relative Raman scattering cross section for CH_4 compared to rotational

H$_2$ concentration (ppm)	σ_stat (counts)	$\sigma_\text{stat}/I_\text{mean}$ (abs. %)	SNR
5	1.6	4.3	7
10	1.2	1.8	9
20	1.8	1.5	11
50	5.2	2.2	12

Table 6.4: Fiber-based Raman spectroscopic SNR and precision for different concentrations of molecular hydrogen: The precision $\sigma_\text{stat}/I_\text{mean}$ was determined by the integrated Raman peak signal I_mean and statistical noise σ_stat for a hydrogen concentration of 5, 10, 20, and 50 ppm in a multi-component gas mixture.

H$_2$ was 3.1 times larger in combination with a quasi parasitic-free signal background in the high wavenumber region, a significantly higher fiber attenuation at 2917 cm^{-1} led to an overall 1.5× lower SNR for methane (cf. Fig. 6.6). This allows the detection of low CH$_4$ concentration levels to be utilized as an indicator for lactose intolerance, due to the conversion of H$_2$ into CH$_4$ by the large bowel bacterium *Methanobrevibacter smithii* [19]. It has to be stated, that the FERS-based sensor method can demonstrate the detection of a H$_2$ concentration change of 20 ppm for HBT and an increase of more than 12 ppm of hydrogen as an indicator for bacterial overgrowth in the small intestine (Fig. 6.6). Additionally, a cut-off value of 20 ppm methane above the basal concentration had been simulated as a potential indicator for lactose intolerance, fructose malabsorption, and bacterial overgrowth syndrome (Fig. 6.6).

A novel methodology for early-stage, non-invasive, point-of-care breath gas diagnosis of metabolic diseases based on combined rotational and ro-vibrational FERS is introduced by the simultaneous monitoring of H$_2$ and CH$_4$ within a mixture of the major components N$_2$, O$_2$, ^{12}CO$_2$, and ^{13}CO$_2$ in exhaled breath. Because some patients hold bacteria that only produce methane or a mixture with hydrogen, FERS introduces the simultaneous and fast detection of methane and hydrogen in combination for a more convincing positive HBT. The simultaneous monitoring of H$_2$ and CH$_4$ by FERS as VOC for colonic fermentation of undigested oligosaccharides can improve the correct diagnostic interpretation in terms of human breath analysis [66, 67, 68]. Furthermore, there is much less experience with methane, because its production is much more complex than the production of hydrogen. On this basis, FERS could potentially support investigations in methane-based human breath analysis. Conclusively, compared to other types of hydrogen sensors those based on optical fibers exhibits a number of advantages:

- There is a great miniaturization potential for this fiber-enhanced Raman spectroscopic setup accompanied by high sensitivity and selectivity, as well as portability and versatility, i.e. the usage of a compact spectrometer. Such a portable sensor would be capable of bedside diagnostics of several metabolic diseases or disorders using breath gases and the implementation as hydrogen leak detection sensors for the discrimination of molecular H$_2$ from non-H$_2$ sources, as well as in context of novel hydrogen based energy systems [125, 164].

- Those fiber sensors show no cross-sensitivity for gases like hydrocarbons, H$_2$S, or CO.

- HC-PCF with small sample volume requirements allow for incorporation into compact and robust devices with trace gas detection sensitivities. This rivals the established mass and optical spectroscopy methods in the field of clinical diagnostics using breath analysis.

- There is no risk of gas ignition because the optical detector has no electrical contacts, thus are capable of remote sensing.

Raman-spectroscopic investigation of *Helicobacter pylori* infection Helicobacter pylori is a gram-negative, microaerophilic bacterium, which is found in the stomach and sometimes in other parts of the body [1, 70]. It plays an important role in the detection of peptic ulcer diseases and gastric malignancy [138]. Clinical diagnostics of *H. pylori* is performed by the urea breath test, where *H. pylori* urease present in the stomach decomposes urea into ammonia and ^{13}C-labeled carbon dioxide, collected in special breath bags [111]. In the presence of produced enzymatically urease by large quantities of *H. pylori*, urea will be metabolized to NH_3, $^{12}CO_2$, and $^{13}CO_2$. The sample could be subsequently analyzed by FERS, which would determine the level of NH_3 and $^{13}CO_2$ compared to normal levels before ingestion of labeled urea resulting in an either positive or negative UBT.

The potential for FERS-based breath analysis is shown by the highly sensitive detection of ammonia in combination with $^{13}CO_2$ in the low ppm level. The ammonia concentration for healthy subjects in the range of 0.25 - 2.9 ppm usually differs from a higher level of 3 - 30 ppm for diseased humans. In contrast, simultaneous detection of $^{13}CO_2$ levels in the range of 330 - 440 ppm compared to 500 - 1000 ppm are necessary to separated a negative from a positive UBT [167, 196]. The sensing capability of these high concentration levels for spectrally well-separated isotopic CO_2 by FERS has already been shown in this work (cf. Sec. 4.4).
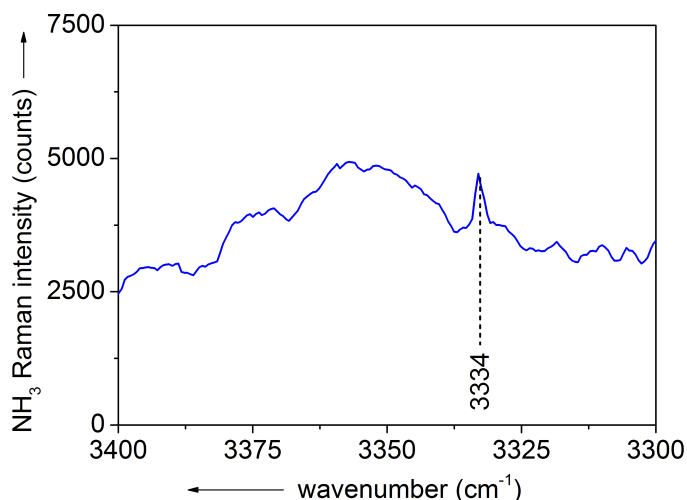

Figure 6.7: Raman spectrum of 10 ppm NH_3 in Ar: The peak height of the symmetric vibration at 3334 cm^{-1} is 927 counts, the standard deviation of the noise was determined to be 137 counts. The noise-equivalent LOD results in a detectable NH_3 concentration of 4.4 ppm (for 0.4 W laser power at 660 nm excitation wavelength, 1.5 m "HC-633-02", 600 lines/mm grating, 30 s acquisition time, $p_{abs} = 10$ bar, and $T = 21\,°C$).

The totally symmetric vibration of ammonia [55] at 3334 cm^{-1} was evaluated by FERS (Fig. 6.7). Molecular NH_3 concentrated at 10 ppm in carrier gas Ar resulted in a peak height of 927 counts with a noise contribution of 137 counts. Thus, a noise-equivalent LOD of 4.4 ppm was achieved. For an adequate differentiation of a negative from a positive ^{13}C-UBT in combination with ammonia detection, further sensitivity scaling is required. The simulation of a positive UBT can be realized by the detection of NH_3 levels over 3 ppm compared to $^{13}CO_2$ levels over 450 ppm, whereas a negative test can be connected to ammonia levels up to 3 ppm and carbon dioxide levels between 300 - 400 ppm. For patient with chronic liver problems (e.g. fatty liver, alcoholic hepatitis), deficiency of essential amino acids (vegetarians), or after a rich meal in protein, the

ammonia level is no longer linear dependent on the specific CO_2 level in the range of 300 - 1000 ppm [74]. An elevated ammonia concentration should be additionally detected within a positive UBT [189, 97, 154]. Insofar the fiber-based Raman spectroscopic NH_3 sensitivity would only be sufficient for a positive UBT connected to higher levels of ammonia in combination with ^{13}C-labeled urea. Lower ammonia concentrations referring to a negative UBT would require an increased sensitivity for FERS-based exhaled breath detection.

Other studies with Raman spectroscopy based on HC-PCF for human breath analysis showing a further SNR improvement for application of lasers and HC-PCF in the NIR compared to the VIS range would be beneficial for clinical diagnostics [35]. The combination of the introduced improved FERS setup together with an operation in the near-IR (i.e. around 800 nm) based on extremely low loss HC-PCF (e.g. "HC-800-02" from NKT Photonics) presents a realistic step to accomplish point-of-care FERS-based clinical diagnosis of *H. pylori* infection in terms of a ^{13}C-UBT.

6.2.3 Detection of ambient air and ultimate LOD

The detection of trace gases is of great interest in numerous areas such as industrial processes, atmospheric chemistry, volcanic activity, agriculture, workplace surveillance, gas certification, and clinical diagnostics [147, 64, 8, 130, 184]. Considering the wide range of application areas for gas sensors, the requirements are manifold and the development and implementation of all in a versatile analytical tool is still challenging. These gas sensors should feature high sensitivity, selectivity, accuracy, precision, a broad dynamic range, no sample preparation, robustness, fast detection, maintenance-free, and should be easy to calibrate. There is no ideal instrument to fulfill all of these requirements. The presented technique of FERS comprises the Raman spectroscopic advantages of being very fast, non-consumptive, label-free, no need for sample preparation, revealing an easy-to-operate two-point calibration with the ability to detect homonuclear diatomic gases like N_2, O_2, and H_2 [82, 79, 102].

In the field of environmental gas sensing, the detection of trace climate relevant atmospheric gases, e.g. CH_4, CO_2, N_2O, N_2, and O_2, is of great importance. The global warming relevant CO_2 has an average ambient concentration of about 360 ppm nowadays, compared to 280 ppm before the industrialization era [17]. An estimated temperature increase of about $2-3\,°C$ will double the natural ambient CO_2 concentrations. Thus, it is very important to quantify unknown CO_2 sources and sinks besides the influences of the well-known gas flux budget contributions. The performance of climatological studies requires a resolution of ambient CO_2 levels in the range of 0.1 ppm with time resolution of 10 s for long-term measurements or $4-10$ ppm for 0.1 s regarding flux measurements [61, 118].

The presented work established a highly sensitive Raman gas sensor, which was characterized in specificity, sensitivity, selectivity, accuracy, and precision. The rapid monitoring of multi-gas fluctuations down to the ppm levels with noise-equivalent LOD in the ppb region was demonstrated. Further characterization was conducted to show a high dynamic range of 7 orders of magnitude in the time range of a few seconds.
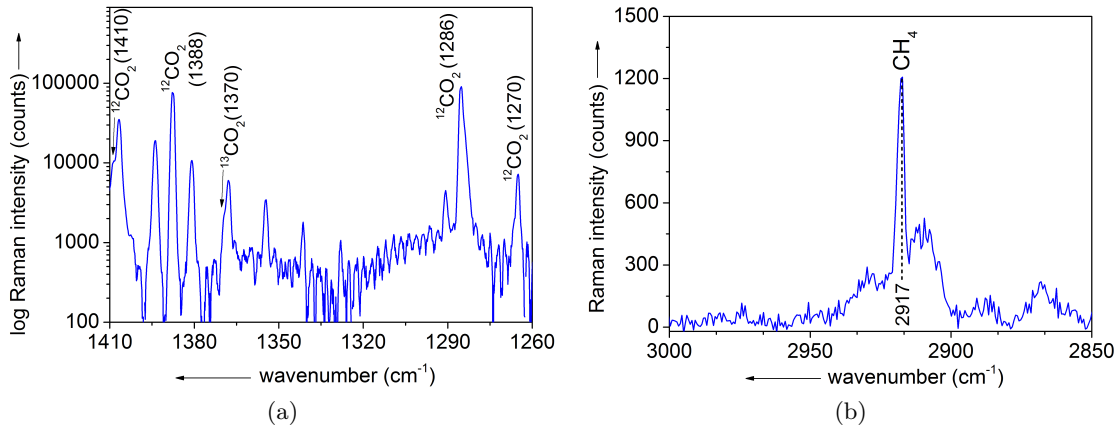
Figure 6.8: Fiber-enhanced ro-vibrational Raman spectrum of (a) ambient CO_2 and (b) ambient CH_4, both in air under ambient conditions. (a): The peak height for $^{13}CO_2$ at 1370 cm^{-1} is 1460 counts, the standard deviation of the noise was determined to be 28 counts. The noise-equivalent LOD equals 1.0 ppm if the peak sum is evaluated. (b): The SNR for the atmospheric CH_4 at ~ 2 ppm is 28 and results in a noise-equivalent LOD of 0.2 ppm. (0.8 W laser power at 660 nm excitation wavelength, 1.5 m long HC-PCF "HC-633-02", 600 lines/mm grating, 40 s acquisition time, $p_{abs} = 1$ bar, and $T = 21\,°C$, respectively)

Ambient air consists to 78.08 vol. % and 20.94 vol. % of the major components N_2 and O_2, next to the minor components $^{12}CO_2$, $^{13}CO_2$, and CH_4 in the ppm region with 380 ppm, 3.8 ppm, and 1.8 ppm per volume, respectively. In order to study the potential of the improved FERS setup to reach the sensitivity compared to the already presented requirements, a spectrum of ambient air under ambient conditions at $p_{abs} = 1$ bar and $T = 21\,°C$ was acquired with respect to the naturally low concentrated molecular gas components $^{13}CO_2$ and CH_4 (Fig. 6.8). It is nicely demonstrated, that the highest band of the Fermi diad at 1370 cm^{-1} for $^{13}CO_2$ is included in the rotational fine structure of the natural concentrated $^{12}CO_2$ (Fig. 6.8a). Convolution and integration of the isotopic $^{13}CO_2$ band led to a peak sum of 1460 counts with a peak noise (SD) of 125 counts. Referring to an ambient concentration of 3.8 ppm in air, it concludes a noise-equivalent LOD of 1.0 ppm for SNR = 3. Further detection of naturally concentrated methane in ambient air revealed a SNR of 28 and a noise-equivalent LOD of 0.2 ppm (Fig. 6.8b). Note that the detection of tracers on a high background of other major components without any cross sensitivity is one major advance of the presented fiber-enhanced Raman multi-gas spectrometric technique. Tab. 6.5 summarizes the hitherto achieved noise-equivalent LOD for important gas compounds, which have been investigated throughout this work. The sensor sensitivity in the sub-ppm region will introduce FERS to new application areas demanding high specificity combined with the stated sensitivity levels.

gas component	Raman shift (cm^{-1})	relative Raman scattering cross section*	noise-equivalent LOD (ppm)
H_2	587	1.66	0.3
CO_2	1388	1.43	1.0
O_2	1556	1.22	1.1
N_2O	2224	0.51	3.0
N_2	2331	1.0	1.2
C_4H_{10}	2880	8.4	1.7
C_3H_8	2908	19.6	7.5
C_2H_6	2914	8.6	1.1
CH_4	2917	8.6	0.2
NH_3	3334	5.0	4.4

Table 6.5: Overview of Raman shifts, relative Raman scattering cross sections [55, 165, 166, 50] (*: normalized to that of nitrogen at 532 nm excitation wavelength), and achieved sensitivities (LOD) for a gas composition detection by FERS after DIN 32456.

6.3 Further sensitivity scaling

Most of these gaseous biomarkers and their characteristic concentration differences between healthy and diseased patients in exhaled human breath are present in the concentration span of ppm to ppb or even ppt. For instance, concentration differences of isoprene (C_5H_8) connected to lung cancer patients were observed in the range of 50 ppb within exhaled breath [90]. The very intense Raman band of isoprene at 1638 cm^{-1} originates from the relative differential Raman scattering cross section of 50.51 compared to nitrogen at 488 nm excitation wavelength [188]. This value is almost one order of magnitude higher than that of methane and would theoretically result in a higher sensitivity to the same amount. Nevertheless, there are several other possible improvements to further increase the sensitivity of FERS for the possible detection of VOC in the ppb region such as:

1. Specific and unspecific analyte preconcentration: Gas sample enrichment by so-called thermal desorption tubes are commonly used for gas chromatography to further increase the SNR [195]. The gas sample will be preconcentrated and natural concentrations far below the specified LOD of the gas sensor system would be identified.

2. Laser output power: The higher the number of photons per fiber area (expressed in intensity with unit $W \cdot cm^{-2}$) and length, the higher the number of successful Raman scattering photons involved in the Stokes shift would be. Assuming an excellent beam quality (i.e. $M^2 \cong 1.0$) in combination with coupled laser powers of tens of W from compact cw-DPSS lasers would dramatically increase the precision for the same acquisition time, or consequently allow shorter acquisition times at the same precision level. Although the silica Raman signal would tremendously increase, the improved spatial pinhole function showed to be extremely efficient to cut out this additional parasitic Raman signal background. Conclusively, the Raman signal enhancement would be higher than a further increase in Raman spectroscopic noise contributions by fused silica.

3. Optimum length and fiber end-facet mirror: Depending on the fiber attenuation

characteristics, there exists an optimum fiber length for forward Raman scattering in HC-PCF (cf. Sec. 3.5). Signal collection for backward and forward scattering can be combined with the help of a highly reflecting mirror for the spectral fiber transmission window at the fiber distal-end in the backward scattering arrangement. This optical mirror combing the signal collection of forward and backward Raman scattering could theoretically increase the signal efficiency up to the factor of 1.6 compared to conventional backward Raman scattering arrangements [4].

4. NIR region ($\sim$ 800 nm): HC-PCF designed with an optical transmission window in the NIR-region can provide much lower signal attenuation than those for the VIS range, with e.g. 0.25 dB/m for a "HC-800-02" fiber at 820 nm design wavelength compared to 1.0 dB/m for the used HC-PCF "HC-580-02". This would result in longer effective fiber lengths up to 5 m for these HC-PCF providing larger interaction lengths for the gaseous analyte and the low-attenuated laser light. In combination with a highly quantum-efficient spectrometer for the IR region, a high power laser at 785 nm, and IR-high reflective optical components, the SNR can be increased at least one order of magnitude for the specific HC-PCF "HC-800-02"[3] from NKT Photonics [35].

---

[3] Albeit, there are more HC-PCF with lower losses available designed for the higher (N)IR region (e.g. "HC-1060" with losses of $<$ 0.1 dB/m at 1060 nm), poor spectrometer quantum efficiencies, the etaloning effect of back-illuminated spectrometer CCD detectors or the application of expensive IR detectors would bring the fiber advantages to naught.

7 Enhanced Raman spectrometric online investigation of plant metabolic activity

The previous chapters have shown that the novel FERS technique provides a manifold of advantages compared to other types of state-of-the-art gas sensors. This approach possesses a high dynamic range with fast response times of several seconds, which will pave the way for fast, non-invasive, and painless point-of-care diagnosis of metabolic diseases in exhaled human breath. Furthermore, the developed FERS sensor provides great potential for miniaturization. This plays an important role in mobile and portable in-situ gas analysis for deeper insights into plant ecophysiology e.g. that greater drought tolerance in tree species might be linked to its greater flexibility in substrate use for respiration. The simultaneous measurement of O_2 and CO_2 for plants has been difficult in practice due to the relatively small O_2 concentration changes in ambient air. Insights in cellular respiration, which can be fueled with carbohydrates, lipids, or proteins, are gained by the on-site detection of the CO_2 production to O_2 uptake relation.

Nevertheless, the previously presented laboratory-based FERS setup lacks miniaturization so far, but could be overcome by the utilization of the available miniaturized mobile Raman setup, which was already investigated and presented thoroughly by Robert Keiner in [100]. The technique of cavity-enhanced Raman multi-gas spectrometry (CERS) fulfilled the requirements to be a calibration- and maintenance-free, fully-automatized O_2/CO_2 respiration rate monitoring system with long-term stability for weeks [101, 102, 103]. Moreover, CERS will be proven as a powerful and non-consumptive analytical technique for precise real-time monitoring of respiration rates and respiratory quotients for the investigation of plant metabolism under stress conditions like drought and shading in this chapter.

7.1 Significance of environmental multi-compound gas sensing

There is a general demand on mobile, robust, cost-efficient, and miniaturized gas sensors for on-site environmental research and biophotonics. Applications for relevant gases like N_2, O_2, CO_2, CH_4, H_2, and N_2O in terms of simultaneous multi-compound gas detection include isotope quantification, biogas analysis, and environmental gas monitoring [155, 126]. Molecular O_2 plays an important role in the process of plant photosynthesis or aerobic bio processes [54]. Molecular CO_2 is the major expired product in processes like respiration [200]. Stable isotopes like ^{13}C in $^{13}CO_2$ are often used for inexpensive isotope labeling measurements, which are a powerful tool to trace carbon fluxes within plants [102, 103].

Conventional O_2 sensors are either based on paramagnetic, electrochemical (i.e. galvanic), or optical (photoluminescence or fiber-based) techniques. Paramagnetic sensors measure O_2 in the range of $0.05 - 100$ vol. % with a response time of less than 1 s. They are commonly used for measurements of cell respiration but successfully applied only in side-stream configurations. Electrochemical sensors, which are mostly used in clinical analysis, show a high sensitivity starting in the ppm range accompanied by low cost, but suffer sensitivity loss from fast aging as consequence of the required high temperature operation. Photoluminescence sensors stand out with response times < 1 s, but lack adequate long-term stability, precision, and accuracy for plant physiological analysis.

Carbon dioxide is generally measured by electrochemical, photoacoustic, infrared absorption spectroscopy (IRAS), or by non-dispersive infrared (NDIR) absorption spectroscopy. Photoacoustic CO_2 sensors are low cost, easy-to-operate, but influenced by thermal drift and insensitive for homonuclear gas molecules (O_2, N_2). Additionally, NDIR sensors require calibration with a zero gas (e.g. N_2). A widely distributed technique for multi-gas detection is gas chromatography often in combination with mass spectrometry (GC-MS). It features a very high accuracy down to the ppt region for multi-gas detection, however with a high response time of several seconds to minutes. These methods are analyte-consumptive and require frequent calibration.

Physiological mechanisms like respiration and cellular osmoregulation are related to the carbon availability in plants [168]. The latter can be substantially affected by induced drought. A consequent stomatal closure will reduce carbon assimilation and may result in allocation and depletion of stored carbon reserves in trees, known as carbon starvation for longer drought periods [128]. Plants can store carbon in form of lipids and proteins, which can be mobilized and used for dark respiration. Studies on respiration, which address a compound metabolism of proteins and lipids besides that of pure carbohydrates, are scarce in plant science [182, 160, 18, 45]. The reduction of carbon allocation through experimentally induced shading for single leaves (i.e. needles) and roots uncovered a compound shift from carbohydrates to lipids and proteins (or a mixture) for dark respiration. Evidence especially for stressed trees with a whole plant approach is absent and restricted to precise gas sensors, which can detect minor concentration changes in respiratory O_2 and CO_2 for stressed plants [26].

The respiratory quotient (RQ: consumed CO_2 divided by produced O_2) indicates respiration dynamics and metabolite use [89, 180]. The release of biochemical energy by metabolization of nutritional compounds, which will be fueled with carbohydrates, proteins, and lipids, can be identified by elucidating the RQ. Monitoring of the RQ can reveal a shift in metabolite use due to different stoichiometric ratios of C:O:H for carbohydrates, proteins, and lipids. These major fuel substrates differ in the amount of O_2 for compound oxidation relative to released CO_2. Carbohydrates feature a RQ value of ~ 1.0 compared to 0.82 and 0.7 for proteins (amino acids) and lipids (fatty acids), since the molar ratio of the combustion is < 1, i.e. less O_2 is required for breakdown. In other words, lipids consist stoichoimetrically of less O (relative to C and H) and require more external oxygen for fatty acid oxidization compared to proteins and carbohydrates [41].

So far, RQ measurements based on compound shift were performed only on excised tissues for short-term treatments on affected plants [182]. The determination of RQ for qualitative plant respiration turned out to be practically difficult to measure, primarily due to small O_2 concentration changes relative to the content in ambient air (~ 21 vol. %) compared to ambient CO_2 at 360 ppm. An increase (decrease) of e.g. 200 ppm from absolute 260 ppm (absolute 21 000 ppm) in concentration for CO_2 (O_2) at ambient conditions would lead to a relative difference of 55 % (0.01 %). Lower aerobic activities compared to humans and animals, certain species variance, and great diversity of organs (roots, stems, leaves/needles, etc.) in plants further result in varying respirational activity in terms of respiration rates (RR) and RQ [182]. Commercially available sensors for the detection of O_2 and CO_2 are not suitable for RQ monitoring in plant science. Hence, they suffer from one or more of several basic problems: (1) insufficient precision with low specificity, (2) no continuous measurements with high response time < 1 s, (3) consumption of sample gas, (4) operation only under high oxygen atmosphere, (5) need for frequent calibration due to fast sensor aging, (6) no simultaneous measurement of O_2 and CO_2, and (7) no miniaturization for online in-situ monitoring. Continuous monitoring of O_2 and CO_2 respiration rates and online in-situ analysis of RQ values should ideally be performed with a miniaturized and field-portable O_2 and CO_2 combined sensor with high temporal response time, high sensitivity in the ppm range on

a high natural background of O_2 and N_2 and with very good sensor precision, i.e. a relative error of less than 1 %.

7.2 Cavity-enhanced multi-gas Raman spectrometry (CERS)

A novel technique, which overcomes all above mentioned limitations, namely cavity-enhanced multi-gas Raman spectrometry (CERS), will be introduced for the continuous and simultaneous on-site monitoring of respiration fluxes for O_2 and CO_2 in plant sciences. The applied CERS devices was built within a cooperation of Philips Medizin Systeme Böblingen GmbH and Carl Zeiss Jena GmbH. Its technique, its optical design, and its applications are described elaborately in [100] by Robert Keiner.

7.2.1 Optical design

Contrary to the previously described fiber-based Raman spectroscopic technique, the CERS arrangement consists of a power-buildup laser cavity [110, 131] with a length of ~ 5 cm. A schematic setup of the mobile and miniaturized CERS multi-gas sensor is shown in Fig. 7.1.
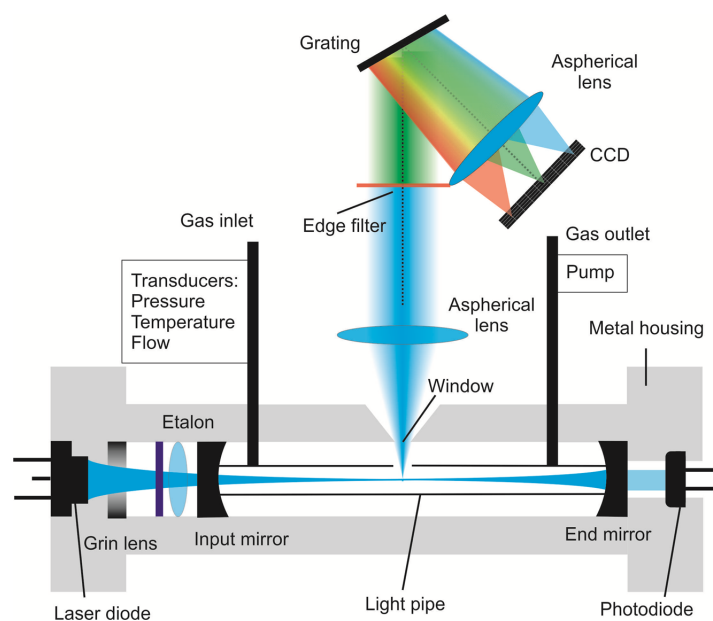

Figure 7.1: Schematic setup of the CERS gas sensor: The blue beam illustrates the resonator mode in the power build-up cavity, the green light the Stokes scattered light transmitted through the edge filter and send to the CCD over a dispersive grating (by Robert Keiner from [100]).

Although both introduced techniques of CERS and FERS are based on the Raman spectroscopic effect, the signal enhancement is accomplished differently. The optical field is amplified by a factor > 1000 inside the miniaturized optical cavity, leading to an intra-cavity power up to 100 W in CERS. Since the Raman signal intensity scales with the laser intensity/power, sensitivities down to 50 ppm can be achieved with CERS [100]. The miniaturized CERS device (Fig. 7.1) features a spectral resolution of 50 cm^{-1} and a spectral specification for the Fermi diad of isotopic-labeled $^{13}CO_2$ next to ambient $^{12}CO_2$ has been successfully demonstrated for isotopic-labeled saplings of *Populus trichocarpa* [102]. This portable laser-cavity gas sensor is less bulky and mobile compared to the lab-based FERS setup. A comparison of both techniques in terms of achievable spectral resolution for some prominent gases is illustrated in Fig. 7.2. FERS demonstrates a clear ro-vibrational spectroscopic structure, e.g. a fine structure with $O-$ and $S-$branch for

nitrogen around 2331 cm^{-1}, which cannot be easily quantified simultaneously by other conventional technique for e.g. monitoring of metabolic pathways.
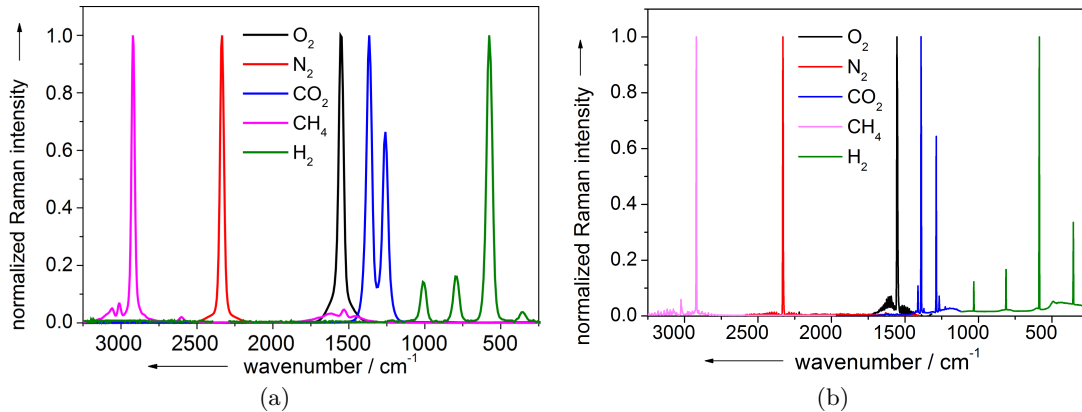

Figure 7.2: Illustrative Raman spectra of some prominent gases achieved by (a) CERS and (b) FERS: The Raman intensity is normalized for better visibility, respectively. Raman spectra of CERS feature a resolution of ~ 50 cm^{-1} at an excitation wavelength of 650 nm, whereas ro-vibrational Raman transitions are highlighted for the FERS measurement with spectral resolutions down to 0.8 cm^{-1} at 532 nm laser excitation wavelength. The CERS-based Raman spectrum was acquired by Robert Keiner and extracted from [100].

The analytical relevance of both methods can be compared by introducing the figure of merit "LOD to laser power, gas pressure, and acquisition time", i.e. "LOD$\cdot P_{\mathrm{L}} \cdot p \cdot \sqrt{t}$". Referring to performed experiments, Tab. 7.1 lists measurement parameters, the individual LOD, and the "LOD$\cdot P_{\mathrm{L}} \cdot p \cdot \sqrt{t}$". The analytical efficiency of CERS is around 25 times higher than that of the FERS approach.

parameter	CERS^a	FERS^b	unit
laser power P_{L}	0.05	0.6	W
pressure p	1	9	bar
measurement time t	0.1	15	s
LOD	16	0.3	ppm
LOD$\cdot P_{\mathrm{L}} \cdot p \cdot \sqrt{t}$	1*	24.8	ppm$\cdot$W$\cdot$bar$\cdot\sqrt{s}$

Table 7.1: Comparison of a demonstrative CERS and FERS measurement with respect to the obtainable LOD: *The LOD was referenced to the laser power P_{L}, pressure p, time $\sqrt{t}$ and normalized to CERS measurement with value 1 for a better comparability. (Smaller values equal a lower normalized LOD, which indicates a better performance.) ^{a} Listed CERS parameters were taken from [100]. ^{b} Listed parameters are extracted from Fig. 6.3.

The relatively lower effective LOD is realized by an extreme optical field enhancement in the gas-filled cavity accompanied by lower laser powers when compared to moderate effective MOF lengths determined by fiber attenuation characteristics. The lab-based FERS approach lacks several features for application in various fields of gas environmental sensing, which are covered by the CERS buildup:

- The CERS gas sensor is extremely stable against mechanical vibrations. This very cost-effective and portable sensor with a high level of miniaturization can be battery-driven for on-site measurements [103].

- The relatively simple calibration of the CERS device accompanied by a straightforward handling allows for more rapid detection in the range of some tens ppm

with a high time-resolution of some tens of ms for i.e. respiration gas flux changes [100].

- The maintenance-free and easy-to-calibrate cavity-based Raman gas analyzer further reveals a long-tern stability over weeks, which makes it highly suitable e.g. for monitoring of the gas exchange in plant respiration [101, 102, 80].

High finesse optical cavities outperform losses of microstructured optical fibers to date [35, 162], although the fiber approach turned out to be more sensitive in many applications carried out in this thesis. Nevertheless, both techniques showed their uniqueness for different applications in the field of plant science and clinical diagnostics, and individually demonstrated their strength. The detection of metabolic disorders or diseases at VOC concentration levels of sub-ppm by terms of human breath analysis is however limited for CERS due to low laser powers and low gas pressures inside the optical cavity.

7.2.2 Raman spectroscopic gas analysis

Due to the high level of miniaturization and on-site compatibility of the cavity-based Raman gas sensor, the online investigation of gas concentrations, corresponding gas exchange rates, and respiratory quotients in different tree species under stress-induced treatments was carried out by CERS rather than FERS. The calibration for the multi-gas monitoring and the operation principle for multi-gas measurements were described in [100]. All investigated gases, namely O_2, CO_2, and N_2, could be specifically identified and independently quantified (Fig. 7.3b).
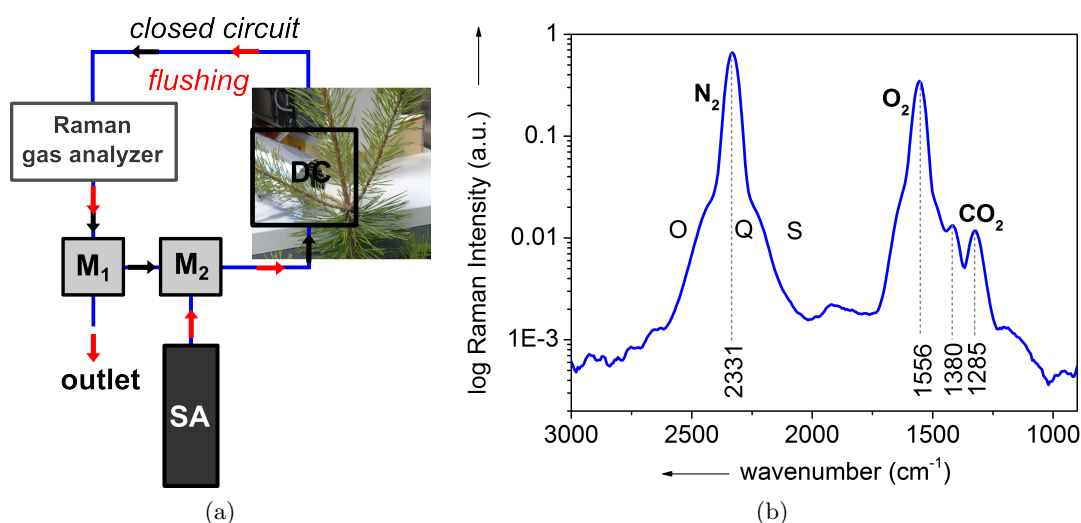

Figure 7.3: (a): Schematic setup of the Raman gas analysis experiment for RQ measurements: The Raman gas analyzer was connected to a dark chamber for the branch under investigation. The setup enables two modes: (1) Continuous flushing (red arrows) of the whole setup by CO_2-free synthetic air (SA) or (2) closed circuit mode for the continuous gas monitoring of the branch respiration (black arrows). It could be switched automatically between both modes via two magnetic valves (M_1, M_2). The gas composition for the closed circuit mode was neither consumed nor changed by the Raman gas analyzer. (b): Exemplary Raman spectrum from a dark respiration experiment with the vibrational bands of N_2, O_2, and the CO_2 Fermi diad for 650 nm laser excitation wavelength. The weakly resolved $O-$, $Q-$ and $S-$branches are indicated for molecular nitrogen in the Raman spectrum.

The inlet of the CERS sensor was connected to a specially designed dark respiration chamber (DC, Fig. 7.3a), which contained a single branch. Dark respiration by complete darkness, i.e. the absence of photosynthetic activity, was ensured by covering the airtight

Lucite® chamber together with two layers of aluminum foil. Only the dark chamber contributed to respirational changes in O_2 and CO_2 concentrations during the time of investigation. The outlet of the Raman gas analyzer was connected to two 3-way software-controlled magnetic valves (M_1 and M_2, Fig. 7.3a), which were placed in series. The magnetic valve M_2 realized the flushing process of the multi-gas mixture after a single measurement cycle to the atmosphere. M_1 realized flushing of the total cycle volume with synthetic air (SA: 80 vol. % N_2, 20 vol. % O_2, Fig. 7.3a) before an individual cycle start. Opening and closing of the magnetic valves was included in the spectrometer software (LabVIEW). The closed system was realized with both valves closed, and the air could circulate continuously through the system, the dark respiration chamber, and the sensor cavity driven by the Raman gas analyzer membrane pump. The initial CO_2-free air accumulated by respired CO_2, while the O_2 concentration of initial $\sim$ 20 vol. % was consumed and decreased during closed cycle mode. After the accumulating CO_2 concentration reached a predefined threshold (e.g. 3000 ppm in Fig. 7.4), both valves were switched to open, which resulted in flushing of the total cycle volume (dark chamber, tubing, magnetic valves, and Raman gas sensor) with synthetic air and thus replacing the previous gas mixture for a new measurement cycle. After some minutes, the valves automatically switched to closed cycle mode and a new measurement cycle started. One cycle time lasted $0.5 - 1$ h (Fig. 7.4).

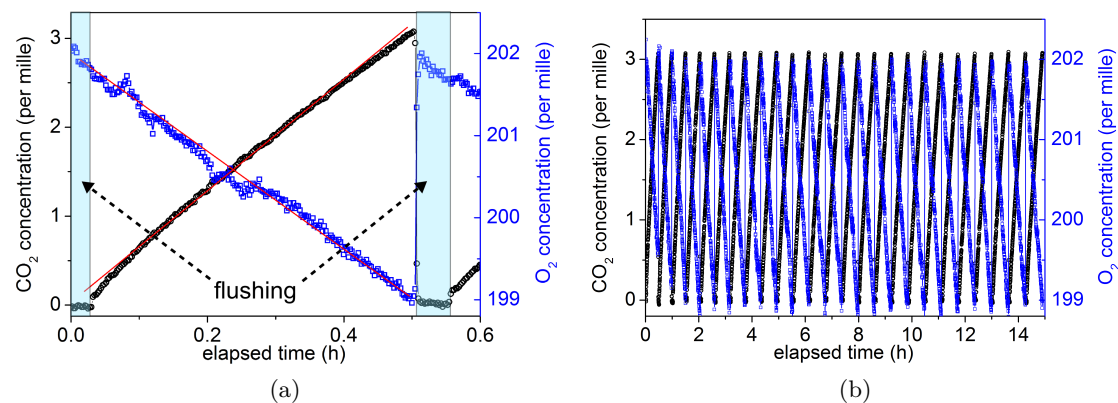### 7.2.3 Measurements of respiration rates and respiratory quotient

Figure 7.4: Example of CERS-based monitoring of branch dark respiration rates for untreated pine. (a): Detail of a single cycle with flushing period before the initiation of a closed circuit cycle and after it reached the experimentally defined upper CO_2 limit of 3000 ppm (3 vol. ‰) for a total cycle time of approx. 0.5 h. The total volume was flushed with synthetic air (80 vol. % N_2, 20 vol. % O_2) each time for 2 min (light blue). For the closed circuit mode, a linear decrease from initial 20 vol. % of O_2 (blue) and a linear increase from initial 0 ppm CO_2 (black) resulted. The small CO_2 offset of 300 ppm (black) was the result of unchanged air inside the magnetic valve tubing. The individual concentration changes were fitted linearly (red lines) for the determination of CO_2 and O_2 respiration rates. (b): The graph shows 25 subsequent dark respiration cycles for an overall elapsed time of 15 h and the upper CO_2 limit of 3000 ppm. 25 RR for O_2 and CO_2 and thus 25 RQ values could be obtained.

The measured cycle time was dependent on two factors: (1) the total volume of the whole closed circuit and (2) the respiration activity (and its decline under stress) of the current branch under investigation. The dead volume of the closed cycle resulted in $\sim$ 50 ml for the drought and $\sim$ 60 ml for the shading experiments. The dead volume of the whole cycle was determined by the following steps: (1) An overpressure (several mbar) for the closed cycle was applied via a gas syringe with 5 ml volume. (2) According to the ideal gas law, the volume was determined by the known total pressure and the

pressure difference for the defined syringe volume. Respiration rates for the investigated tree species and treatments showed to be very different referring to the initial values and the decline as a consequence of the individual treatment, the tree species, and the different branch biomass. In order to obtain constant cycle for continuously declining respiration activity over several days, the CO_2 limit was reduced from initially 7000 ppm to 3000 ppm throughout the treatment.

The measured respiration rates in per mille h^{-1} can be converted in µmol m^{-2} s^{-1} with the help of the total cycle volume and the sample surface area in m^2. After each treatment, the surface area was determined with a LI-3100C® area meter (LI-COR, USA) and a standard deviation of 1.5 % for needles and 0.4 % for branches. The relative slopes of the concentration changes for O_2 and CO_2 were used for the calculation. The linear fit of both revealed the RQ defined by $\Delta c(CO_2)/ - \Delta c(O_2)$. After the cycle flushing procedure, a small dead volume for the magnetic valve connections remained. The immediate distribution of this small CO_2 concentration in synthetic air resulted in a step-like increase in CO_2 concentration, exemplary 150 ppm in Fig. 7.4a during the first 3 min (Fig. 7.4). Concentration changes within this time were not considered for the determination of RR by the linear fit procedure. This fitting process in Fig. 7.4b resulted in a slope of (-6.12 ± 0.05) per mille h^{-1} for O_2 and (6.06 ± 0.02) per mille h^{-1} for CO_2. The RQ could be determined to 0.99 ± 0.02 for 25 overall dark respiration cycles within a total time of 15 h. The Raman gas analyzer defined the precision of 1 % for the determination of individual gas concentration changes [101, 102]. The concentration error (standard deviation) is smaller for molecular CO_2 due to a smaller peak area compared to O_2 with a generally higher concentration of $\sim$ 20 vol. %. The error for the individual RR increased to a value of 1.5 % as a consequence of the decline in respiration activity for treatment periods up to 11 days.

On the one hand, RR were monitored instantaneously to highlight the general exponential trend over time and rapid alteration like respirational day-night cycles. On the other hand, averaged RR are reported to emphasize the temporal dynamics during the treatment period. Hence, an error (standard deviation) of ± 0.07 was introduced for the mean RQ values. Averaging for the time of treatment start and end resulted in a smaller error of ± 0.03.

The direct monitoring of RQ, i.e. O_2 and CO_2 concentration changes, have been so far realized by the combination of an IR gas analyzer (CO_2) and oxygen electrode (O_2) in literature [182]. RQ data was averaged every day and the standard deviation and precision was not stated. For another publication, the CO_2 production and the O_2 consumption were measured simultaneously in excised leaves with an IR CO_2 sensor (UMS GmbH, München, Germany) and a ZrO_2 oxygen sensor [65]. One RQ measurement took approx. $10 - 15$ min per sample and the resulting significance level p was 0.14 - 0.67 for $n = 12$ [65]. So far, no studies based on a comparable sensor for both gas compounds O_2 and CO_2 together with a high time resolution, i.e. resolved respiration day-night-cycles like in Fig. 7.5a and 7.5c, have been published. Especially CRDS devices used within literature cannot measure diatomic O_2, are less miniaturized, and feature a large tubing volume (i.e. additional dead volume) of approx. $60 - 80$ ml.

7.3 Investigation on pine and spruce metabolism under drought and shading

The investigation of compound changes for respiration during two individual treatments of drought and shading accompanied by a declining RQ value in two different European forest tree species, namely *Pinus sylvestris* [L.] (Scots pine) and drought-intolerant *Picea abies* [L. H. Karst] (Norway spruce) will be presented in this chapter.

7.3.1 Biological material and preliminary examination

Five year old trees of Scots pine and Norway spruce with a height of ~ 60 cm were purchased at a local forest nursery. Two liter pots containing carbon-free 2:1 vermiculate:sand mixture were used for the trees (fertilized with Manna® Wuxal Super 8-8-6 with micro elements and a slow-release conifer fertilizer Substral® Osmocote 11-8-17; Wilhlem Haug GmbH & Co. KG and Scotts Celaflor GmbH).

One tree was investigated for each treatment and each species. Each treatment was repeatedly started 3 times for an untreated tree. The leaf area varied between $21-25\,\text{cm}^2$ and $22-37$ cm^2, respectively, for pine and spruce. Since a preliminary study revealed drought-related changes in tree functioning within one week under complete drought (i.e. decrease in photosynthetic rate and stomatal conductance), the irrigation was avoided completely for this drought treatment. Drought treatments were continued beyond initial RQ changes until the RQ stabilized, but stopped before a drought-induced mortality occurred in an air-conditioned laboratory at a temperature ranging between $25-27\,°\text{C}$. The shaded trees were placed into a dark incubator (IPC 7000, Memmert GmbH), which regulated a constant temperature of 25 °C and a temperature accuracy of ± 0.1 °C. The relative humidity and temperature within the incubator were logged by a humidity-temperature logger (Testo 177-H1, Testo GmbH).

Reproducibility and accuracy of the CERS-based monitoring of respiratory concentration changes were tested by measuring branches of control pine trees ($N = 4$) over a period of 8 weeks. These trees were watered and experienced a natural day-and-night cycle without any treatment. The respiration rates over this period were $(1.26 \pm 0.06)\,\text{µmol}\,\text{m}^{-2}\,\text{s}^{-1}$ and (-1.29 ± 0.08) µmol m^{-2} s^{-1} for O_2 and CO_2, which resulted in a RQ value of 0.98 ± 0.02. This is in agreement with the carbohydrate-dominated combustion of mainly starch, sucrose, glucose, fructose, and inositol [180]. The standard deviation of ± 0.02 for the RQ mainly originated from the natural species variation and the precision of the Raman gas sensor.

Afterwards, stress treatments of shading and drought were applied. The initial RQ values close to 1.00 ± 0.03 for both species indicated pure carbohydrate metabolism before the individual treatment was initiated.

7.3.2 CERS investigations of pine and spruce

Pine

The initial respiration rates of O_2 and CO_2 dropped from ~ 0.8 µmol m^{-2} s^{-1} to $\sim 0.4\,\text{µmol}\,\text{m}^{-2}\,\text{s}^{-1}$ within the first 2 days after treatment begin (Fig. 7.5a, 7.5c). The initial decrease for shaded pine, however, stopped already within the first day. The initial decline in RR with -0.22 µmol m^{-2} s^{-1} d^{-1} (drought) and -0.29 µmol m^{-2} s^{-1} d^{-1} (shading) emphasized the strong down-regulation of respiration activity for treated pine. This trend was accompanied by a slight decrease in RQ of initially 1.00 ± 0.02 to 0.93 ± 0.03 for drought and to 0.97 ± 0.03 for shading treatment (Fig. 7.5b, 7.5d). Compared to the control measurements, the precision of RQ was marginally higher, which may indicate the variation of RQ during stress-regime. In droughted pine, the absolute O_2 respiration rate further decreased to its final value of 0.30 µmol m^{-2} s^{-1} (Fig. 7.5a). Albeit, the associated RQ slightly decreased for another 2 days and then abruptly dropped to its final value of 0.75 ± 0.02 within 2 subsequent days. Afterwards, RR remained constantly for another 5 days until the treatment was stopped (Fig. 7.5b).
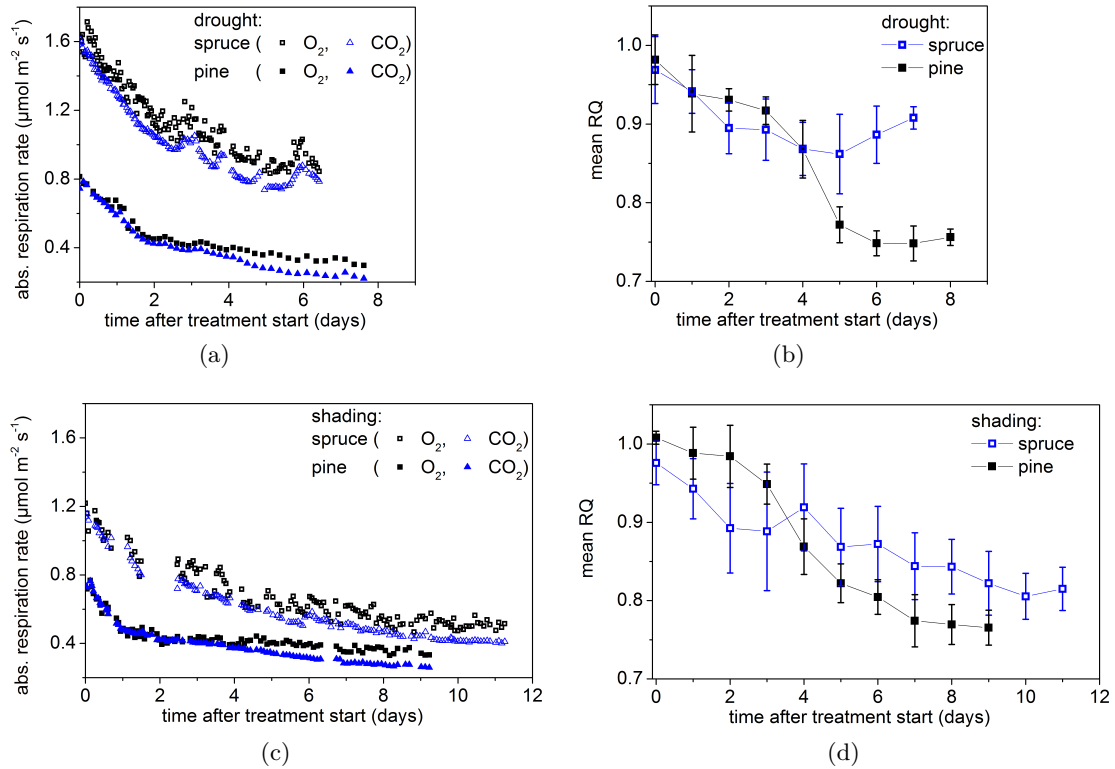
Figure 7.5: Online Raman multi-gas analysis of O_2 and CO_2 during the course of branch dark respiration comparing pine and spruce in terms of absolute respiration rates for (a) drought and (c) shading treatment, which resulted in daily averaged RQ of pine and spruce for the (b) drought and (d) shading treatment.

The RQ value of shaded pine continuously decreased to the value of 0.78 ± 0.02 at day 6 and stayed almost stationary until its final value of 0.77 ± 0.03 at day 9 (Fig. 7.5a). The RR slightly decreased to a final value of 0.33 µmol m^{-2} s^{-1} the following 7 days with an associated change of -0.01 µmol m^{-2} s^{-1} d^{-1} until the shade treatment was stopped for pine (Fig. 7.5c). However, droughted pine switched to a change of -0.03 µmol m^{-2} s^{-1} d^{-1} at day 2, which was kept constant till the treatment end. Although the features in RQ decrease seemed to be different for both treatments, the absolute RQ decline of 0.23 indicated an overall similar behavior (Tab. 7.2). The sigmoidal decrease most likely arose from enzymatic saturation in these tress (Tab. 7.2) [116].

Spruce

The overall higher initial respiration rates for spruce differed from 1.71 µmol m^{-2} s^{-1} to 1.22 µmol m^{-2} s^{-1} for drought to shading treatment (Fig. 7.5a, 7.5c, and Tab. 7.2). The acclimatization time in the laboratory had to be differently applied for shading, i.e. 3 days instead of generally 2 days before a treatment started. The RR for droughted spruce decreased fast within the first 2 days after treatment initiation and slowed down for the following 3 days to a value of 0.84 µmol m^{-2} s^{-1} (Fig. 7.5a). RR stayed almost constant for the final 2 days till treatment stopped. The RR for shaded spruce decreased to a value of 0.82 µmol m^{-2} s^{-1} during the first 1.5 days (Fig. 7.5c). The continuous decline in RR slowed down to a value of 0.61 µmol m^{-2} s^{-1} within the next 4 days and further on to the final value of 0.50 µmol m^{-2} s^{-1} after 11 days (Fig. 7.5c). Similar values of 0.87 µmol m^{-2} s^{-1} (drought) and 0.77 µmol m^{-2} s^{-1} (shading) for both treatments were observed, but differed in treatment duration. These respiratory dynamics are reflected in the alteration of RQ values in both treatments. For droughted

spruce, the initial RQ value of 1.00 ± 0.02 rapidly decreased to 0.90 ± 0.04 within the first 4 days and further remained at this level for the next 5 days until treatment ended (Fig. 7.5b). For shaded spruce, the lower initial RQ value of 0.97 ± 0.03 rapidly diminished to 0.89 ± 0.05 for the first 2 days (Fig. 7.5d). Afterwards, the RQ slowly declined at a constant rate to its final value of 0.81 ± 0.03 after 11 days of shade treatment. Droughted spruce showed a similar initial decline of -0.22 µmol m^{-2} s^{-1} d^{-1} to pine within the first 3 days. Afterwards, this decline was halved to -0.11 µmol m^{-2} s^{-1} d^{-1} and remained on this generally high level (Fig. 7.5a). Contrary to droughted spruce, the initial decline rate of -0.10 µmol m^{-2} s^{-1} d^{-1} in shaded spruce for the first 4.5 days slowed down to -0.02 µmol m^{-2} s^{-1} d^{-1} for the remaining period of the shading treatment (Fig. 7.5c). This may be an indicator for the mobilization and utilization of stored carbon substrate pools. In summary, the RR declined in the first $1 - 2$ days to $50 - 70$ % compared to the initial values with a continuous slighter decrease until the end of these different treatments. All data are summarized in Tab. 7.2.

species,	RR (µmol m^{-2} s^{-1})		RR	RQ (SD)		RQ diff.
treatment	start	end	diff.	start	end	
pine, drought	-0.81	-0.30	0.51	0.98 (0.03)	0.75 (0.02)	-0.23
pine, shading	-0.77	-0.33	0.44	1.00 (0.02)	0.77 (0.03)	-0.23
spruce, drought	-1.71	-0.84	0.87	1.00 (0.02)	0.90 (0.02)	-0.10
spruce, shading	-1.22	-0.50	0.77	0.97 (0.03)	0.81 (0.03)	-0.16

Table 7.2: Respiration rates (RR) for O_2, respiratory quotients (RQ), and standard deviation (SD) for pine and spruce exposed to drought and shading treatment are compared for the start and end of the treatment (i.e. difference in RR and RQ).

Remarkably, respiration rates in droughted spruce showed a distinct day-night-cycle characterized by higher rates during daytime compared to nighttime (Fig. 7.5a). This may be the consequence of two facts: (1) changes in day-night temperature and (2) frequent changes in light illumination during the whole treatment. Whereas (1) affects the whole tree, (2) only takes influence on the rest of the tree excluding the chambered branch. The largest respiration rate differences in the day-night-cycle occurred between $24 - 26$ h after the treatment start. These changes in the range of $0.078 - 0.090$ µmol m^{-2} s^{-1} could be easily detected by the mobile CERS gas analyzer (Fig. 7.5a). A comparable day-night-cycle with lower fluctuations could be observed as well in droughted pine and shaded spruce (cf. RR of O_2 in Fig. 7.5a, 7.5c).

7.3.3 Analysis of respiration substrates

The determination of concentrations for different substrate pools is described in the Appendix B.1. Carbohydrates as the primary respiration substrate being produced during photosynthesis, usually lead to their storage form starch. It should switch to other metabolites like proteins and lipids during both treatments identified by the observed RQ decline (Fig. 7.6). For both species, starch concentrations depleted under drought, but increased for shading treatments (Fig. 7.6e, 7.6f).

The initial substrate concentrations of water-soluble carbohydrates (WSC) were higher for spruce compared to pine in both treatments (Fig. 7.6a, 7.6b). Final WSC concentrations (in mg/g) for both species balanced each other out in needles and branches (Fig. 7.6c, 7.6d). This may be a consequence of the faster down-regulation in metabolism for pine compared to spruce, indicated by the rapidly decreased RR (cf. Fig. 7.5a, 7.5c). Especially the changes in lipid concentration, corroborated by a steadily RQ decline, may indicate a substrate metabolism shift to lipids (Fig. 7.6e, 7.6f). It seems, that after

a general sudden decrease of photosynthates, a stronger remobilization of stored lipid compounds occurred due to a lower level of dehydration in shaded spruce compared to droughted spruce (Fig. 7.6). In drought-tolerant pine, carbon starvation as the primary effect of stress-induced carbon limitation showed only a moderate compound translocation of lipids compared to spruce for both treatments (Fig. 7.6e). Any pools were fully depleted, neither by the drought nor by the shading treatment. This was probably a result of the very fast down-regulation of metabolic activity after treatment start in combination with relatively short treatment durations of maximum 11 days (Fig. 7.5a, 7.5c, and Tab. 7.2).
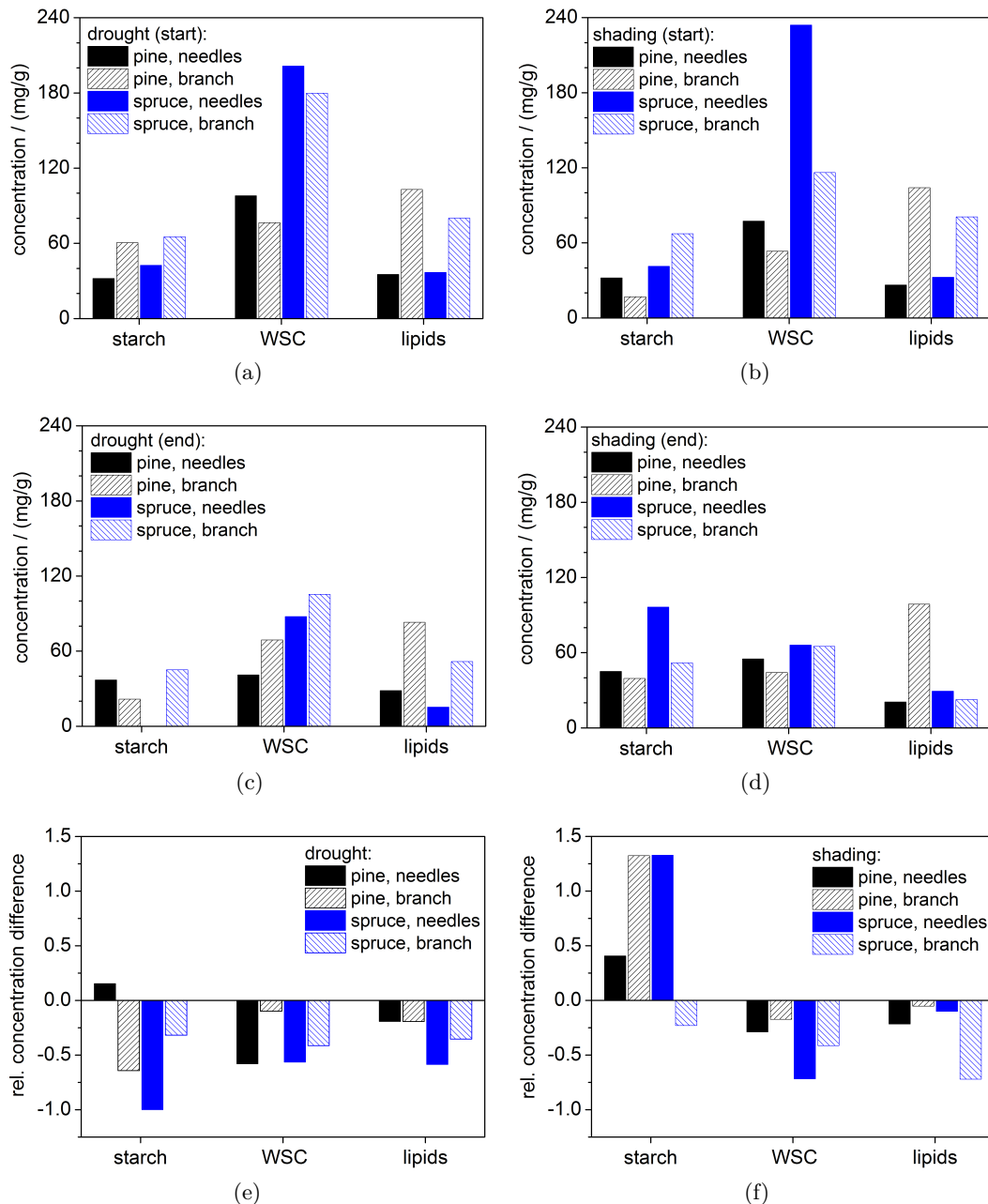
Figure 7.6: Absolute concentrations (a – d) and relative differences (e, f) in respiration substrate between start (a, c) and end (b, d) of drought and shading for starch, water-soluble carbohydrates (WSC: glucose, fructose, sucrose, and inositol), and lipids in needles and branches of pine and spruce, respectively [80]. (N = 1)

7.3.4 Conformity of gas exchange rates and putative respiration substrates

The initial decline in respiration activity for both species could be attributed to a sudden decrease in primary respiration substrates due to stomatal closure [58] or shading [168]. The continuous strongly pronounced decline in RR may be connected to a hindrance of storage remobilization and translocation via hydration [84]. Different results for shading treatment are supporting this thesis, although concentrations of substrates like carbohydrates did not clearly indicate continuous mobilization. The previous results of pine emphasize the ability of mobilization and utilization of stored carbon compounds more readily than for spruce in both treatments. A photosynthates shift from carbohydrates, i.e. sugars, to lipids and proteins have so far only been proven under sugar starvation [18, 63]. Sugars are not only substrates in carbon metabolism, but act also enzymatically for lipid and protein catabolism [112]. Decreasing substrate pools for carbohydrates will most likely lead to an allocation and mobilization of protein and lipid storage. The decreasing RQ for both treatments and both species indicated a generally mixed metabolism, but shifted on a different level from a pure carbohydrate-dominated to a lipid- and protein-dominated metabolism.

The strong down-regulation of catabolic activity in pine could have reduced the utilization of stored carbohydrates to such an amount, that the substrate concentration changes could not be detected in the tree tissues [57]. This could be solved by the stoichiometry of the gas exchange comparing it with substrate pool changes. Unfortunately, the experimental design (Fig. 7.3a) cannot verify the energy balance of the measured branch section, because the import and export carbon pool measurements from or to other tree parts are not taken into account. Conclusively, simultaneous decrease in RR, RQ, and concentrations of putative respiratory substrates for pine and spruce showed similarities to previous findings under carbon limitation [18, 160]. The more drought-tolerant pine in comparison to spruce may be linked more to its potential for allocation, mobilization, and utilization of respiratory metabolites. Both treatments revealed a sigmoidal decline in respiration rates and associated respiratory quotients down to a value of 0.75 for pine.

7.4 Summary

The investigation of accurate online quantification of RR and RQ in trees exposed to stress-induced treatments was carried out by the utilization of CERS. By this unique technique, it was possible to quantify minor concentration changes of O_2 and CO_2 simultaneously with one gas sensor and monitor in-situ the dark respiration gas exchange of chambered branches for 2 simultaneously applied treatments continuously over periods of up to 21 days. Deeper insights could be elucidated by the application of this novel enhanced Raman spectroscopic technique. In general, such measurements are challenging in plant science due to the high background of ambient O_2 at 21 vol. % next to CO_2 naturally concentrated at 360 ppm in air. CERS outperforms other gas sensing techniques for in-situ online monitoring of O_2 and CO_2 respiration rates during manipulative experiments in plant physiology due to some essential features:

- Enhanced Raman multi-gas monitoring is preferable for the simultaneous real-time analysis for mixtures of many gases, including homonuclear O_2, N_2, and H_2, without altering the gas composition or showing any cross-sensitivities.

- Highly temporal-resolved CERS monitoring of different gas fluxes allows for the rapid detection of physiological responses such as respiratory day-night-cycles, but also more long-term variations over weeks for stress-treated trees.

- The versatile CERS device is cost-effective, very robust, portable owing to its

miniaturization, and is therefore suitable for in-situ gas exchange monitoring for plant respiration with long-term stable operation and no need for maintenance for weeks.

8 Conclusion and Outlook

The main objective of this thesis was to merge conventional Raman spectroscopy, which is based on the intrinsically weak inelastic scattering process, with a novel type of microstructured optical fiber (HC-PCF). The development of such an innovative fiber-based Raman gas sensor would exploit a tremendous signal enhancement by increasing the number of interacting gas molecules with the laser light. Thus, the highly sensitive detection of different multi-component gas mixtures over a wide dynamic range down to VOC concentrations in the ppb-region for non-invasive, point-of-care breath gas analysis of metabolic diseases by human breath analysis and the precise real-time monitoring of biogenic gas fluxes for plant ecophysiological studies should be realized. Furthermore, the application of an innovative design of a miniaturized and extremely robust Raman multi-gas sensor [100], which is based on a very stable power-buildup laser cavity, is applied for profound insights into plant functioning such as the link of more drought-tolerant pine to its greater flexibility in substrate switch for plant respiration under drought and shading.

In the first part, the design and the thorough characterization of an advanced fiber-enhanced Raman spectrometric (FERS) setup was investigated for a fast monitoring of multi-gas concentration fluctuations for required sample volumes in the nL-range. Climate relevant gases such as CH_4, CO_2, and N_2O together with N_2 and O_2 were simultaneously quantified with limits of detection as low as 4 ppm at very short acquisition times. FERS as a potential method for early-stage disease diagnosis was elucidated with the simultaneous quantification of different gas compounds within exhaled human breath such as the major components $^{14}N_2$, $^{16}O_2$, and $^{12}CO_2$, as well as the minor components $^{14}N^{15}N$ and $^{13}CO_2$ naturally concentrated at the low ppm region, in a high dynamic range of 6 orders of magnitude.

The second part demonstrated measurements based on the successful approach to combine the developed lab-based FERS sensor with the already existing fiber-array spectral translator-based Raman imaging setup (by Michael Brückner, IPHT Jena) [16] for the first time. Consequently, Raman signal contributions from the microstructured silica fiber cross section could be spatially mapped and quantified. Additionally, rapidly changing Raman signal variations based on strong fiber bending within the microstructured fiber were carried out by this approach. Compared to wavelength-scanning or mapping-based spatial analysis, this techniques is less time-consumptive and can elucidate spatial Raman signal variations for immediate fiber instabilities. Altogether, this setup showed to be a suitable candidate for investigation of signal distributions radiated by the cross section of novel types of microstructured fibers.

Based on these results, a rigorous optimization of the FERS-based methodology in terms of sensitivity and accuracy was achieved by the utilization of spatial filtering for the intrinsic fiber-silica Raman signal. As a result, the SNR could be increased by a factor of 10 and the silica noise level could be reduced by a factor of 6 at once. Thus, fiber-enhanced rotational and ro-vibrational Raman spectroscopy was combined for the simultaneous monitoring of molecular H_2 and CH_4 within a mixture of the major breath components N_2, O_2, $^{12}CO_2$, and $^{13}CO_2$ for a concentration range between 5 and 50 ppm. The simultaneous analysis of the gas components CH_4 and H_2, which are generated by the anaerobic metabolism of colon bacteria *Escherichia coli*, can improve the diagnostic accuracy to 15 - 30 % for patients with malabsorption of oligosaccharides. On the other hand, the scaling potential for the improved FERS sensor to even higher sensitivities

was experimentally explored by the detection of ambient air including the naturally low concentrated compounds $^{13}CO_2$ and CH_4 at 3.6 ppm and 2.0 ppm. This resulted in a noise-equivalent LOD of 0.1 ppm. Remarkably, this value represents the lowest LOD detected under ambient conditions, which has been reported for any state-of-the-art enhanced Raman spectroscopic gas sensor.

Finally, a highly miniaturized and very robust, but less sensitive cavity-enhanced Raman gas sensor was utilized for the accurate online quantification of respiration rates and changes in the respiratory quotient for trees exposed to stress treatments. Thus, it was possible to quantify minor relative changes of naturally concentrated O_2 and CO_2 simultaneously on a high ambient background of 21 vol. % for O_2 and to monitor the respiration rates of chambered branches in situ over weeks. These findings suggest that respiratory substrates other than carbohydrates are used under carbon limitation. Further studies should invest on the stoichiometry of the gas exchange and should address the resource translocation across the plant organs as a function of the substrate changes within the investigated branch section.

The different experiments for both enhanced Raman spectrometric methods, the fiber-based and the cavity-based approach, demonstrate their importance and potential for a wide range of significant research questions. In particular, the ability to measure minor sample volumes of exhaled human breath and the ability to simultaneously measure O_2 and CO_2 besides other gases like N_2 in-situ on a high ambient background in comparison to less easy-to-operate and less inexpensive gas sensors is unique. The presented measurements did not influence or disturb the experiment itself by consumption of the different gas molecules and sample preparation steps were not necessary.

The great advantages of microstructured optical fibers for enhanced analytical sensitivity at very low sample demand reveal the potential for detection of breath-to-breath cycles, for monitoring of a complex (volatile) anesthetics matrix, or for the diagnosis of metabolic diseases including lactose intolerance, fructose malabsorption, and bacterial overgrowth syndrome, together with the utilization of thermoelectrically cooled, miniaturized spectrometers. There is an urgent demand for techniques operating in a high dynamic concentration range with high chemical selectivity, without the need for sample preparation, and thus can fill the gap of already well-established analytical techniques. Future investigations on device miniaturization, cost reduction, low maintenance costs, easy operability and calibration, together with low power consumption will enable these Raman instruments further to be used for the elucidation of complex environmental processes and easy-to-apply, point-of-care diagnosis of metabolic disorders and diseases.

Zusammenfassung

Das Hauptziel dieser Arbeit war die Verbindung konventioneller Raman-Spektroskopie mit der Verstärkung der Lichtintensität durch mikrostrukturierte optische Hohlkernfasern, speziell die photonische Kristallstrukturfaser (HC-PCF[1]). Die Faserverstärkte Raman-Spektrometrie (FERS[2]) ist eine neuartige Technik mit vielen Vorteilen gegenüber bekannter Gasmesstechniken. Die Herausforderung der sensitiven Gasdetektion mittels FERS ergibt sich durch die Ausnutzung des Stokes-Raman-Effektes, welcher jedoch auf dem unelastischen Streuprozess beteiligter Gasmoleküle mit geringer Teilchendichte basiert und statistisch weniger häufig gegenüber konkurrierenden Effekten wie der Absorption oder Fluoreszenz auftritt. Die Verstärkung und optimierte Einsammlung Raman-gestreuter Photonen durch kommerziell verfügbare HC-PCF[3] realisieren eine Signalverstärkung im Bereich von 4 bis 5 Größenordnungen gegenüber der konventionellen Raman-Gasspektrometrie und ermöglichen dadurch die applikationsorientierte Analyse und Quantifizierung komplexer Multikomponenten-Gasgemische. Entscheidende Vorteile der Raman-Spektroskopie, wie die selektive und simultane Detektion nahezu aller Gaskomponenten, werden der Gasanalytik dadurch zugänglich gemacht. Die Quantifizierung homoatomarer Gase wie H_2, N_2 oder O_2 und deren Isotope stellt hierbei eine Besonderheit der Raman-Gasspektrometrie dar. Diese sind mit vergleichbaren Techniken wie die Absorptionsspektroskopie schwierig zu messen und Anwendungen beschränken sich deshalb auf die Detektion vereinzelter Gase. Gerade die Vielzahl an gleichzeitig nachweisbarer, mehratomiger Gasmoleküle macht die Raman-Spektroskopie als analytische Messtechnik einzigartig, da relevante Multikomponenten-Gasgemische auf herkömmliche Art schwierig zu quantifizieren sind.

Im ersten Teil der Arbeit wird die Entwicklung und optische Charakterisierung des Faserverstärkten Raman-Gassensors mit einzigartigen Vorteilen vorgestellt. Die verwendeten HC-PCF als ideale Mikroküvette erzeugt dabei einen geeigneten Überlapp zwischen Laserlicht und Gasmolekülen innerhalb des hohlen Faserkerns. Zudem skaliert die Signalverstärkung mit der Faserlänge und weiterhin linear mit der Gaskonzentration, aber auch mit der Moleküldichte und der Laserleistung innerhalb der optischen Faser. Die gezeigte exzellente Linearität ermöglichte eine generell einfache und schnelle Zweipunktkalibration des Raman-Gassensors mit Hilfe von Reinstgasen, welche die benötigte Genauigkeit für eine Vielzahl unterschiedlicher Experimente gewährleistete. Klimarelevante Gase wie CH_4, CO_2 und N_2O zusammen mit N_2 und O_2 konnten simultan bis zu Nachweisgrenzen von 4 ppm[4] quantifiziert werden. Der hohe dynamische Bereich umfasste dabei 6 Größenordnungen. Darüber hinaus wurde die extreme Spezifität durch die simultane Detektion einer Vielzahl von chemisch fast identischen Isotopen am Beispiel von CO_2 gezeigt. Die enorme Steigerung der Signalverstärkung durch die Erhöhung der Anzahl wechselwirkender Gasmoleküle mit dem Laserlicht innerhalb der mikrostrukturierten Hohlkernfaser ermöglichte in einem anderen Experiment die Quantifizierung einer Vielzahl von Gaskomponenten innerhalb der menschlichen Ausatemluft. Diese setzt sich zusammen aus Hauptanteilen von $^{14}N_2$, $^{16}O_2$ und $^{12}CO_2$, sowie $^{14}N^{15}N$ und $^{13}CO_2$ mit geringeren Konzentrationen im unteren ppm-Bereich und kann zur Diagnostik und Früherkennung von metabolischen Krankheiten dienen.

---

[1] hollow-core photonic crystal fiber

[2] fiber-enhanced Raman spectrometry

[3] beispielsweise von NKT Photonics

[4] parts per million - Teilchen pro Million

Die Anwendung dieser neuen Gasmesstechnik in verschiedenen Experimenten offenbarte jedoch einen hohen Anteil an inhärentem Raman-Signal. Dieser intrinsische Raman-Streuanteil ist Folge der Quarzglas-Mikrostruktur, welche die photonische Bandlückenstruktur und die daraus resultierende Lichtführung von Laser- und Signallicht gewährleistet. Dieser hohe Raman-Signaluntergrund führt generell zu einer Verschlechterung der Sensorempfindlichkeit. Die exakte Lokalisierung und gezielte Rauschsignalfilterung würden eine gesteigerte Nachweisempfindlichkeit ermöglichen.

Die räumliche Indentifikation und Quantifizierung des parasitären Raman-Glassignals gegenüber des Analytensignals konnten durch die erstmalige Kombination der FERS-Technik mit einem existierenden faserbündelbasierten Raman-Bildgebungsaufbau [16] realisiert werden. Im Vergleich zu üblichen Wellenlängenscanverfahren oder räumlich abtastenden Scanverfahren sind Messungen mit diesem kombinierten Aufbau weniger zeitaufwendig. Erzielte Erkenntnisse über instantane Signaländerungen aufgrund geringster Faserbiegeradien oder genereller Faserinstabilitäten (Temperatur, Druck, Einkopplung, ...) wurden untersucht und flossen in die Sensorkalibration ein. Durch diese hyperspektralen Raman-Bildgebungsexperimente konnten signifikante Raman-Glassignalanteile im äußeren Bereich des Faserkerns mit höherer numerischer Apertur identifiziert werden. Die gezielte räumliche Filterung dieser Signalanteile gegenüber des Analytensignals im Inneren des Faserkerns mit geringerer numerischer Apertur erhöhte die Nachweisempfindlichkeit des FERS-Gassensors um eine Größenordnung bei gleichzeitiger Rauschsignal-Reduktion um den Faktor 6. Der dynamische Bereich erhöhte sich auf mehr als 7 Größenordnungen und ermöglichte eine kombinierte faserbasierte Rotations-Schwingungsspektroskopische Überwachung von H_2-Rotationsbanden und der Schwingungsbanden von CH_4 in einem Wellenzahlbereich von $300 - 3000$ cm^{-1} für den Konzentrationsbereich von $5 - 50$ ppm innerhalb eines komplexen Atemgasprofils. Eine solch detaillierte Analyse aller bekannten Atemspurengase im erweiterten dynamischen Bereich von über 7 Größenordnungen, was einer Nachweisempfindlichkeit von einigen 100 ppb[5] entspricht, ist Voraussetzung für die zuverlässige Identifikation und Interpretation wichtiger Krankheitsbiomarker. Eine mögliche Anwendung für die FERS-Diagnose ist der Wasserstoff-Atemtest als Indikator für Laktose-Intoleranz und für kleine Darmbakterienwucherungen. Im Falle einer Malabsorption von Oligosacchariden wird H_2 durch anaeroben Stoffwechsel der Darmbakterien *Escherichia coli* erzeugt; bei gesunden Probanden hingegen ist dieser nicht detektierbar. Eine zusätzliche Analyse von CH_4 kann die Diagnosegenauigkeit um $15 - 30$ % der Patienten verbessern, bei denen die methanogenen Bakterien *Methanobrevibacter smithii* H_2 in CH_4 konvertieren. Somit könnte eine schnelle und simultane FERS-Analyse von H_2 und CH_4 eine neue und einfach anzuwendende Technik im Bereich der Vor-Ort-Diagnose metabolischer Krankheiten darstellen.

Im weiteren Verlauf wurde die Faserverstärkte Raman-Gasspektrometrie mit der Laserkavität-verstärkten Raman-Gasspektrometrie (CERS[6]) [100] verglichen. Es zeigte sich, dass Letztere einerseits geringere Nachweisempfindlichkeiten bei viel höheren Probenvolumina zeigte, andererseits jedoch ein energieeffizienter und miniaturisierter Ansatz zur Langzeitüberwachung biogener Gase für verschiedenste ökophysiologische Problemstellungen ist. Im letzten Teil dieser Arbeit wird die Echtzeit-Quantifizierung von Atmungsraten und geringste Veränderungen des sogenannten Atmungsquotienten (RQ[7]) verschiedener Baumarten unter Stressbelastungen wie Trockenheit oder Beschattung durch CERS vorgestellt. Die simultane Detektion kleinster relativer Konzentrationsänderung von natürlich konzentriertem O_2 und CO_2 gegenüber einem hohen Umgebungsuntergrund, und die Bestimmung der Atmungsraten der zu untersuchenden Baumarten

---

[5]parts per billion - Teilchen pro Milliarde
[6]cavity-enhanced Raman spectrometry
[7]respiratory quotient

für mehrere Wochen waren hierbei einzigartig. Die erzielten Ergebnisse legen nahe, dass neben Kohlenhydraten als primäre respiratorische Substrate auch verstärkt andere Substrate, wie beispielweise Aminosäuren oder Fettsäuren, innerhalb des pflanzlichen Organismus' bei einer Kohlenstofflimitation genutzt werden. Eigene darauffolgende und komplexere Studien bestätigten diese Interpretation [57].

Die vorgestellten Experimente auf dem Gebiet der verstärkten Raman-Gasspektrometrie, welche einerseits auf dem Faseransatz und anderseits auf dem Ansatz einer Laserkavität basieren, zeigten ihre analytische Bedeutung für eine Vielzahl stark relevanter Forschungsfragen im Bereich der Pflanzen-Ökophysiologie und der klinischen Atemgasdiagnostik. Weder beeinflussten noch veränderten die vorgestellten Messungen die Experimente beispielsweise durch einen Analytenverbrauch, noch war eine Probenvorbereitung erforderlich. Die entscheidenden Vorteile mikrostrukturierter optischer Fasern für eine verbesserte analytische Sensorempfindlichkeit bei gleichzeitig sehr geringem Probenbedarf verdeutlicht das Anwendungspotential der Faserverstärkten Raman-Gasspektrometrie zur Überwachung von Atem-zu-Atem-Zyklen oder einer komplexen Anästhetika Matrix, die Diagnose von metabolischen Erkrankungen einschließlich der Laktoseintoleranz, intestinale Fruktoseintoleranz und der Dünndarmfehlbesiedlung. Es besteht ein notwendiger Bedarf an innovativen Gassensor-Techniken, die in einem weiten dynamischen Bereich mit hoher chemischer Selektivität funktionieren, um somit die Lücke bereits etablierter analytischer Verfahren schließen zu können. Eine weitere Miniaturisierung durch den Einsatz thermoelektrisch-gekühlter, miniaturisierter Spektrometer, aber auch die zukünftige Kostensenkung, einfache Bedienbarkeit und Kalibration zusammen mit niedrigem Leistungsverbrauch werden es diesen beiden innovativen Techniken ermöglichen, sich als Standardgasanalysetechniken neben der Gaschromatographie zu etablieren. Komplexe Umweltprozesse und eine einfach realisierbare Vor-Ort-Diagnostik von metabolischen Störungen und Krankheiten mittels der Atemgasanalyse stehen hierbei vermehrt im Vordergrund.
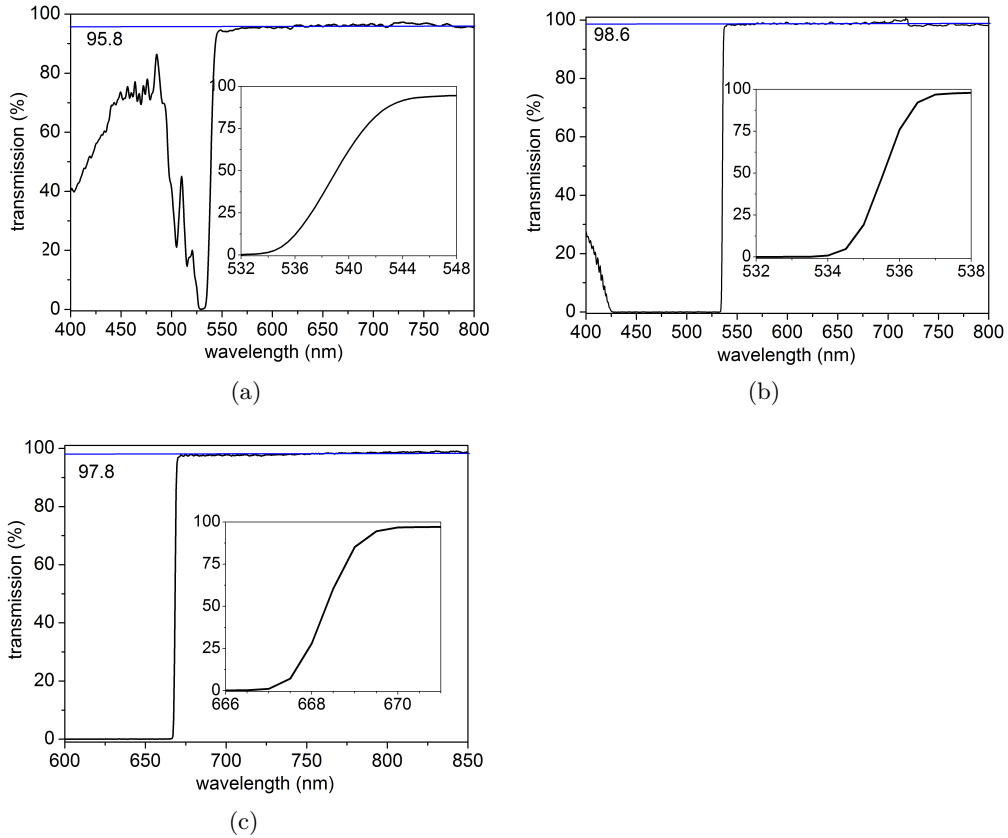
Appendix A

Experimental setup

Figure A.1: Transmittance curve of (a) Semrock Razor Dichroic filter (LPD01-532RU-25) at an incident angle of 45 °, (b) Semrock Razor RazorEdge filter (LP03-532RU-25) for 532 nm excitation wavelength at an incident angle of 10 °, and (c) Semrock Razor RazorEdge filter (LP02-664RU-25) for 660 nm excitation wavelength at an incident angle of 0 °. The individual inset shows a more detailed view around the designed edge for the specific laser wavelength. All transmission curves were measured with the help of a UV-VIS spectrometer "Specord" from Carl Zeiss.
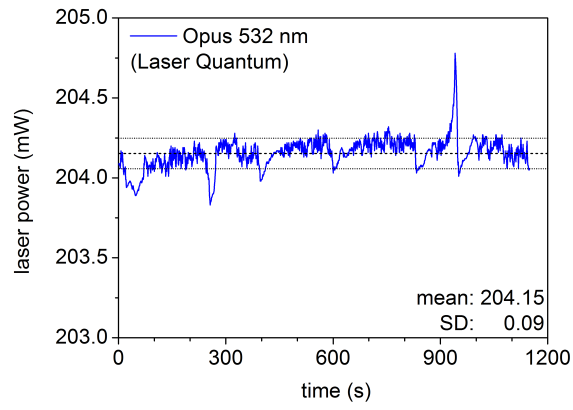
Figure A.2: Laser stability of the Opus laser at 532 nm excitation wavelength (Laser Quantum) [124], which was additionally equipped with a fan-cooled laser plate. The power around 200 mW was monitored for approx. 20 min after a warm-up time of $\sim$ 10 min.
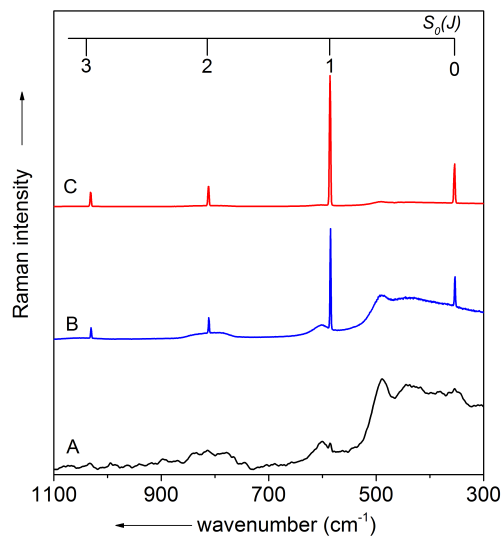
Figure A.3: Raman spectra referring to tab. 6.1: Comparison of the detection ability for the pure rotational transition lines of molecular hydrogen (concentrated with 5 vol. % in rest carrier gas nitrogen) in the case of (A) conventional Raman spectroscopy and after applying (B) the spatial and (C) the modal pinhole for FERS.

Appendix B

Supplementary information

B.1 Concentration measurements of substrates

Glucose, fructose, sucrose, inositol, and starch concentrations in leaves and branches were analyzed as the major physiologically important carbon storage compounds. Branch and needle samples were collected at the beginning and end for each treatment and species. Samples were cut, immediately frozen by immersion in liquid nitrogen, and afterwards kept on dry ice until they were placed in a freezer at -80 °C for longer storage. For further non-structural carbohydrate (NSC) extractions, the frozen samples were vacuum freeze-dried for 3 days and milled with a ball mill (Retsch® MM200) to fine powder. 50 mg of the samples were added to 1 ml of distilled water to extract the soluble sugars and afterwards vortexed, incubated (10 min at 65 °C), and centrifuged at 12000 g for another 6 min. The procedure of supernatant removal with a pipette and further storage on ice was repeated twice [148]. 50 mg of ground sample was added to 0.35 ml distilled water, vortexed (1 min), and treated at 65 °C for 10 min to hydrolyze the starch content. Afterwards, 0.5 ml of 52 % perchloric acid were added and the solution was incubated in an orbital shaker for another 20 min with further centrifuging at 12000 g for 6 min. The supernatant was removed and the procedure repeated [148]. These supernatants were pooled and stored frozen at -20 °C. The extract from soluble sugar and starch were diluted with high-pressure liquid chromatography pulsed amperometric detection (HPLC-PAD) by ion chromatography with auto sampler (Dionex® ICS 3000). The concentrations of starch resulted as difference in glucose concentration in the hydrolyzed extract, subtracted by half of the sucrose concentration in the water-soluble sugar extract, and multiplied by a conversion factor of 0.9 [179].

By using the method of Eggstein & Kuhlmann the concentration of triacylglycerol (lipids) was determined [48]. 1 ml of 0.5 M NaOH was added to 10 mg of grounded plant material, vortexed, and incubated in a thermomixer (70 °C for 30 min) for saponification of lipids. Samples cooled down to room temperature and addition of 0.2 ml 2.5 M PCA neutralized the extract, followed by vortexing and centrifuging at 12000 g. An aliquot of 0.3 ml was diluted in 0.7 ml of bi-distilled water. To define the concentration of total glycerol, the enzymatic conversion of glycerol to glycerol-3-phosphat was followed photometrically at 340 nm, using a microplate reader (Infinite M200, Tecan) with pure glycerol, which was used as standard. Enzymes were purchased from Sigma-Aldrich GmbH (glycero-kinase and lactate-dehydrogenase) and Roche Diagnostic GmbH (pyruvat kinase).

Bibliography

[1] A. Ahnoux-Zabsonre, M. Quaranta, and M. Mauget-Faysse. Prevalence de l'helicobacter pylori dans la chorioretinopathie sereuse centrale et l'eliopathie retinienne diffuse. *Journal Francais d'Ophtalmologie*, 27(10):1129–1133, 2004.

[2] M. Alharbi, T. Bradley, B. Debord, C. Fourcade-Dutin, D. Ghosh, L. Vincetti, F. Gerome, and F. Benabid. Cladding effect on confinement and bend losses in hypocycloid-core kagome hc-pcf. In *CLEO: 2013*. Optical Society of America, 2013.

[3] F. Alsmeyer and W. Marquardt. Automatic generation of peak-shaped models. *Appl. Spectrosc.*, 58(8):986–994, 2004.

[4] R. Altkorn, Michelle D. Malinsky, R. P. Van Duyne, and I. Koev. Intensity considerations in liquid core optical fiber raman spectroscopy. *Appl. Spectrosc.*, 55(4):373–381, 2001.

[5] A. Amann and D. Smith. *Breath Analysis For Clinical Diagnosis And Therapeutic Monitoring*. Wspc, 2005.

[6] G. Amat and M. Pimbert. On fermi resonance in carbon dioxide. *Journal of Molecular Spectroscopy*, 16(2):278–290, 1965.

[7] A. Anderson and T. S. Sun. Raman spectra of molecular crystals. carbon dioxide and nitrous oxide. *Chemical Physics Letters*, 8(6):537–542, 1971.

[8] M. O. Andreae, D. S. Schimel, and G. P. Robertson. *Exchange of Trace Gases between Terrestrial Ecosystems and the Atmosphere*. Wiley, 1989.

[9] G. Antonopoulos. *Super-enhanced stimulated Rpart scattering and particle guidance in photonic-core photonic crystal fibres*. PhD thesis, University of Bath, 2006.

[10] G. Antonopoulos, F. Benabid, T. A. Birks, D. M. Bird, J. C. Knight, and P. St J. Russell. Experimental demonstration of the frequency shift of bandgaps in photonic crystal fibers due to refractive index scaling. *Opt. Express*, 14(7):3000–3006, 2006.

[11] H. Babovsky. On knudsen flows within thin tubes. *Journal of Statistical Physics*, 44(5-6):865–878, 1986.

[12] J. F. Bertrán. Study of the fermi doublet v1 and 2v2 in the raman spectra of co2 in different phases. *Spectrochimica Acta Part A: Molecular Spectroscopy*, 39(2):119–121, 1983.

[13] J. Bethge, A. Husakou, F. Mitschke, F. Noack, U. Griebner, G. Steinmeyer, and J. Herrmann. Two-octave supercontinuum generation in a water-filled photonic crystal fiber. *Opt. Express*, 18(6):6230–6240, 2010.

[14] T. Birks, D. Bird, T. Hedley, J. Pottage, and P. Russell. Scaling laws and vector effects in bandgap-guiding fibres. *Opt. Express*, 12(1):69–74, 2004.

[15] T. A. Birks, P. J. Roberts, P. Russell, D. M. Atkin, and T. J. Shepherd. Full 2-d photonic bandgaps in silica/air structures. *Electronics Letters*, 31(22):1941–1943, 1995.

[16] M. Brückner, T. Frosch, and J. Popp. Raman-spektroskopie-beleuchtungs- und auslesesystem, patent, de102015001032.8, 2015.

[17] P. Brimblecombe. *Air Composition and Chemistry.* Cambridge University Press, 1996.

[18] R. Brouquisse, F. James, P. Raymond, and A. Pradet. Study of glucose starvation in excised maize root tips. *Plant Physiol.*, 96(2):619–626, 1991.

[19] J. Bures. Small intestinal bacterial overgrowth syndrome. *World Journal of Gastroenterology*, 16(24):2978, 2010.

[20] M. P. Buric, K. Chen, J. Falk, R. Velez, and S. Woodruff. Raman sensing of fuel gases using a reflective coating capillary optical fiber. *Proceedings of the SPIE*, 7316, 2009.

[21] M. P. Buric, K. Chen, J. Falk, and S. Woodruff. Enhanced spontaneous raman scattering and gas composition analysis using a photonic crystal fiber. *Appl. Opt.*, 47(23):4255–4261, 2008.

[22] M. P. Buric, K. Chen, J. Falk, and S. Woodruff. Improved sensitivity gas detection by spontaneous raman scattering. *Appl. Opt.*, 48(22):4424–4429, 2009.

[23] M. P. Buric, K. P. Chen, J. Falk, and S. D. Woodruff. Multimode metal-lined capillaries for raman collection and sensing. *J. Opt. Soc. Am. B*, 27(12):2612–2619, 2010.

[24] B. Bussian and W. Härdle. Robust smoothing applied to white noise and single outlier contaminated raman spectra. *Appl. Spectrosc.*, 38(3):309–313, 1984.

[25] B. Buszewski, M. Kesy, T. Ligor, and A. Amann. Human exhaled air analytics: biomarkers of diseases. *Biomedical Chromatography*, 21(6):553–566, 2007.

[26] F. F. Calegario, R. G. Cosso, F. V. Almeida, A. E. Vercesi, and W. F. Jardim. Determination of the respiration rate of tomato fruit using flow analysis. *Postharvest Biology and Technology*, 22(3):249–256, 2001.

[27] D. H. Calloway, E. L. Murphy, and D. Bauer. Determination of lactose intolerance by breath analysis. *The American Journal of Digestive Diseases*, 14(11):811–815, 1969.

[28] W. Cao and Y. Duan. Breath analysis: potential for clinical diagnosis and exposure assessment. *Clin. Chem.*, 52(5):800–811, 2006.

[29] C. B. Carter and G. Norton. *Ceramic Materials: Science and Engineering.* Springer, 2007.

[30] S. A. Cerqueira Jr. Recent progress and novel applications of photonic crystal fibers. *Reports on Progress in Physics*, 73(2), 2010.

[31] A. Chedin. The carbon dioxide molecule: Potential, spectroscopic, and molecular constants from its infrared spectrum. *Journal of Molecular Spectroscopy*, 76(1-3):430–491, 1979.

[32] R. Chen, P. J. Codella, R. Guida, A. Zribi, A. Vert, R. Potyrailo, and M. Baller. Photonic bandgap fiber-enabled raman detection of nitrogen gas. volume 7322. SPIE, 2010.

[33] K. Chida, F. Hanawa, and M. Nakahara. Fabrication of oh-free multimode fiber by vapor phase axial deposition. *Journal of Quantum Electronics, IEEE*, 18(11):1883–1889, 1982.

[34] Y. Chikaraishi, N. O. Ogawa, H. Doi, and N. Ohkouchi. 15n/14n ratios of amino acids as a tool for studying terrestrial food webs: a case study of terrestrial insects (bees, wasps, and hornets). *Ecological Research*, 26(4):835–844, 2011.

[35] K. K. Chow, M. Short, S. Lam, A. McWilliams, and H. Zeng. A raman cell based on hollow core photonic crystal fiber for human breath analysis. *Medical Physics*, 41(9), 2014.

[36] F. Couny, F. Benabid, and P. S. Light. Large-pitch kagome-structured hollow-core photonic crystal fiber. *Opt. Lett.*, 31(24):3574–3576, 2006.

[37] M. F. Crawford, H. L. Welsh, and J. H. Harrold. Rotational wings of raman bands and free rotation in liquid oxygen, nitrogen, and methane. *Canadian Journal of Physics*, 30(2):81–98, 1952.

[38] A. M. Cubillas, M. Schmidt, T. G. Euser, N. Taccardi, S. Unterkofler, P. Russell, P. Wasserscheid, and B. J. M. Etzold. In situ heterogeneous catalysis monitoring in a hollow-core photonic crystal fiber microflow reactor. *Advanced Materials Interfaces*, 1(5), 2014.

[39] A. M. Cubillas, M. Schmidt, M. Scharrer, T. G. Euser, B. J. M. Etzold, N. Taccardi, P. Wasserscheid, and P. Russell. Ultra-low concentration monitoring of catalytic reactions in photonic crystal fiber. *Chemistry - A European Journal*, 18(6):1586–1590, 2012.

[40] A. M. Cubillas, S. Unterkofler, T. G. Euser, B. J. M. Etzold, A. C. Jones, P. J. Sadler, P. Wasserscheid, and P. Russell. Photonic crystal fibres for chemical sensing and photochemistry. *Chem. Rev.*, 42:8629–8648, 2013.

[41] J. Darnell. *Molecular Cell Biology*. Freeman & Company, 1986.

[42] M. de Vrese, A. Stegelmann, B. Richter, S. Fenselau, C. Laue, and J. Schrezenmeir. Probiotics - compensation for lactase insufficiency. *The American Journal of Clinical Nutrition*, 73(2):421–429, 2001.

[43] W. Demtröder. *Laser Spectroscopy: Vol. 1: Basic Principles*. Laser Spectroscopy. Springer-Verlag, 2008.

[44] T. Dieing, O. Hollricher, and J. Toporski. *Confocal Raman Microscopy*. Springer Series in Optical Sciences. Springer, 2011.

[45] M. Dieuaide-Noubhani, P. Canioni, and P. Raymond. Sugar-starvation-induced changes of carbon metabolism in excised maize root tips. *Plant Physiol.*, 115(4):1505–1513, 1997.

[46] P. M. Dove, N. Han, A. F. Wallace, and J. J. De Yoreo. Kinetics of amorphous silica dissolution and the paradox of the silica polymorphs. *Proc. Natl. Acad. Sci. USA*, 105(29):9903–9908, 2008.

[47] F. Eftekhari, J. Irizar, L. Hulbert, and A. S. Helmy. A comparative study of raman enhancement in capillaries. *Journal of Applied Physics*, 109(11), 2011.

[48] M. Eggstein and E. Kuhlmann. *Triglyceride und Glycerin (alkalische Verseifung). In Methoden der enzymatischen Analyse. Band II*. Weinheim: Verlag Chemie, 1974.

[49] F. Ehrentreich and L. Sämmchen. Spike removal and denoising of raman spectra by wavelet transform methods. *Anal. Chem.*, 73(17):4364–4373, 2001.

[50] S. C. Eichmann, M. Weschta, J. Kiefer, T. Seeger, and A. Leipertz. Characterization of a fast gas analyzer based on raman scattering for the analysis of synthesis gas. *Review of Scientific Instruments*, 81(12):125104–1, 2010.

[51] T. Eidam, S. Hanf, E. Seise, T. Andersen, T. Gabler, C. Wirth, T. Schreiber, and A. Limpert, J. Tünnermann. Femtosecond fiber cpa system emitting 830 w average output power. *Opt. Lett.*, 35(2):94–96, 2010.

[52] J. M. Eiler and E. Schauble. 18o13c16o in earth's atmosphere. *Geochimica et Cosmochimica Acta*, 68(23):4767–4777, 2004.

[53] A. Eisenmann, A. Amann, M. Said, B. Datta, and M. Ledochowski. Implementation and interpretation of hydrogen breath tests. *J. Breath. Res.*, 2(4), 2008.

[54] L. Eklund. Endogenous levels of oxygen, carbon dioxide and ethylene in stems of norway spruce trees during one growing season. *Trees*, 4(3):150–154, 1990.

[55] W. R. Fenner, H. A. Hyatt, J. M. Kellam, and S. P. S. Porto. Raman cross section of some simple gases. *J. Opt. Soc. Am.*, 63(1):73–77, 1973.

[56] E. Fermi. Über den ramaneffekt des kohlendioxyds. *Zeitschrift für Physik*, 71(3-4):250–259, 1931.

[57] S. Fischer, S. Hanf, T. Frosch, M. Reichelt, G. Gleixner, J. Popp, S. Trumbore, and H. Hartmann. Pinus sylvestris switches respiration substrates under shading but not during drought. *New Phyt.*, 2015 (accepted).

[58] J. Flexas, J. Bota, J. Galmes, H. Medrano, and M. Ribas-Carba. Keeping a positive carbon balance under adverse conditions: responses of photosynthesis and respiration to water stress. *Physiologia Plantarum*, 127(3):343–352, 2006.

[59] F. Flora and L. Giudicotti. Complete calibration of a thomson scattering spectrometer system by rotational raman scattering in h(2). *Appl. Opt.*, 26(18):4001–4008, 1987.

[60] P. Forster and et. al. *Changes in atmospheric constituents and in radiative forcing.* Cambridge University Press, 2007.

[61] A. Fried, F. D'Amato, A. Lancia, and P. W. Werle. Very precise measurement of carbon dioxide atmospheric concentration by using tdls. volume 2834, pages 242–248, 1996.

[62] T. Frosch, D. Yan, and J. Popp. Ultrasensitive fiber enhanced uv resonance raman sensing of drugs. *Anal. Chem.*, 85(13):6264–6271, 2013.

[63] P. Genix, R. Bligny, JB. Martin, and R. Douce. Transient accumulation of asparagine in sycamore cells after a long period of sucrose starvation. *Plant Physiol.*, 94(2):717–722, 1990.

[64] E. Gerecht, K. O. Douglass, and D. F. Plusquellic. Chirped-pulse terahertz spectroscopy for broadband trace gas sensing. *Opt. Express*, 19(9):8973–8984, 2011.

[65] A. Gessler, G. Tcherkez, O. Karyanto, C. Keitel, J. P. Ferrio, J. Ghashghaie, J. Kreuzwieser, and G. D. Farquhar. On the metabolic origin of the carbon isotope composition of co2 evolved from darkened light-acclimated leaves in ricinus communis. *New Phyt.*, 181(2):374–386, 2009.

[66] U. C. Ghoshal. How to interpret hydrogen breath tests. *J Neurogastroenterol Motil*, 17(3):312–317, 2011.

[67] U. C. Ghoshal and D. Srivastava. Irritable bowel syndrome and small intestinal bacterial overgrowth: Meaningful association or unnecessary hype. *World J. Gastroenterol.*, 20(10):2482–2491, 2014.

[68] U.C. Ghoshal and A. Misra. Utility of hydrogen breath tests in diagnosis of small intestinal bacterial overgrowth in malabsorption syndrome and its relationship with oro-cecal transit time. *Indian J Gastroenterol.*, 25(1):6–10, 2006.

[69] P. R. Gibson, E. Newnham, J. S. Barrett, S. J. Shepherd, and J. G. Muir. Review article: fructose malabsorption and the bigger picture. *Aliment Pharmacol Ther*, 25(4):349–363, 2007.

[70] C. Giusti. Association of helicobacter pylori with central serous chorioretinopathy: hypotheses regarding pathogenesis. *Medical Hypotheses*, 63(3):524–527, 2004.

[71] Lasos Lasertechnik GmbH. Endmontage - glk 3250t01 (data sheet), 2012.

[72] A. F. Goddard and R. P. H. Logan. Urea breath tests for detecting helicobacter pylori. *Alimentary Pharmacology and Therapeutics*, 11(4):641–649, 1997.

[73] H. R. Gordon and T. K. McCubbin Jr. The 2.8-micron bands of co2. *Journal of Molecular Spectroscopy*, 19(1-4):137–154, 1966.

[74] I. Grattagliano, B. H. Lauterburg, G. Palasciano, and P. Portincasa. 13c-breath tests for clinical investigation of liver mitochondrial function. *European Journal of Clinical Investigation*, 40(9):843–850, 2010.

[75] F. Gérôme, R. Jamier, J. Auguste, G. Humbert, and J. Blondy. Simplified hollow-core photonic crystal fiber. *Opt. Lett.*, 35(8):1157–1159, 2010.

[76] C. Haisch and R. Niessner. Light and sound - photoacoustic spectroscopy. *spectrosc eur*, 14(5):10–15, 2002.

[77] H. Haken and H. C. Wolf. *Molecular Physics and Elements of Quantum Chemistry: Introduction to Experiments and Theory*. Advanced Texts in Physics. Springer, 2004.

[78] S. Hanf. Untersuchung der verstärkungscharakteristik von ytterbium-dotierten ultrakurzpulsfaserlasern. Master's thesis, Friedrich-Schiller Univeristät Jena, 2010.

[79] S. Hanf, T. Bögözi, R. Keiner, T. Frosch, and J. Popp. Fast and highly sensitive fiber-enhanced raman spectroscopic monitoring of molecular h2 and ch4 for point-of-care diagnosis of malabsorption disorders in exhaled human breath. *Anal. Chem.*, 87(2):982–988, 2015.

[80] S. Hanf, S. Fischer, H. Hartmann, R. Keiner, S. Trumbore, J. Popp, and T. Frosch. Online investigation of respiratory quotients in pinus sylvestris and picea abies during drought and shading by means of cavity-enhanced raman multi-gas spectrometry. *Anal. Chem.*, 2015 (submitted).

[81] S. Hanf, T. Frosch, and J. Popp. Verfahren und anordnung zur wasserstoff-sensorik, patent, de102014014414.3, 2014.

[82] S. Hanf, R. Keiner, D. Yan, J. Popp, and T. Frosch. Fiber-enhanced raman multi-gas spectroscopy: a versatile tool for environmental gas sensing and breath analysis. *Anal. Chem.*, 86(11):5278–5285, 2014.

[83] S. B. Hansen, R. W. Berg, and E. H. Stenby. High-pressure measuring cell for raman spectroscopic studies of natural gas. *Appl. Spectrosc.*, 55(1):55–60, 2001.

[84] H. Hartmann, W. Ziegler, O. Kolle, and S. Trumbore. Thirst beats hunger - declining hydration during drought prevents carbon starvation in norway spruce saplings. *New Phyt.*, 200(2):340–349, 2013.

[85] T. Hübert, L. Boon-Brett, G. Black, and U. Banach. Hydrogen sensors - a review. *Sensors and Actuators B*, 157(2):329–352, 2011.

[86] J. Henningsen and J. Hald. Dynamics of gas flow in hollow core photonic bandgap fibers. *Appl. Opt.*, 47(15):2790–2797, 2008.

[87] W. Hill and D. Rogalla. Spike-correction of weak signals from charge-coupled devices and its application to raman spectroscopy. *Anal. Chem.*, 64(21):2575–2579, 1992.

[88] J. O. Hirschfelder, C. F. Curtisselder, C. F. Curtiss, and R. B. Bird. *Molecular theory of gases and liquids*, volume 17 of *Journal of Polymer Science*. New York, 1955.

[89] G. M. Hoffman, A. Torres, and H. V. Forster. Validation of a volumeless breath-by-breath method for measurement of respiratory quotien. *Journal of Applied Physiology*, 75(4):1903–1910, 1993.

[90] C. Hou, J. Lei, D. Huo, K. Song, J. Li, X. Luo, M. Yang, and H. Fa. Discrimination of lung cancer related volatile organic compounds with a colorimetric sensor array. *Analytical Letters*, 46(13):2048–2059, 2013.

[91] H. E. Howard-Lock and B. P. Stoicheff. Raman intensity measurements of the fermi diad v1, 2v2 in 12co2 and 13co2. *Journal of Molecular Spectroscopy*, 37(2):321–326, 1971.

[92] Brooks Instrument. Data sheet: Gf40/gf80 - thermal mass flow, 2012.

[93] Princeton Instruments. *Acton Standard Series of Monochromators and Spectrographs*. 3660 Quakerbridge Road Trenton, NJ 08619 USA, rev. n1.8 edition, 2010.

[94] Princeton Instruments. *PIXIS 1024 eXcelon*. 3660 Quakerbridge Road Trenton, NJ 08619 USA, rev. n1.2 edition, 2010.

[95] G. Irmer and T. Graupner. Isotopes of c and o in co2: a raman study using gas standards and natural fluid inclusions, 2002.

[96] V. Jerman, M. Metje, I. Mandic-Mulec, and P. Frenzel. Wetland restoration and methanogenesis: the activity of microbial populations and competition for substrates at different temperatures. *Biogeosciences*, 6(6):1127–1138, 2009.

[97] V. L. Kasyutich and P. A. Martin. 13co2/12co2 isotopic ratio measurements with a continuous-wave quantum cascade laser in exhaled breath. *Infrared Physics & Technology*, 55(1):60–66, 2012.

[98] Y. Katsumoto and Y. Ozaki. Practical algorithm for reducing convex spike noises on a spectrum. *Appl. Spectrosc.*, 57(3):317–322, 2003.

[99] U. Kc, J. A. Silver, D. C. Hovde, and P. L. Varghese. Improved multiple-pass raman spectrometer. *Appl. Opt.*, 50(24):4805–4816, 2011.

[100] R. Keiner. *Cavity-Enhanced Raman Gas Spectrometry of Biogenic Gases*. PhD thesis, Friedrich-Schiller Univeristy Jena, 2015.

[101] R. Keiner, T. Frosch, S. Hanf, A. Rusznyak, D. M. Akob, K. Kusel, and J. Popp. Raman spectroscopy-an innovative and versatile tool to follow the respirational activity and carbonate biomineralization of important cave bacteria. *Anal. Chem.*, 85(18):8708–8714, 2013.

[102] R. Keiner, T. Frosch, T. Massad, S. Trumbore, and J. Popp. Enhanced raman multigas sensing - a novel tool for control and analysis of 13co2 labeling experiments in environmental research. *Analyst*, 139(16):3879–3884, 2014.

[103] R. Keiner, M. Gruselle, B. Michalzik, J. Popp, and T. Frosch. Raman spectroscopic investigation of 13co2 labeling and leaf dark respiration of fagus sylvatica l. (european beech). *Analytical and Bioanalytical Chemistry*, pages 1–5, 2015.

[104] S. Keitzer, M.P. Nelson, P. J. Treado, and J. Wolfe. Method and apparatus for automated spectral calibration, patent, wo2007075426 a3, 2008.

[105] E. H. Kennard. *Kinetic theory of gases: with an introduction to statistical mechanics*. International series in pure and applied physics. McGraw-Hill, 1938.

[106] A. Khetani, M. Naji, N. Lagali, H. Anis, and R. Munger. Method for using a photonic crystal fiber as a raman biosensor, 2010. US Patent 7,738,097.

[107] A. Khetani, J. Riordon, V. Tiwari, A. Momenpour, M. Godin, and H. Anis. Hollow core photonic crystal fiber as a reusable raman biosensor. *Opt. Express*, 21(10):12340–12350, 2013.

[108] A. Khetani, V. S. Tiwari, A. Harb, and H. Anis. Monitoring of heparin concentration in serum by raman spectroscopy within hollow core photonic crystal fiber. *Opt. Express*, 19(16):15244–15254, 2011.

[109] S. Kim, C. Young, B. Vidakovic, S. G. A. Gabram-Mendola, C. W. Bayer, and B. Mizaikoff. Potential and challenges for mid-infrared sensors in breath diagnostics. *Ieee Sensors Journal*, 10(1):145–158, 2010.

[110] D. A. King and R. J. Pittaro. Simple diode pumping of a power-buildup cavity. *Opt. Lett.*, 23(10):774–776, 1998.

[111] P. D. Klein and D. Y. Graham. Minimum analysis requirements for the detection of helicobacter pylori infection by the 13c-urea breath test. *The American journal of gastroenterology*, 88(11):1865–1869, 1993.

[112] K. E. Koch, Y. Wu, and J. Xu. Sugar and metabolic regulation of genes for sucrose metabolism: potential influence of maize sucrose synthase and soluble invertase responses on carbon partitioning and sugar sensing. *Journal of Experimental Botany*, 47:1179–1185, 1996.

[113] V.T. Kogan, D.S. Lebedev, A.K. Pavlov, Yu.V. Chichagov, and A.S. Antonov. A portable mass spectrometer for direct monitoring of gases and volatile compounds in air and water samples. *Instruments and Experimental Techniques*, 54(3):390–396, 2011.

[114] S. O. Konorov, C. J. Addison, H. G. Schulze, R. F. B. Turner, and M. W. Blades. Hollow-core photonic crystal fiber-optic probes for raman spectroscopy. *Opt. Lett.*, 31(12):1911–1913, 2006.

[115] R. K. Kumar, H. Tamm, and W C. Harrison. Combustion of hydrogen-steam-air mixtures near lower flammability limits. *Combustion Science and Technology*, 33(1-4):167–178, 1983.

[116] H. Lambers and M. Ribas-Carbo. *Plant Respiration: From Cell to Ecosystem.* Advances in Photosynthesis and Respiration. Springer, 2005.

[117] A. Leodolter, J. E. Dominguez-Munoz, U. von Arnim, S. Kahl, U. Peitz, and P. Malfertheiner. Validity of a modified 13c-urea breath test for pre- and post-treatment diagnosis of helicobacter pylori infection in the routine clinical setting. *Am J Gastroenterol*, 94(8):2100–2104, 1999.

[118] R. Leuning and K. M. King. Comparison of eddy-covariance measurements of co2 fluxes by open- and closed-path co2 analysers. *Boundary-Layer Meteorology*, 59(3):297–311, 1992.

[119] D. R. Lide. *CRC handbook of chemistry and physics.* CRC Press Inc, 89th edition, 2009.

[120] S. Liu, W. Gao, H. Li, Y. Dong, and H. Zhang. Liquid-filled simplified hollow-core photonic crystal fiber. *Optics & Laser Technology*, 64:140–144, 2014.

[121] D. G. Lona, H. E. Hernandez-Figueroa, S. Jr. Arismar Cerqueira, G. Stefanini, and H. L. Fragnito. Applicability of low macrobending loss hollow-core pcf to ftth applications. *Journal of Microwaves, Optoelectronics and Electromagnetic Applications*, 10:251–258, 2011.

[122] D. A. Long. *The Raman Effect: A Unified Treatment of the Theory of Raman Scattering by Molecules.* John Wiley & Sons, 2002.

[123] Laser Quantum Ltd. lux - the high power 660 nm laser - data sheet v1.5, 2012.

[124] Laser Quantum Ltd. opus - ultra quiet 532 cw laser - data sheet v2.0, 2012.

[125] F. Lu, J. Ji, L. Shao, and P. He. Bacterial bioaugmentation for improving methane and hydrogen production from microalgae. *Biotechnol Biofuels*, 6(1), 2013.

[126] G. J. Luo, N. Brüggemann, B. Wolf, R. Gasche, R. Grote, and K. Butterbach-Bahl. Decadal variability of soil co2, no, n2o, and ch4 fluxes at the höglwald forest, germany. *Biogeosciences*, 9(5):1741–1763, 2012.

[127] R. L. McCreery. *Raman Spectroscopy for Chemical Analysis.* Chemical Analysis: A Series of Monographs on Analytical Chemistry and Its Applications. Wiley, 2005.

[128] N. McDowell, W. T. Pockman, C. D. Allen, D. D. Breshears, N. Cobb, T. Kolb, J. Plaut, J. Sperry, A. West, D. G. Williams, and E. A. Yepez. Mechanisms of plant survival and mortality during drought: why do some plants survive while others succumb to drought? *New Phyt.*, 178(4):719–739, 2008.

[129] J. W. McMurdy and A. J. Berger. Raman spectroscopy-based creatinine measurement in urine samples from a multipatient population. *Appl. Spectrosc.*, 57(5):522–525, 2003.

[130] S. Ohara, J. Sato, M. Endo, S. Yamaguchi, K. Nanri, and T. Fujioka. Trace methane detection based on raman spectroscopy using a high finesse optical resonator. *The Review of Laser Engineering*, 32(3):208–210, 2004.

[131] S. Ohara, S. Yamaguchi, M. Endo, K. Nanri, and T. Fujioka. Performance characteristics of power build-up cavity for raman spectroscopic measurement. *Optical Review*, 10(5):342–345, 2003.

[132] Y. Okita, T. Katagiri, and Y. Matsuura. A raman cell based on hollow optical fibers for breath analysis. *Proceedings of the SPIE*, 7559, 2010.

[133] Y. Okita, T. Katagiri, and Y. Matsuura. Small-volume cavity cell using hollow optical fiber for raman scattering-based gas detection. *Small-volume cavity cell using hollow optical fiber for Raman scattering-based gas detection*, 2011.

[134] P. G. Papageorgas, D. Maroulis, H. Winter, S. A. Karkanis, H. Albrecht, and N. G. Theofanous. Multichannel raman gas analyzer: the data acquisition and control system. measurement improvement with blue laser light. *Instrumentation and Measurement*, 53(1):58–66, 2004.

[135] V. Parmar and R. Bhatnagar. Analysis of gas flow dynamics in hollow core photonic crystal fibre based gas cell. *Optik - International Journal for Light and Electron Optics*, 125(13):3204–3208, 2014.

[136] R. Paschotta. *Encyclopedia of Laser Physics and Technology.* Number Bd. 1. Wiley-VCH, 1. edition, 2008.

[137] W. F. Pearman, J. C. Carter, S. M. Angel, and J. W. Chan. Quantitative measurements of co2 and ch4 using a multipass raman capillary cell. *Appl. Opt.*, 47(25):4627–4632, 2008.

[138] F. Perri, R. Clemente, M. Pastore, M. Quitadamo, and V. Festa. The 13c-urea breath test as a predictor of intragastric bacterial load and severity of helicobacter pylori gastritis. *Scandinavian Journal of Clinical Laboratory Investigation*, 58(1):19–28, 1998.

[139] C. Perrotton, R. J. Westerwaal, N. Javahiraly, M. Slaman, H. Schreuders, B. Dam, and P. Meyrueis. A reliable, sensitive and fast optical fiber hydrogen sensor based on surface plasmon resonance. *Opt. Express*, 21(1):382–390, 2013.

[140] B. Petrak, N. Djeu, and A. Muller. Purcell-enhanced raman scattering from atmospheric gases in a high-finesse microcavity. *Phys. Rev. A*, 89, 2014.

[141] G. R. Phillips and Joel M. Harris. Polynomial filters for data sets with outlying or missing observations: application to charge-coupled-device-detected raman spectra contaminated by cosmic rays. *Anal. Chem.*, 62(21):2351–2357, 1990.

[142] NKT Photonics. Data sheet: Hc-1060, hollow core photonic bandgap fiber, 2014.

[143] NKT Photonics. Data sheet: Hc-1550, hollow core photonic bandgap fiber, 2014.

[144] NKT Photonics. Data sheet: Hc-532-02-101118, hollow core photonic bandgap fiber, 2014.

[145] NKT Photonics. Data sheet: Hc-580-02-100916, hollow core photonic bandgap fiber, 2014.

[146] NKT Photonics. Data sheet: Hc-633-02-100915, hollow core photonic bandgap fiber, 2014.

[147] C. Popa, D. Dutu, R. Cernat, C. Matei, A. Bratu, S. Banita, and D. Dumitras. Ethylene and ammonia traces measurements from the patients' breath with renal failure via lpas method. *Applied Physics B: Lasers and Optics*, 105(3):669–674, 2011.

[148] M. Raessler, B. Wissuwa, A. Breul, W. Unger, and T. Grimm. Chromatographic analysis of major non-structural carbohydrates in several wood species - an analytical approach for higher accuracy of data. *Analytical Methods*, 2(5):532–538, 2010.

[149] C. V. Raman and K. S. Krishnan. A new type of secondary radiation. *Nature*, 121:501–502, 1928.

[150] A. Reyes-Reyes, Z. Hou, E. van Mastrigt, R. C. Horsten, J. C de Jongste, M. W. Pijnenburg, H. P. Urbach, and N. Bhattacharya. Multicomponent gas analysis using broadband quantum cascade laser spectroscopy. *Opt. Express*, 22(15):18299–18309, 2014.

[151] J. M. Rhodes, P. Middleton, and D. P. Jewell. The lactulose hydrogen breath test as a diagnostic test for small-bowel bacterial overgrowth. *Scandinavian Journal of Gastroenterology*, 14(3):333–336, 1979.

[152] P. J. Roberts, F. Couny, H. Sabert, B. J. Mangan, D. P. Williams, L. Farr, M. W. Mason, A. Tomlinson, T. A. Birks, J. C. Knight, and P. Russell. Ultimate low loss of hollow-core photonic crystal fibres. *Opt. Express*, 13(1):236–244, 2005.

[153] V. Rodriguez-Garcia, S. Hirata, K. Yagi, K. Hirao, T. Taketsugu, I. Schweigert, and M. Tasumi. Fermi resonance in co2: A combined electronic coupled-cluster and vibrational configuration-interaction prediction. *The Journal of Chemical Physics*, 126(12), 2007.

[154] J. Romagnuolo, D. Schiller, and R. J. Bailey. Using breath tests wisely in a gastroenterology practice: an evidence-based review of indications and pitfalls in interpretation. *Am J Gastroenterol*, 97(5):1113–1126, 2002.

[155] A.O. Rudaz, E. Wälti, G. Kyburz, P. Lehmann, and J. Fuhrer. Temporal variation in n2o and n2 fluxes from a permanent pasture in switzerland in relation to management, soil water content and soil temperature. *Agriculture, Ecosystems & Environment*, 73(1):83–91, 1999.

[156] W. W. Rudolph, D. Fischer, and G. Irmer. Vibrational spectroscopic studies and density functional theory calculations of speciation in the co2-water system. *Appl. Spectrosc.*, 60(2):130–144, 2006.

[157] R. Ruser, H. Flessa, R. Russow, G. Schmidt, F. Buegger, and J. C. Munch. Emission of n2o, n2 and co2 from soil fertilized with nitrate: effect of compaction, soil moisture and rewetting. *Soil Biology and Biochemistry*, 38(2):263–274, 2006.

[158] P. Russell. Photonic crystal fibers. *Science*, 299(5605):358–362, 2003.

[159] P. Russell. Photonic-crystal fibers. *Journal of Lightwave Technology*, 24(12):4729–4749, 2006.

[160] P. H. Saglio and A. Pradet. Soluble sugars, respiration, and energy charge during aging of excised maize root tips. *Plant Physiol.*, 66(3):516–519, 1980.

[161] B. E. A. Saleh and M. C. Teich. *Grundlagen der Photonik*. Lehrbuch Physik. Wiley-VCH, 2008.

[162] R. Salter, J. Chu, and M. Hippler. Cavity-enhanced raman spectroscopy with optical feedback cw diode lasers for gas phase analysis and spectroscopy. *Analyst*, 137(20):4669–4676, 2012.

[163] T. Sato, N. Funamori, and T. Yagi. Helium penetrates into silica glass and reduces its compressibility. *Nat. Commun.*, 2, 2011.

[164] Q. Schiermeier. Renewable power: Germany's energy gamble. *Nature*, 496(7444):156–158, 2013.

[165] B. Schrader. *Infrared and Raman Spectroscopy: Methods and Applications*. Wiley, 1995.

[166] H. W. Schrötter and H. W. Kläckner. *Raman Scattering Cross Sections in Gases and Liquids*, volume 11 of *Topics in Current Physics*, book section 4, pages 123–166. Springer Berlin Heidelberg, 1979.

[167] F. Seichter, A. Wilk, K. Worle, S. S. Kim, J. A. Vogt, U. Wachter, P. Radermacher, and B. Mizaikoff. Multivariate determination of 13co2/12co2 ratios in exhaled mouse breath with mid-infrared hollow waveguide gas sensors. *Analytical and Bioanalytical Chemistry*, 405(14):4945–4951, 2013.

[168] S. Sevanto, N. G. McDowell, L. T. Dickman, R. Pangle, and W. T. Pockman. How do trees die? a test of the hydraulic failure and carbon starvation hypotheses. *Plant, Cell & Environment*, 37(1):153–161, 2014.

[169] A. E. Siegman. *Lasers*. University Science Books, 1986.

[170] M. G. Simon and C. E. Davis. *Instrumentation and Sensors for Human Breath Analysis*, volume 55. 2010.

[171] M. Simren and P. O. Stotzer. Use and abuse of hydrogen breath tests. *Gut*, 55(3):297–303, 2006.

[172] D. A. Skoog. *Fundamentals of analytical chemistry*, volume 3. Holt, Rinehart, and Winston, 1976.

[173] A. Smekal. Zur quantentheorie der dispersion. *Naturwissenschaften*, 11(43):873–875, 1923.

[174] D. Smith and P. Spanel. The challenge of breath analysis for clinical diagnosis and therapeutic monitoring. *Analyst*, 132(5):390–396, 2007.

[175] S. Smolka, M. Barth, and O. Benson. Highly efficient fluorescence sensing with hollow core photonic crystal fibers. *Opt. Express*, 15(20):12783–12791, 2007.

[176] O. Sode, M. Keceli, K. Yagi, and S. Hirata. Fermi resonance in solid co2 under pressure. *The Journal of Chemical Physics*, 138(7), 2013.

[177] S. Stewart, R. J. Priore, M. P. Nelson, and P. J. Treado. Raman imaging. *Annual Review of Analytical Chemistry*, 5:337–360, 2012.

[178] M. Sturm, M. Schlösser, R.J. Lewis, B. Bornschein, G. Drexlin, and H.H. Telle. Monitoring of all hydrogen isotopologues at tritium laboratory karlsruhe using raman spectroscopy. *Laser Physics*, 20(2):493–507, 2010.

[179] J. T. Sullivan. The estimation of starch. *Industrial & Engineering Chemistry Analytical Edition*, 7(5):311–314, 1935.

[180] L. Taiz and E. Zeiger. *Plant Physiology*. Sinauer Associates, 2010.

[181] K. J. R. Taylor and P. D. P. Rosman. Isotopic compositions of the elements 1997 (technical report). *Pure and Applied Chemistry*, 70(1), 1998.

[182] G. Tcherkez, S. Nogues, J. Bleton, G. Cornic, F. Badeck, and J. Ghashghaie. Metabolic origin of carbon isotope composition of leaf dark-respired co2 in french bean. *Plant Physiol.*, 131(1):237–244, 2003.

[183] R. Thapa, K. Knabe, K. L. Corwin, and B. R. Washburn. Arc fusion splicing of hollow-core photonic bandgap fibers for gas-filled fiber cells. *Opt. Express*, 14(21):9576–9583, 2006.

[184] A. Thöny and M. W. Sigrist. New developments in co2-laser photoacoustic monitoring of trace gases. *Infrared Physics & Technology*, 36(2):585–615, 1995.

[185] M. J. Thorpe, K. D. Moll, R. J. Jones, B. Safdi, and J. Ye. Broadband cavity ringdown spectroscopy for sensitive and rapid molecular detection. *Science*, 311(5767):1595–1599, 2006.

[186] P. J. Treado, C. W. Gardner, and M. P. Nelson. Method and apparatus for extended hyperspectral imaging, patent, us7420679 b2, 2008.

[187] P.J. Treado, A. Bangalore, M.P. Nelson, and C.T. Zugates. Simultaneous imaging and spectroscopy apparatus, patent, us6717668 b2, 2004.

[188] M. O. Trulson and R. A. Mathies. Excited-state structure and dynamics of isoprene from absolute resonance raman intensities. *The Journal of Physical Chemistry*, 94(15):5741–5747, 1990.

[189] S. Tummala, S. Sheth, J. Goldsmith, A. Goldar-Najafi, C. Murphy, M. Osburne, S. Mullin, D. Buxton, and D. Wagner. Quantifying gastric helicobacter pylori infection: A comparison of quantitative culture, urease breath testing, and histology. *Digestive Diseases and Sciences*, 52(2):396–401, 2007.

[190] K. Tveito, C. Brunborg, L. Sandvik, E. M. Loberg, and V. Skar. 13c-xylose and 14c-xylose breath tests for the diagnosis of coeliac disease. *Scand. J. Gastroenterol.*, 43(2):166–173, 2008.

[191] F. G. Vogt and M. Strohmeier. Confocal uv and resonance raman microscopic imaging of pharmaceutical products. *Molecular Pharmaceutics*, 10(11):4216–4228, 2013.

[192] W. H. Weber and R. Merlin. *Raman Scattering in Materials Science*. Springer, 2000.

[193] P. Werle, F. Slemr, K. Maurer, R. Kormann, R. Mücke, and B. Jänker. Near- and mid-infrared laser-optical sensors for gas analysis. *Optics and Lasers in Engineering*, 37(2-3):101–114, 2002.

[194] C. F. Windisch, V. Glezakou, P. F. Martin, B. P. McGrail, and H. T. Schaef. Raman spectrum of supercritical c18o2 and re-evaluation of the fermi resonance. *Phys. Chem. Chem. Phys.*, 14:2560–2566, 2012.

[195] E. Woolfenden. Monitoring vocs in air using sorbent tubes followed by thermal desorption-capillary gc analysis: Summary of data and practical guidelines. *Journal of the Air and Waste Management Association*, 47(1):20–36, 1997.

[196] K. Wörle, F. Seichter, A. Wilk, C. Armacost, T. Day, M. Godejohann, U. Wachter, J. Vogt, P. Radermacher, and B. Mizaikoff. Breath analysis with broadly tunable quantum cascade lasers. *Anal. Chem.*, 85(5):2697–2702, 2013.

[197] E. Yablonovitch. Inhibited spontaneous emission in solid-state physics and electronics. *Phys. Rev. Lett.*, 58:2059–2062, 1987.

[198] E. Yablonovitch, T. J. Gmitter, and K. M. Leung. Photonic band structure: The face-centered-cubic case employing nonspherical atoms. *Phys. Rev. Lett.*, 67:2295–2298, 1991.

[199] K. Yagi, S. Hirata, and K. Hirao. Vibrational quasi-degenerate perturbation theory: applications to fermi resonance in co2, h2co, and c6h6. *Phys. Chem.*, 10:1781–1788, 2008.

[200] D. Yakir and L. Sternberg. The use of stable isotopes to study ecosystem gas exchange. *Oecologia*, 123(3):297–311, 2000.

[201] D. Yu, F. Cheeseman, and S. Vanner. Combined oro-caecal scintigraphy and lactulose hydrogen breath testing demonstrate that breath testing detects oro-caecal transit, not small intestinal bacterial overgrowth in patients with ibs. *Gut*, 60(3):334–340, 2011.

[202] D. Zhang, J. D. Hanna, and D. Ben-Amotz. Single scan cosmic spike removal using the upper bound spectrum method. *Appl. Spectrosc.*, 57(10):1303–1305, 2003.

Acknowledgment

List of Publications

During this work several articles were published in scientific journals and results were presented in talks or poster presentations at different scientific conferences. A list of them is found below.

Patents

1. **S. Hanf**; T. Frosch; J. Popp, *Verfahren und Anordnung zur Wasserstoff-Sensorik*, September, 2014, DE10 2014 014 414.3

Peer-reviewed publications

1. R. Keiner; T. Frosch; **S. Hanf**; A. Rusznyak; D. M. Akob; K. Küsel; J. Popp, Raman Spectroscopy - An Innovative and Versatile Tool To Follow the Respirational Activity and Carbonate Biomineralization of Important Cave Bacteria, *Anal. Chem.*, 85(18):8708–8714, 2013.

2. **S. Hanf**; R. Keiner; D. Yan; J. Popp; T. Frosch, Fiber-enhanced Raman multi-gas spectroscopy – a versatile tool for environmental gas sensing and breath analysis, *Anal. Chem.*, 86(11):5278–5285, 2014.

3. **S. Hanf**; T. Bögözi; R. Keiner; T. Frosch; J. Popp, Fast and highly sensitive fiber enhanced Raman spectroscopic monitoring of molecular H_2 and CH_4 for point-of-care diagnosis of metabolic diseases in exhaled human breath , *Anal. Chem.*, 87(2):982–988, 2015.

4. **S. Hanf**; S. Fischer; H. Hartmann; R. Keiner; S. Trumbore; J. Popp; T. Frosch, Online investigation of respiratory quotients in Pinus sylvestris and Picea abies during drought and shading by means of cavity-enhanced Raman multi-gas spectrometry, *Analyst*, 140(13):4473-4481, 2015.

5. S. Fischer; **S. Hanf**; T. Frosch; G. Gleixner; J. Popp; S. Trumbore; H. Hartmann, Pinus sylvestris switches respiration substrates under shading but not during drought, *New Phyt.*, 207:542–550, 2015.

Conference contributions

1. **S. Hanf**; D. Yan; R. Keiner; J. Popp; T. Frosch, High sensitivity multitrace gas analysis by means of Raman spectrometry using a photonic bandgap fiber, *3rd International Congress on Biophotonics (ICOB)*, Jena, Germany, 19-21 June 2012 (poster).

2. T. Frosch ; Di Yan; **S. Hanf**; J. Popp, Fiber enhanced Raman spectroscopy, Proc. SPIE 9157, *23rd International Conference on Optical Fibre Sensors*, 915753, June 2, 2014 (talk).

3. **S. Hanf**; J. Popp; T. Frosch, Fiber-enhanced Raman multi-gas spectroscopy with hollow core photonic crystal fibers – A versatile tool for environmental gas sensing

and breath analysis, *24th International Congress on Raman Spectroscopy (ICORS)*, Jena, Germany, August 10-15, 2014 (poster).

4. T. Frosch; D. Yan; R. Keiner; **S. Hanf**; M. Brückner; T. Jochum; A. Bachmann; J. Popp, Enhanced Raman Spectroscopy, *International Congress on Raman Spectroscopy (ICORS)*, Jena, Germany, August 10-15, 2014 (talk).

5. **S. Hanf**; J. Popp; T. Frosch, Pushing the limit of sensitivity for Fiber-enhanced Raman multi-gas spectrometry – a versatile tool for clinical diagnostics by human breath analysis, *Int. Symposium on Photonics and Optoelectronics (SOPO) 2014*, Suzhou, China, August 22 – 24, 2014 (talk).

6. **S. Hanf**; S. Fischer; H. Hartmann; R. Keiner; S. Trumbore; J. Popp; T. Frosch, Raman spectroscopic online investigation of respiratory quotients in Pinus sylvestris and Picea abies during drought and shading, *American Geophysical Union (AGU) Fall Meeting*, 2014, San Francisco, USA, December 15-19, 2014 (poster).

7. H. Hartmann; S. Fischer; **S. Hanf**; T. Frosch; M. Reichelt; J. Popp; S. Trumbore, Pinus sylvestris switches respiration substrates under shading but not during drought, *European Geosciences Union (EGU) General Assembly 2015*, Vienna, Austria, April 12-17, 2015 (talk).

Selbständigkeitserklärung

Ich erkläre hiermit ehrenwörtlich, dass ich die vorliegende Arbeit selbständig, ohne unzulässige Hilfe Dritter und ohne Benutzung anderer als der angegebenen Hilfsmittel und Literatur angefertigt habe. Die aus anderen Arbeiten direkt oder indirekt übernommenen Daten und Konzepte sind unter Angabe der Quelle gekennzeichnet. Weitere Personen waren an der inhaltlich-materiellen Erstellung der vorliegenden Arbeit nicht beteiligt. Insbesondere habe ich hierfür nicht die entgeltliche Hilfe von Vermittlungsbzw. Beratungsdiensten (Promotionsberater oder andere Personen) in Anspruch genommen. Niemand hat von mir unmittelbar oder mittelbar geldwerte Leistungen für Arbeiten erhalten, die im Zusammenhang mit dem Inhalt der vorgelegten Dissertation stehen. Die Arbeit wurde bisher weder im In- noch im Ausland in gleicher oder ähnlicher Form einer anderen Prüfungsbehörde vorgelegt. Teile dieser Arbeit wurden aus Prioritätsgründen bereits veröffentlicht oder wurden zur Veröffentlichung eingereicht: [101, 82, 79, 80, 57]. Die geltende Promotionsordnung der Chemisch-Geowissenschaftlichen Fakultät ist mir bekannt. Ich versichere ehrenwörtlich, dass ich nach bestem Wissen die reine Wahrheit gesagt und nichts verschwiegen habe.

Ort, Datum: Jena, 06.05.2015

Unterschrift: